SAKARYA ÜNİVERSİTESİ
FEN BİLİMLERİ ENSTİTÜSÜ DERGİSİ

Sakarya University Journal of Science (SAUJS)

SAKARYA ÜNİVERSİTESİ

e-issn: 2147-835X

Volume: 29

Issue: 2

April 2025

VOLUME: 29 ISSUE: 2
E-ISSN 2147-835X

APRIL 2025
https://dergipark.org.tr/tr/pub/saufenbilder

SAKARYA UNIVERSITY JOURNAL OF SCIENCE

SAKARYA
ÜNİVERSİTESİ

Section Editor (Civil Engineering)

Section Editor (Chemistry)

Section Editor (Biology)

Section Editor (Mathematics)

Section Editor (Computer Science and Engineering)

Muhammed Maruf Öztürk
Computer Science and Engineering
Süleyman Demirel University
Isparta - Türkiye
muhammedozturk@sdu.edu.tr

Mustafa Akpinar
Computer Science and Engineering
High Tech Collages
United Arab Emirates
mustafakpinar@gmail.com

Section Editor (Physics)

Ceren Tayran
Department Physics
Gazi University
Ankara - Türkiye
c.tayran@gazi.edu.tr

Section Editor (Industrial Engineering)

Feyza Gürbüz
Department Industrial Engineering
Erciyes University
Kayseri - Türkiye
feyza@erciyes.edu.tr

Mehmet Emin Aydın
Department Industrial Engineering
University of The West of England Bristol
England
mehmet.aydin@uwe.ac.uk,

Barış Yüce
Department Industrial Engineering
University of Exeter
United Kingdom
b.yuce@exeter.ac.uk

Benjamin Durakovic
Department Industrial Engineering
International University of Sarajevo
Bosnia and Herzegovina
bdurakovic@ius.edu.ba

Section Editor (Mechanical Engineering)

Elif Eker Kahveci
Department of Mechanical Engineering
Sakarya University
Sakarya - Türkiye
eeker@sakarya.edu.tr

Erman Aslan
Department of Mechanical Engineering
Kocaeli University
Kocaeli - Türkiye
erman.aslan@kocaeli.edu.tr

Abderrahmane Benbrik
Department of Mechanical Engineering
M'hamed Bougara University
Egypt
abderrahmane.benbrik@univ-boumerdes.dz

Ali Cemal Benim
Department of Mechanical Engineering
Düsseldorf University of Applied Sciences
Germany
alicemal@prof-benim.com

Shi-Chune Yao
Department of Mechanical Engineering
Carnegie Mellon University
USA
sy0d@andrew.cmu.edu

Section Editor (Environmental Sciences and Engineering)

Senay Çetin Doğruparmak
Department of Environmental Engineering
Kocaeli University
Kocaeli - Türkiye
senayc@kocaeli.edu.tr

Section Editor (Food Science)

Aslı Uçar
Department of Food Sciences
Ankara University
Ankara - Türkiye
aucar@ankara.edu.tr

Section Editor (Electrical and Electronics Engineering)

Francesco De Paulis
Department of Electrical and Electronics Engineering
L'Aquila University
Italy
francesco.depaulis@univaq.it

Rıfkı Terzioğlu
Department of Electrical and Electronics Engineering
Bolu Abant Izzet Baysal University
Bolu - Türkiye
rifkiterzioğlu@ibu.edu.tr

Section Editor (Architecture)

Section Editor (Materials Science)

English Language Editor

Editorial Assistant

Statistical Editor

Indexing

Contents

Research Article

Sakarya Üniversitesi Fen Bilimleri Dergisi
Sakarya University Journal of Science

e-ISSN : 2147-835X
Publisher : Sakarya University

Vol. 29, No. 2, 140-150, 2025
DOI: https://doi.org/10.16984/saufenbilder.1582286

Research Article

Humidity Effect on Adsorption Kinetics of Aromatic and Chlorinated Hydrocarbon Vapors onto Fe_2O_3 Based Sensor

Nursel Can

Yildiz Technical University, Faculty of Arts and Science, Department of Physics, İstanbul, Türkiye, can@yildiz.edu.tr, ror.org/0547yzj13

ARTICLE INFO

Keywords:
Fe_2O_3
Adsorption kinetics
Aromatics
Chlorinated hydrocarbons
Sensor

Article History:
Received: 09.11.2024
Revised: 23.02.2025
Accepted: 25.02.2025
Online Available: 15.04.2025

ABSTRACT

In this study, the influence of relative humidity on amorphous Fe2O3 thin film' sensing properties towards aromatic and chlorinated hydrocarbon vapor and their adsorption kinetics were examined systematically. The sensing results showed that the relative humidity level has a significant effect not only on the aromatic and hydrocarbon sensing performance of Fe2O3 films but also on the baseline currents of the sensors. It was found that sensitivity increased approximately twofold when the relative humidity was raised from 20% to 40% in the presence of 14% toluene vapor. A comprehensive evaluation of the sensing performance indicated that the Fe2O3 film offers promising potential as a sensing element for the detection of toluene (C7H8) vapor, even at relatively high humidity levels at room temperature. The adsorption kinetics of toluene and carbon tetrachloride (CCl4) vapors on Fe2O3 were modeled using the Pseudo-first-order equation, as well as the Elovich and Ritchie models, and the key parameters of each model were determined and analyzed. Results from regression analysis indicated that the sensing performance and adsorption kinetics are dependent on the molecular structure of the analyte molecules. The Elovich model was found to be to describe the adsorption kinetics of the CCl4 on Fe2O3. On the other hand, first-order equation most accurately described the adsorption kinetics of C7H8 vapors on the Fe2O3 thin film, The Elovich and Ritchie's kinetics models were not satisfactory.

1. Introduction

Because of the increasing industrial activity, air quality pollution in the workplace and indoors caused by volatile organic vapors (VOCs) has become one of the most important threats to human health [1]. Studies show that VOC vapors have carcinogenic effects in both the short and long term and that there is even a direct relationship between VOC emissions and some types of cancer [2, 3]. Although VOC sensors are widely used in many different areas such as controlling and regulating industrial emissions [4] and monitoring indoor air quality [5], their use in the field of healthcare as biomarkers for early diagnosis and in food security are quite limited [6-8]. It is known that, the VOCs existing in the atmosphere, especially C_7H_8 and CCl_4, harm human health and also in terms of environmental pollution [9, 10].

As is known, C_7H_8 is an aromatic compound widely used in the furniture industry, paints, inks, and automobile fuels [11, 12]. It is also well known that long-term exposure to C_7H_8 vapor causes many diseases such as asthma and nasopharyngeal cancer due to its negative effects on the heart, kidneys, respiratory system, and nervous system, and it is listed as the third among cancer-causing VOCs by the World Health Organization [13, 14].
On the other hand, carbon tetrachloride is one of the chlorinated hydrocarbons found in the atmosphere as volatile organic vapor with a special odor and is used in many areas in the chemical industry such as organic solvents [15],

Cite as: N. Can (2025). Humidity Effect on Adsorption Kinetics of Aromatic and Chlorinated Hydrocarbon Vapors onto Fe2O3 Based Sensor, *Sakarya University Journal of Science*, 29(2), 140-150. https://doi.org/10.16984/saufenbilder.1582286

degreasing agent, cleanout and dry-clean reagent in the chemical industry. Research has shown that exposure to carbon tetrachloride, one of the primary toxic pollutants, has significant negative effects on the liver, kidney, and central nervous system even at low concentration levels. [10, 16].

Due to the increasing use of C_7H_8 and CCl_4 in industry and their negative effect on the human body, intensive work is being done on the development of sensors for detecting low concentrations of these toxic gases. For this purpose, in addition to analytical methods such as gas chromatography and mass spectrometry [17], sensors with very different operating principles such as electrochemical, photoionization, capacitive, and surface acoustic waves have been developed [18-20]. Despite numerous efforts to enhance the VOC vapor sensing performance of single semiconductors, their sensing capabilities remain constrained by several limitations, including high operating temperatures, low sensitivity, poor selectivity, and stability issues [21].

Recently, ferric oxide functional films have found applications in diverse areas such as semiconductor materials, magnetic materials, sensitive materials, and catalysts, among others [22]. Researchers have reported the electrical responses of α-Fe_2O_3 nanostructures to various oxidizing/reducing gases and humidity [23, 24]. It has been demonstrated that factors like grain size, porosity, and operating temperature play a significant role in influencing the sensitivity of α-Fe_2O_3 to different gases and humidity levels [25]. Theoretically, the gas sensing mechanism of this type of sensor is based on a conspicuous conductivity change of oxide semiconductor, deriving from the adsorption of oxygen and the chemical reaction between oxygen species and target gas molecules. Consequently, the composition and structure of sensitive materials play crucial roles in their sensing performances. [26-28]. Stable alpha-iron oxide (α-Fe_2O_3), an *n*-type semiconductor with good sensitivity, environmentally friendliness, high corrosion resistance, and easy fabrication properties, has been extensively applied in many fields including gas sensors [29, 30].

However, interference from other components in the sensing environment often poses challenges for chemical sensors. Additionally, relative humidity (RH) in the operating environment is commonly overlooked in the design of high-performance and reliable sensing devices. While studies have shown that sensor efficiency in selective VOC vapor detection is promising, understanding the mechanisms governing the interaction between the sensitive layer and VOC vapor molecules has become increasingly necessary. In this context, adsorption kinetics, a fundamental aspect for analyzing the adsorption process, serves as an essential indicator for evaluating adsorption efficiency.

Numerous kinetic models have been developed to explain the adsorption process on solid surfaces in solid-gas interactions. These models can describe adsorption kinetics with two, three, or even more parameters. In this study, the influence of relative humidity on the sensing properties of Fe_2O_3-based sensors for detecting C_7H_8 and CCl_4 vapors was investigated. The obtained adsorption data were analyzed and discussed using four different kinetic models: Elovich equation, Ritchie equation, first-order equation, and second-order equation.

2. Experimental

The sensing film of Fe_2O_3 was deposited on interdigitated microelectrode (IDE) arrays by the dip coating method. The starting solutions for the deposition of Fe_2O_3 thin films were prepared by dissolving 0.27 gr $FeCl_3{\cdot}6H_2O$ in 20 ml de-ionized water (pH =1.50) by magnetic string at room temperature to obtain a clear solution. In a separated wesel, an aqueous solution containing 0.04 gr NaOH with a pH value of 10.8 was prepared. Then, the cleaned IDE arrays were immersed successively in $FeCl_3{\cdot}6H_2O$ and NaOH solutions and DI-water for 20 s. The process was repeated 70 times with the same solutions.

Here, the cycle number refers to the immersion of the transducer surface in $FeCl_3{\cdot}6H_2O$ containing solution. The obtained films were annealed in atmospheric conditions at 300^o C for 2 hours to remove any hydroxide phase and post-

annealed at 500 ºC for 3 hours to get a pure phase of α-Fe_2O_3 [31].

In order to comparatively test the sensing performances of the amorphous phase of the Fe_2O_3 film for C_7H_8 and CCl_4 vapors; the concentration of C_7H_8 varied between 2% and 14% and the concentration of CCl_4 varied between 1% and 4% and the sensor currents were measured using Keithley model 617 electrometer. After the coating of Fe_2O_3 on the surface of the transducer, the sensors were placed in a homemade sensing cell and exposed to carrier gas (99.9 % pure N_2 was used as carrier gas) flow until a stable baseline current was reached.

Afterward, the Fe_2O_3-based sensor surface was exposed to seven well-defined different concentrations of C_7H_8 and CCl_4 vapors for 10 min and the variations in sensor current were recorded. In order to test whether the changes in the sensor current were reversible, the sensor surface was exposed to only the carrier gas at the same flow rate for another 10 min. The real-time sensing test cycle for C_7H_8 and CCl_4 involves exposing the sensor surface to a gas flow with seven distinct concentrations of target molecules, followed by purging with a carrier gas.

Details of the VOC vapor sensing experiment were provided by Gümrükçü et al. [32]. Desired concentrations of C_7H_8 and CCl_4 vapor was obtained by bubbling the carrier gas through liquid C_7H_8 and CCl_4. For relative humidity dependent investigations, the carrier gas was divided into two parts using computer driven mass flow controllers (Alicat Scientific, Inc.). One of them was passed through deionized water and the other one liquid phase of the target molecules. To examine the effect of relative humidity on sensing performance and adsorption kinetics, level of the relative humidity inside the test chamber was varied between 0% and 40% throughout the C_7H_8 and CCl_4 sensing experiments and controlled with a commercially available humidity meter.

3. Result and Discussion

3.1. Structural analysis

Structural analysis of the Fe_2O_3 films used as the sensing element in the sensors produced was carried out by using the X-ray diffraction (XRD) method and observed spectra for the films obtained after 30, 50, and 70 cycles are shown in Fig. 1. The fact that no dominant peak was observed in the XRD spectrum (Fig. 1) clearly shows that the produced Fe_2O_3 films have an amorphous nature.

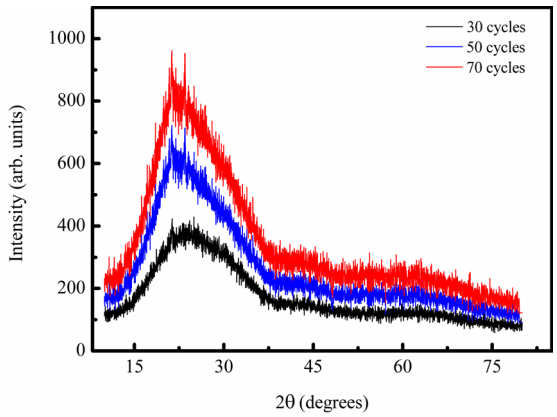

Figure 1. The effect of the number of the cycle on the XRD spectra of the Fe_2O_3 thin film

Additionally, as can be seen in Fig. 1, it was observed that by increasing the number of cycles from 30 to 70, the intensity of the broad peak in the XRD spectra increased. On the other hand, it was also observed that the width of the obtained XRD spectra decrease without any shift in its position. This behavior observed in the XRD spectra of the film was interpreted as an increase in the crystallization and grain sizes of the film with increasing cycle of numbers.

3.2. Sensing experiments

C_7H_8 and CCl_4 sensing performance of the Fe_2O_3 films were performed for seven different concentrations of target molecules at room temperature (297 K) and different relative humidity (RH) varying from 0% to 40%. These relative humidity values were obtained by passing the dry nitrogen gas used as a carrier through DI-water at different flow rates. The relative humidities produced in this way were measured and calibrated by using a hygrometer. In studies, to determine the effect of relative

humidity on the sensors' C_7H_8 and CCl_4 sensing properties and adsorption kinetics, relative humidity levels were kept low to avoid condensation. Fig. 2 shows the effect of relative humidity on the sensors' current for concentrations ranging from 2% to 14% of C_7H_8 and 1% to 4% of the CCl_4. The rationale behind choosing different C_7H_8 and CCl_4 concentrations is based on the results obtained from preliminary studies [32].

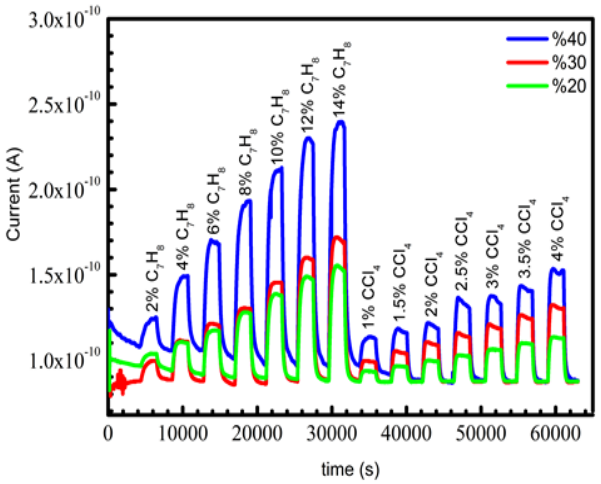

Figure 2. Relative humidity effect on C_7H_8 and CCl_4 response-recovery characteristics of the sensor

Fig. 2 clearly shows the effect of relative humidity level on both the baseline current of the sensors and the response-recovery characteristics towards C_7H_8 and CCl_4 vapors. It has been seen in Fig. 2 that the increase observed in the sensor baseline current with increasing relative humidity is compatible with similar studies in the literature. Studies on this subject showed that the resistance change in spinel-type metal oxides with RH level mainly is due to the adsorption of moisture molecules on the surface and capillary condensation [33]. Moisture adsorbed on the film surface used as the sensing unit may cause structural changes by forming hydrogen bonds with the sensing unit.

Additionally, it may cause swelling by diffusing within the sensing layer. The observed increase in baseline current with relative humidity can be attributed to the formation of a more ordered structure as a result of all these effects. A more ordered structure means higher charge mobility and higher electrical conductivity. The response-recovery characteristics presented in Fig. 2 show that when the sensor surface is exposed to different concentrations of C_7H_8 and CCl_4 vapors, it causes an initial rapid increase in the sensor current, and the rate of increase in sensor current slows down over time and tends to reach a steady state value.

As can be clearly seen from Fig. 2 when the sensor surface is exposed to the carrier gas, the sensor current starts to decrease again and reaches its initial value. This observation shows that the sensor response is reversible, thus the adsorption of the target molecules on the Fe_2O_3 film surface is physical adsorption. Although a satisfactory explanation of the interaction between metal-oxides and gas molecules has not been given so far, a reasonable explanation of the interaction between the Fe_2O_3 film surface and VOC vapor molecules, which causes an increase in the electrical conductivity of the films, can be given as follows.

Literature studies show that the electrical conductivity of metal-oxide thin films under atmospheric conditions is determined by reactions including charge exchange between oxygens in the atmosphere and the oxide [34]. Under atmospheric conditions, oxygen molecules in the environment are ionized as O^- or O_2^- by capturing the free electrons on the Fe_2O_3 film surface, and a depletion region is formed. This means that the charge carrier concentration and their mobility decrease, and as a result the sensor current also decreases. On the contrary, in the C_7H_8 and CCl_4 atmosphere, the reaction between C_7H_8 and CCl_4 molecules and oxygen species will release electrons. This process reduces the surface barrier and consequently, the electrical conductivity of the film increases.

The sensitivity, response, and recovery time of the gas sensor towards target odors are very important factors that relate directly to the rate of gas detection. The effect of the RH on the C_7H_8 and CCl_4 vapor sensing performance of the film of the Fe_2O_3 was compared in terms of sensitivity, response, and recovery time. Fig. 3 shows the variation of the C_7H_8 and CCl_4 sensitivity (S) of the sensor as a function of analytes (toluene and carbon tetrachloride) vapor concentrations for various humidity levels. It is

worth noting here that sensor sensitivity, as usual, is defined as;

$$S = \frac{\Delta I}{I_0} \quad (1)$$

In Equation (1), ΔI and I_0 show the changes in the sensor current when the sensor surface is exposed to analyte molecules and the baseline current, respectively. As can be seen in Fig. 3, a linear relationship was observed between both C_7H_8 and CCl_4 vapor concentrations and changes in the sensor current. Additionally, it is clearly seen that the sensor sensitivity increases as the RH level increases. For example, it has been observed that by increasing the relative humidity from 20% to 40%, the sensitivity of the sensor to C_7H_8 vapor at 14% concentration increases approximately two times.

A plausible explanation for the humidity dependence of the sensor sensitivity is as follows. Adsorbed water molecules on semiconductor oxides can alter the states and reactivity of adsorbed oxygen, which in turn affects the sensor's response to VOC vapor.

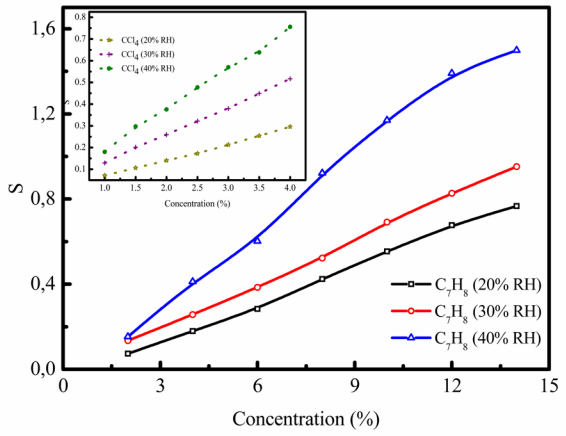

Figure 3. The variations of the sensor sensitivities as a function of target molecule concentrations

The response time is associated with the speed of change in the output on a stepwise change of the measurand. Fast response to a change of gas concentration is one of the key properties for assessing the suitability of sensors for VOC vapors safety. Response and recovery time are commonly used terms to define the speed of response of gas sensors. Response time is defined as the time it takes for the sensor to change its output signal from the initial state in the air to a certain percentage of the final value. The most common definition uses 90% of the final response.

Therefore, one of the most important parameters in gas sensors is the response time. In order to determine the influence of relative humidity on the response times of the sensors for C_7H_8 and CCl_4 vapors, a parameter denoted by τ_{90} has been defined. Here, as is customary in the literature, τ_{90} refers to the time required for the response (in our case sensor current) of the sensor to reach 90% of its maximum value when the sensor surface is exposed to the target molecules. Another important parameter for a gas sensor is the recovery time which is usually denoted as τ_{10}. The recovery time is defined as the time required for the sensor response to decrease to 10% of its initial value. Fig. 4 depicts the variations of the estimated response time for C_7H_8 and CCl_4.

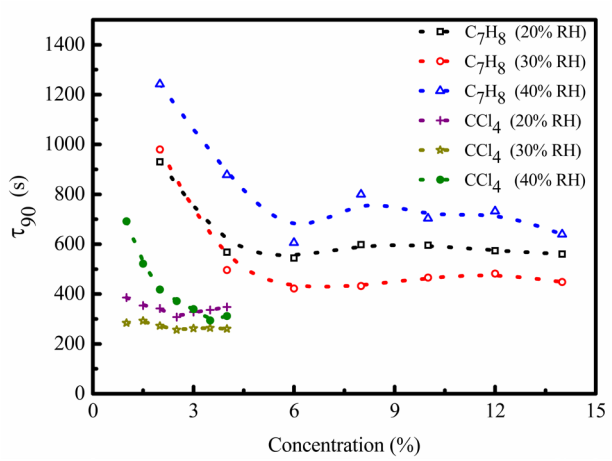

Figure 4. The variations of the estimated response time for C_7H_8 and CCl_4

On close analysis of response time plots Fig. 4 for these films, it becomes clear that the response time is decreasing function for low concentrations of C_7H_8 and CCl_4 vapors. This behaviour can be atributted to the ratio of the number of the gas molecules and the active adsorption sites. It is also clear from Fig. 4 that the response time of the sensor remains unchanged for higher concentrations of the analyte molecules.

In order to make clear the effect of the RH on the C_7H_8 and CCl_4 sensing performance of the Fe_2O_3 film, recovery times were also evaluated from the measured response and recovery characteristic of

the sensor. The recovery time (τ_{10}) is defined as the time require the sensor current return to 10% below its base line value after exposure carrier gas and its concentration dependence is shown in Fig. 5. As can be seen from the Fig. 5 that, in general, the recovery time is a decresing function of C_7H_8 and CCl_4 vapor concentrations. It should also be mentioned here that the recovery time is strongly dependent on the RH level. The lowest value of the recovery time was observed for 4% of the CCl_4 at 30% RH level. On the other hand, the sensor showed the quickest recovery for 14% ppm C_7H_8 at 20% RH. An overall evaluation of the response and recovery times, it was observed that these parameters are dependent on the RH level and the gas concentration.

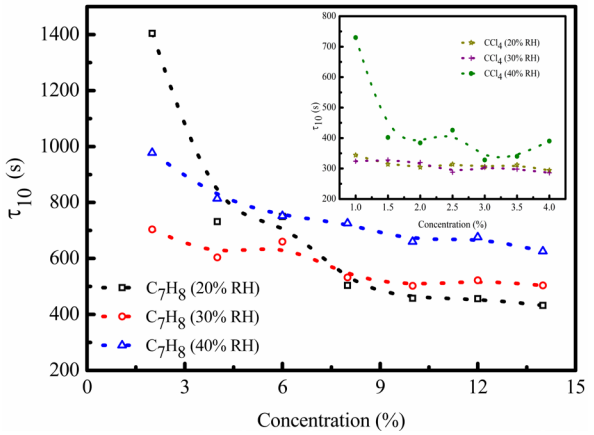

Figure 5. The effect of the relative humidity on the recovery times on Fe_2O_3-based sensors for C_7H_8 and CCl_4

4. Adsorption Kinetics

The best way to examine the interaction between adsorbent and adsorbate during the adsorption process is to examine adsorption kinetics. For this purpose, many models such as the first and second-order rate equation, Ritchie's and Elovich's equations have been developed to elucidate the gas adsorption mechanism on the solid surface. However, the number of studies in the literature comparatively examining the effect of relative humidity on C_7H_8 and CCl_4 adsorption kinetics onto the solid surface using these models is quite limited.

In this study, the adsorption data obtained during the interaction of amorphous Fe_2O_3 films with C_7H_8 and CCl_4 vapors at different relative humidity rates were analyzed using the Ritchie equation, Elovich model and pseudo-first-order equation, and the obtained results were discussed.

4.1. Ritchie equation

To explain the kinetics of solid-gas interactions, a model was developed by Ritchie in 1977 [35] based on the assumption that the adsorption rate at any time t depends solely on the fraction of unoccupied sites on the solid surface. Under these assumptions, the linear form of the Ritchie's equation can be expressed as,

$$\frac{1}{q_t} = \frac{1}{\alpha q_e t} + \frac{1}{q_e} \qquad (2)$$

where q_t and q_e are the amount of gas adsorbed at time t and after an infinite time, respectively. If the adsorption of C_7H_8 and CCl_4 on the Fe_2O_3 surface occurs by the Ritchie model, according to equation (2), the plots of $1/q_t$ versus $1/t$ should give a straight line. Fig. 6 shows $(1/q_t)$ vs.$1/t$ plot for various C_7H_8 vapors in 20% RH at room temperature. As can be seen from the Fig. 6, $(1/q_t)$ vs.$1/t$ plots for all concentrations of C_7H_8 exhibit a non-linear behaviour. The same type of behavior was observed for other RH levels investigated.

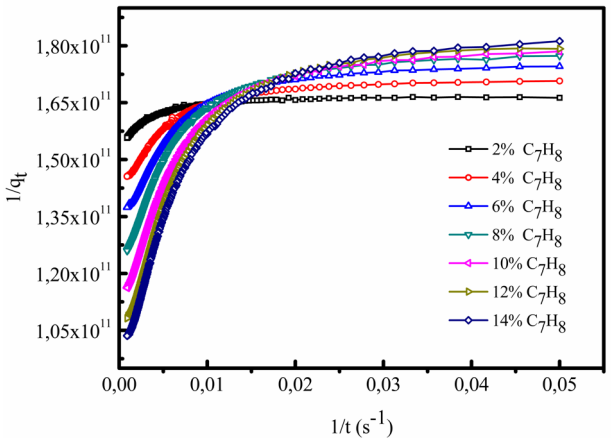

Figure 6. The plots of C_7H_8 adsorption kinetics for various C_7H_8 concentrations at 20% RH conditions

Whether the Ritchie equation was a suitable model to represent the adsorption kinetics of C_7H_8 vapor at different concentrations on the Fe_2O_3 surface, regression analysis was performed. The obtained regression analysis results showed that the correlation coefficient is in the range of 0.574 – 0.740. Additionally, the analysis of CCl_4 adsorption kinetics onto Fe_2O_3

surface according to the Ritchie's model, indicated that the correlation coefficient varies between 0.428 and 0.682 for all concentration and relative humidity examined. An overall evaluation of the regression analysis reveals that the Ritchie equation is not a suitable model to represent the adsorption kinetics of neither C_7H_8 nor CCl_4 vapor on the amorphous Fe_2O_3 surface.

4.2. Elovich model

Elovich's equation is another rate equation based on the adsorption capacity. Elovich equation was first developed to describe the kinetics of the chemisorption of gases on solids [36, 37]. According to the Elovich model, it is assumed that the rate of adsorption decreases with time because of the increase in surface coverage on the solid surface, and under this assumption, the integrated form of the Elovich equation is given by Eq. (3),

$$\theta = \left(\frac{1}{\beta}\right)\ln(\alpha\beta) + \left(\frac{1}{\beta}\right)\ln(t) \qquad (3)$$

In this equation, θ represents the adsorption capacity at any time t. On the other hand, since dθ/dt approaches α when θ approaches zero, the constant α in the Elovich equation is regarded as the initial adsorption rate. If it is assumed that the changes in the electrical conductivity of the sensing uni939t when the sensor surface is exposed to the target molecules are proportional to the surface coverage, according to Eq. (3) the plots of θ against ln (t) should be a straight line. A set of θ vs. ln (t) plots the adsorption of C_7H_8 and CCl_4 vapors on the Fe_2O_3 film surface are shown in Fig. 7 (a) and (b), respectively. The validity of the Elovich kinetic model is tested by the magnitude of the regression coefficient R^2.

As can be clearly seen from Fig. 7 (a), the plots of θ vs. ln (t) for C_7H_8 adsorption deviates greatly from linearity for all concentrations of C_7H_8 investigated. The results obtained suggest that this model is not a suitable model to represent C_7H_8 adsorption on the Fe_2O_3 surface. On the other hand, a comparison of the correlation coefficients R^2 (R^2 is in the range of 0.994–0.998 for the carbon tetrachloride adsorption) shows that the Elovich model fits better the experimental data for the adsorption of carbon tetrachloride vapors onto Fe_2O_3 thin film.

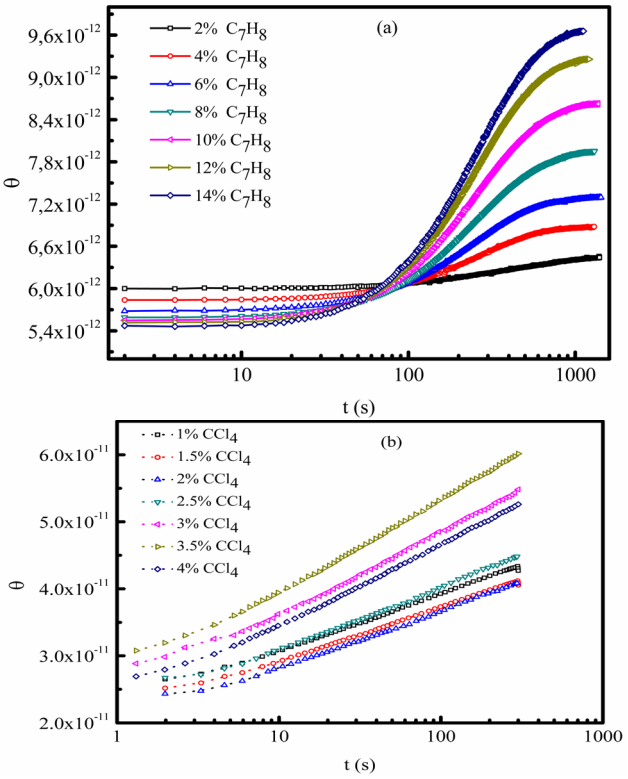

Figure 7. The plots of C_7H_8 (a) and CCl_4 (b) adsorption kinetics according to the Elovich model in a 20% RH environment

4.3. The Lagergren's first-order rate equation

The pseudo-first-order equation, also known as Lagergren's first-order rate equation, is one of the first models developed to understand the adsorption capacity of the adsorbent and the kinetics of the interaction between the adsorbent and adsorbate during the adsorption process. In this model, it is assumed that the adsorption rate on the sensor unit surface is directly proportional to the number of sites unoccupied by target molecules. It is expressed mathematically as follows [37].

$$\frac{dq_t}{dt} = k_{ads}(q_e - q_t) \qquad (4)$$

where q_t and q_e represent the adsorbed target molecules at any time during adsorption processes and at equilibrium, respectively. k_{ads} is the first-order adsorption rate constant. Under this assumption, the linearized form of the Eq. (4) can be expressed as,

$$\log(q_e - q_t) = \log q_e - \frac{k_{ads}}{2.303} t \quad (5)$$

If the plot of Log (q_e-q_t) versus t was found to be linear with a good correlation coefficient, indicating that Lagergren's equation is appropriate to VOC adsorption on Fe_2O_3 film. To quantify the applicability of the first-order model, the correlation coefficient was calculated from the response-recovery characteristics of the sensor. A set of Log (q_e-q_t)- t plots for room temperature adsorption of C_7H_8 and CCl_4 with various concentrations on Fe_2O_3 surface are shown in Figs. 8 and 9 for 20% RH, respectively.

Fig. 8 reveals that the plots of Log (q_e-q_t) versus t are linear for C_7H_8 adsorption, indicating that the interaction obeys the first order equation. However, for the adsorption of carbon tetrachloride vapor, the experimental data deviated considerably from the theoretical model (see Fig. 9). Therefore, the adsorption of C_7H_8 on Fe_2O_3 was more favorable by the pseudo-first-order kinetic model.

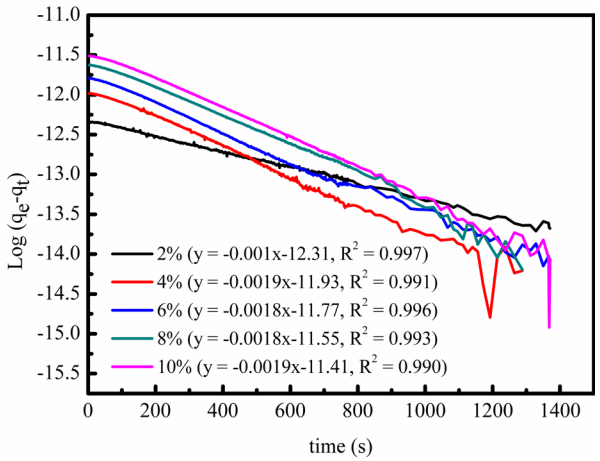

Figure 8. The dependency of the adsorption kinetics on the C_7H_8 concentration concerning Lagergren's first-order rate model at 20% RH

5. Conclusion

Fe_2O_3 films were grown on IDE structures by dip coating method. The sensing properties of these films for two different groups of volatile organic vapors, one aromatic (toluene) and the other chlorinated hydrocarbon (carbon tetrachloride) in different relative humidity environments were investigated as a function of relative humidity by measuring the changes in their electrical conductivity. The influence of relative humidity

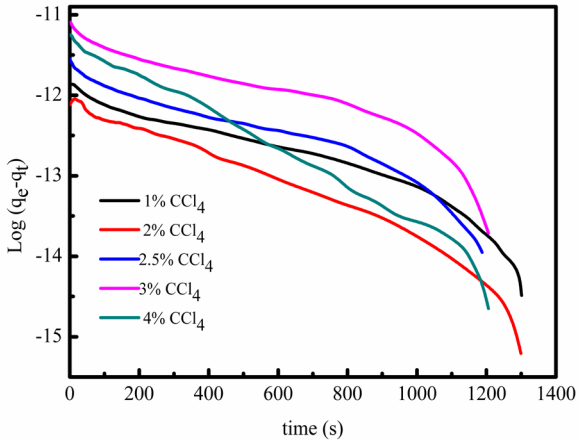

Figure 9. The dependency of the adsorption kinetics on the CCl_4 concentration with respect to Lagergren's first-order rate model at 20% RH

on the baseline conductivity and adsorption kinetics of C_7H_8 and CCl_4 vapor on Fe_2O_3 thin film has also been examined. Studies have shown that the gas sensing mechanism in Fe_2O_3 thin film is influenced by surface reactions, with humidity interference enhancing sensor sensitivity.

Observations confirmed that VOC vapor detection is feasible using the Fe_2O_3 film, even at room temperature. Experimental data were analyzed using the Pseudo-first-order, Ritchie's equation, and Elovich models. A comparison of regression coefficients (R^2) indicated that the Elovich model and first-order model best describe the adsorption of CCl_4 and C7H_8 vapor, respectively. With this strategy, we hope that Fe-based materials such as Fe_2O_3, the most abundant and cheapest material in the earth's crust, will become the key material for next-generation gas sensing technologies. It was found that the physical properties of the analyte molecules are important parameters in VOC adsorption kinetics onto Fe_2O_3. Overall findings indicate that ferric oxides a promising material for IDE based VOC sensor applications at room temperature.

Article Information Form

Acknowledgments
The author would like to thank Dr. Ahmet Altındal for his contributions.

Funding
The author has no received any financial support for the research, authorship or publication of this study.

The Declaration of Conflict of Interest/ Common Interest

No conflict of interest or common interest has been declared by the author.

The Declaration of Ethics Committee Approval

This study does not require permission from the ethics committee or any special permission.

The Declaration of Research and Publication Ethics

The author of the paper declares that they comply with the scientific, ethical, and quotation rules of SAUJS in all processes of the paper and that they do not make any falsification on the data collected. In addition, they declare that Sakarya University Journal of Science and its editorial board have no responsibility for any ethical violations that may be encountered and that this study has not been evaluated in any academic publication environment other than Sakarya University Journal of Science.

References

[1] S.-K. Song, Z.-H. Shon, Y.-H. Kang, K.-H. Kim, S.-B. Han, M. Kang, J.-H. Bang, I. Oh, "Source apportionment of VOCs and their impact on air quality and health in the megacity of Seoul," Environmental Pollution, Vol. 247, pp. 763-777, 2019.

[2] Z. F. Zhang, X. Zhang, X. Zhang, L.Y. Liu, Y. F. Li, W. Sun, "Indoor occurrence and health risk of formaldehyde, toluene, xylene and total volatile organic compounds derived from an extensive monitoring campaign in Harbin, a megacity of China," Chemosphere, vol. 250, 126324, 2020.

[3] M. L. Boeglin, D. Wessels, D. Henshel, "An investigation of the relationship between air emissions of volatile organic compounds and the incidence of cancer in Indiana counties," Environmental Research, vol. 100, no. 2, pp. 242-54, 2006.

[4] C. Xing, C. Liu, J. Lin, W. Tan, T. Liu, "VOCs hyperspectral imaging: A new insight into evaluate emissions and the corresponding health risk from industries," Journal of Hazardous Materials, vol. 461, 132573, 2024.

[5] J. P. Sá, M. C. M. Alvim-Ferraz, F. G. Martins, S. I. V. Sousa, "Application of the low-cost sensing technology for indoor air quality monitoring: A review," Environmental Technology & Innovation, vol. 28, 102551, 2022.

[6] M. Lueno, H. Dobrowolny, D. Gescher, L. Gbaoui, G. Meyer-Lotz, C. Hoeschen, T. Frodl, "Volatile Organic Compounds From Breath Differ Between Patients With Major Depression and Healthy Controls." Frontiers in Psychiatry, vol. 13, 819607, 2022.

[7] J. E. Belizário, J. Faintuch, M. G. Malpartida, "Breath Biopsy and Discovery of Exclusive Volatile Organic Compounds for Diagnosis of Infectious Diseases," Frontiers in Cellular and Infection Microbiology, vol. 10, 564194, 2021.

[8] E. Bonah, X. Huang, J. H. Aheto, R. Osae, "Application of electronic nose as a non-invasive technique for odor fingerprinting and detection of bacterial foodborne pathogens: a review," Journal of Food Science and Technology, vol. 57, no. 6, pp. 1977-1990, 2020.

[9] K. Karuppasamy, B. Sharma, D. Vikraman, E.-B. Jo, P. Sivakumar, H.-S. Kim, "Switchable p-n gas response for 3D-hierarchical NiFe2O4 porous microspheres for highly selective and sensitive toluene gas sensors," Journal of Alloys and Compounds, vol. 886, 161281, 2021.

[10] K. Zhan, Y. Xing, Y. Zhu, J. Yan, Y. Chen, "Carbon tetrachloride vapor sensing based on ZIF-8@ZnO/TiO2 one-dimensional top-defect photonic crystals," Sensors and Actuators, A: Physical, vol. 314, 112249, 2020.

[11] T. Wang, S. Liu, P. Sun, Y. Wang, K. Shimanoe, G. Lu, "Unexpected and enhanced electrostatic adsorption capacity of oxygen vacancy-rich cobalt-doped In2O3 for high-sensitive MEMS toluene sensor." Sensors and Actuators, B: Chemical, vol. 342, 129949, 2021.

[12] R. Zhang, S. Gao, T. Zhou, J. Tu, T. Zhang, "Facile preparation of hierarchical structure based on p-type Co3O4 as toluene detecting sensor," Applied Surface Science, vol. 503, 144167, 2020.

[13] Y. Sun, Z. Zhao, K. Suematsu, W. Zhang, S. Zhuiykov, K. Shimanoe, J. Hu, "MOF-derived Au-NiO/In2O3 for selective and fast detection of toluene at ppb-level in high humid environments." Sensors and Actuators, B: Chemical, vol. 360, 131631, 2022.

[14] T. Liu, Z. Yu, Y. Liu, J. Gao, X. Wang, H. Suo, X. Yang, C. Zhao, F. Liu, "Gas sensor based on Ni foam: SnO2-decorated NiO for Toluene detection," Sensors and Actuators, B: Chemical, vol. 318, 128167, 2020.

[15] J. H. Bulter, M. Battle, M. L. Bender, S. A. Montzka, A. D. Clarke, E. S. Saltzman, C. M. Sucher, J. P. Severinghaus, J. W. Elkins, "A Record of Atmospheric Halocarbons During The Twentieth Century From Polar Firn Air," Nature, vol. 399, pp. 749-755, 1999.

[16] J. Li, Y. L. Dong, J. Li, "Construction of a new ZnII coordination polymer for selective fluorescence sensing of CCl4," Australian Journal of Chemistry, vol. 69, no. 1, p. 56, 2016.

[17] C. Wei-Ni, Y. Zi-Cheng, C. Shen-Hui, Z. Ying-Tong, X. Guo-Bin, D. Dan-Dan, S. Xin, Z. Peng, W. Man-Man, H. Bin, Chinese Journal of Analytical Chemistry, vol. 50, p. 445, 2022.

[18] S. Acharyya, S. Nag, S. Kimbahune, A. Ghose, A. Pal, P. K. Guha, "Selective Discrimination of VOCs Applying Gas Sensing Kinetic Analysis over a Metal Oxide-Based Chemiresistive Gas Sensor," ACS Sensors vol. 6, no. 6, pp. 2218-2224, 2021.

[19] R. A. B. John, A. R. Kumar, "A review on resistive-based gas sensors for the detection of volatile organic compounds using metal-oxide nanostructures," Inorganic Chemistry Communications, vol. 133, 108893, 2021.

[20] G. C. Rezende, S. Le Calvé, J. J. Brandner, D. Newport, "Micro photoionization detectors," Sensors and Actuators, B: Chemical, vol. 287, pp. 86-94, 2019.

[21] H. Shan, C. Liu, L. Liu, J. Zhang, H. Li, Z. Liu, X. Zhang, X. Bo, X. Chi, "Excellent Toluene Sensing Properties of SnO2−Fe2O3 Interconnected Nanotubes," ACS Applied Materials & Interfaces, vol. 5, pp. 6376-6380, 2013.

[22] L. Huo, Q. Li, H. Zhao, L. Yu, S. Gao, J. Zhao, "Sol–gel route to pseudocubic shaped Fe_2O_3 alcohol sensor: preparation and characterization," Sensors and Actuators, B: vol. 107, pp. 915-920, 2005.

[23] W. Y. Chung, D. D. Lee, "Characteristics of α-Fe_2O_3 Thick Film Gas Sensors," Thin Solid Films, vol. 200, pp. 329-39, 1991.

[24] Y. Nakatani, M. Matsuoka, "Enhancement of Gas Sensitivity by Controlling Microstructure of a-Fe2O3 Ceramics," Japanese Journal of Applied Physics, vol. 22, pp. 912-6, 1983.

[25] P. V. Adhyapak, U. P. Mulik, D. P. Amalnerkar, I. S. Mulla, "Low Temperature Synthesis of Needle-like a-FeOOH and Their Conversion into α-Fe_2O_3 Nanorods for Humidity Sensing Application," Journal of the American Ceramic Society, vol. 96, p. 731-735, 2013.

[26] W. Geng, S. Ge, X. He, S. Zhang, J. Gu, X. Lai, H. Wang, Q. Zhang, "Volatile organic compound gas- sensing properties of bimodal porous α-Fe_2O_3 with ultrahigh sensitivity and fast response," ACS

Applied Materials & Interfaces, vol. 10, no. 16, pp. 13702-13711, 2018.

[27] M. Khan, M. Hussain, S. Crispi, S. Rafique R. Akram, G. Nerib, "Effects of Fe_2O_3 on the magnetic and gas sensing propertie sof Co_3O_4 nanoparticles," Next Materials, vol. 7, pages 100338, 2025.

[28] S. Lee, H. Won Jang, "α-Fe_2O_3 nanostructure-based gas sensors," Journal of Sensor Science and Technology, vol. 30, pp. 210-217, 2021.

[29] L. Liu, S. Fu, X. Lv, L. Yue, L. Fan, H. Yu, X. Gao, W. Zhu, W. Zhang, X. Li, W. Zhu, "A Gas Sensor With Fe2O3 Nanospheres Based on Trimethylamine Detection for the Rapid Assessment of Spoilage Degree in Fish," Frontiers in Bioengineering and Biotechnology, vol. 8, 2020.

[30] S. Vallejos, I. Gracia, Jaromır Hubalek, C. Cane, "VOC-sensitive structures with nanoscale heterojunctions based on WO_3-x nanoneedles and Fe_2O_3 nanoparticles," Monatshefte für Chemie-Chemical, vol.148, pp. 1921-1927, 2017.

[31] R. Belkhedkar, A. U. Ubale, "Preparation and Characterization of Nanocrystalline α-Fe2O3 Thin Films Grown by Successive Ionic Layer Adsorption and Reaction Method," International Journal of Materials and Chemistry, vol. 4, no.5, pp. 109-116, 2014.

[32] S. Gümrükçü, Y. Urfa, A. Altındal, M. İ. Katı, S. Akyürekli, A. Gül, Y. Şahin, İ. Özçeşmeci, "The effect of metal type and gamma irradiation doses on the VOC detection performance of new 1,3- bis(2-pyridylamino) isoindoline complexes", Journal of Molecular Structure, vol. 1318, 139235, 2024.

[33] G. Neri, A. Bonavita, S. Galvagno, N. Donato, A. Caddemi, "Electrical characterization of Fe2O3 humidity sensors doped with Li+, Zn2+ and Au3+ ions," Sensors and Actuators, B: Chemical, 111-112 (SUPPL.), pp. 71-77, 2005.

[34] N. Barsan, U. Weimar, "Conduction model of metal oxide gas sensors," Journal of Electroceramics, vol. 7, pp. 143–167, 2001.

[35] A. G. Ritchie, "Alternative to the Elovich equation for the kinetics of adsorption of gases on solids," Journal of the Chemical Society, Faraday Transactions 1: Physical, vol. 73, pp. 1650-1653, 1977.

[36] M. J. D. Low, "Kinetics of chemisorption of gases on solids," Chemical Reviews, 60, pp. 267-307, 1960.

[37] S. H. Chien, W. R. Clayton, "Application of Elovich Equation to the Kinetics of Phosphate Release and Sorption in Soils." Soil Science Society of America Journal, vol. 44, pp. 265-268, 1980.

Sakarya Üniversitesi Fen Bilimleri Dergisi
Sakarya University Journal of Science

e-ISSN : 2147-835X
Publisher : Sakarya University

Vol. 29, No. 2, 151-159, 2025
DOI: https://doi.org/10.16984/saufenbilder.1615457

Research Article

Lattice Boltzmann Modelling of Natural Convection Problems in a Cavity with a Different Wall Temperature

Erman Aslan[1*], Ozlem Yalcin[2]

[1] Kocaeli University, Faculty of Engineering, Department of Mechanical Engineering, Kocaeli, Türkiye, erman.aslan@kocaeli.edu.tr, ror.org/0411seq30
[2] Istanbul Gelişim University, Faculty of Engineering and Arhitecture, Department of Aeronautical, İstanbul, Türkiye, oyalcin@gelisim.edu.tr, ror.org/0188hvh39
*Corresponding Author

ARTICLE INFO

Keywords:
Lattice Boltzmann Method
Natural convection
Computational fluid dynamics
Laminar flow
Nusselt number

Article History:
Received: 07.01.2025
Revised: 03.03.2025
Accepted: 05.03.2025
Online Available: 15.04.2025

ABSTRACT

In this study, the cyclic natural convection problem in a square enclosure is modeled using the Lattice Boltzmann Method (LBM) under laminar flow conditions. Four different combinations of boundary conditions are employed to create cases. These cases are denoted as HHHC (Horizontal Hot Horizontal Cold), HHVC (Horizontal Hot Vertical Cold), VHHC (Vertical Hot Horizontal Cold), and VHVC (Vertical Hot Vertical Cold). Four Rayleigh numbers have been utilized to represent laminar flow conditions, namely Ra=10^4, 10^5, 10^6, and 10^7. For validation purposes, the well-validated finite volume method-based commercial code Ansys-Fluent is employed. In the VHVC model and at the highest Rayleigh number, the results obtained with LBM were compared to and validated against the results obtained with the finite volume method. Nusselt numbers are compared for the four cases based on Rayleigh numbers, and the case with highest heat transfer identified. Cases of HHHC and VHVC have produced the lowest and highest Nusselt number, respectively.

1. Introduction

Numerical modeling of natural convection heat transfer for an enclosure has garnered significant attention. This modeling finds applications in various engineering fields such as building insulation, fire prevention systems, solar collectors, food preservation systems, compact heat exchangers, and cooling systems employed in electricity or nuclear power generation plants, among others [1, 2]. Our problem consists of three main subjects. Firstly, natural convection in a square enclosure; secondly, the Lattice Boltzmann Method; and finally, natural convection in a square enclosure with Lattice Boltzmann modeling; therefore, the literature review is divided into three parts.

Lage and Bejan [3] explored the numerical and theoretical aspects of natural convection resonance within an enclosure subjected to periodic heating from the side. One side was cold (constant temperature), the other side was heated with pulsating heat flux in a two-dimensional square enclosure. In the numerical computations, Prandtl number varied between 0.01 and 0.7, the heat flux Rayleigh number range was 10^3-10^9, and nondimensional frequency range of 0-0.3 was applied. Theoretical considerations revealed that the numerically determined critical frequencies could be predicted by aligning the period of the pulsating heat input with the rotation period of the enclosed fluid. Mahdavi et al. conducted both experimental and numerical studies to investigate the thermal and hydrodynamic characteristics of laminar natural convective flow within a rectangular cavity filled with water and air [4].

The enclosure has a unique aspect ratio. Two vertical walls were applied to constant temperature boundary conditions with one wall

Cite as: E. Aslan, O. Yalcin (2025). Lattice Boltzmann Modelling of Natural Convection Problems in a Cavity with a Different Wall Temperature, *Sakarya University Journal of Science*, 29(2), 151-159. https://doi.org/10.16984/saufenbilder.1615457

being hot, the other cold. All other walls were properly insulated. The finite volume-based commercial code Ansys-Fluent was used for numerical investigations. The numerical results were in good agreement with measured data. The distortion of air is much higher than water. Ugurbilek et al. conducted a numerical investigation of three-dimensional natural convection in an air-filled cubical enclosure with gradually changing partitions [5]. The steady-state governing equations were resolved using the Boussinesq approximation and the finite volume method. Two scenarios were examined: one with partitions positioned perpendicularly (Case-1) and another with partitions positioned parallel (Case-2).

The opposing lateral walls of the enclosure were subjected to heating and cooling, while the remaining walls were considered adiabatic. Case-2 played major roles for convective heat transfer. Pesso and Piva investigated steady free convection at low Prandtl numbers numerically, which was caused by large density differences in a square cavity [6]. The Nusselt number was derived at Rayleigh numbers ranges of 10 and 10^8, Prandtl number ranges of 0.0071 and 7.1, and Gay-Lussac number ranges of 0 and 2. Consequently, a Nusselt number correlation was proposed based on physical arguments. Numerical analysis of the natural convection phenomenon resulting from nonuniform wall heating in a square cavity was investigated at laminar Rayleigh numbers by Turkyilmazoglu [7]. A finite element technique was employed for the numerical simulation of thermally driven flow.

The best heat transfer rate was acquired as the heating took place near the top wall of the heated boundary. Turkyilmazoglu investigated a different type of lid-driven cavity flow in which the single lid is separated into two joint active/passive walls representing potential stirrers during a chemical mixing process [8]. The right portion of the wall is allowed to move freely to the right at a uniform velocity, while the left portion, attached to the adjacent wall at a point of dislocation, is regarded as stationary or able to move freely at a constant speed. A finite element approach was used to solve numerically.

The Lattice Boltzmann Method (LBM) offers an innovative numerical strategy for modeling viscous, incompressible flows within the subsonic range [9-14]. Instead of directly addressing the traditional continuum hydrodynamic equations, LBM aims to replicate fluid flow by monitoring the evolution of distribution functions of microscopic fluid particles. This kinetic characteristic of LBM introduces unique attributes that distinguish it from other numerical methods, including simplified modeling of fluid interactions and complete parallelism. In the last twenty years, LBM has garnered significant attention and interest, witnessed rapid progress in developing novel models and applications across diverse fields [9-11]. Although LBM has proven successful in simulating isothermal flow problems, its application in heat transfer systems has encountered challenges, primarily due to severe numerical instability in thermal models.

Karki et al. studied natural convection cavity numerically with different aspect ratios and using the lattice Boltzmann method [15]. The right side and left side walls were hot and cold, respectively, the other sides were adiabatic. Prandtl number kept constant at 0.71 and Rayleigh numbers varied between 10^3 and 10^6. The Nusselt number, streamlines and isotherms were observed to understand the physics of the problem. It was found that Nusselt number increases with Rayleigh number, and high aspect ratios have a negative effect on Nusselt number. Feng et al. introduced a novel thermal lattice Boltzmann (LB) model designed for numerically simulating natural convection under conditions characterized by significant temperature disparities and elevated Rayleigh numbers [16].

A regularization method was devised for the lattice Boltzmann equation, incorporating a third-order expansion of equilibrium distribution functions and introducing a temperature term to restore the equation of state for an ideal gas. Wei et al. developed a novel two-dimensional coupled lattice Boltzmann model via modified thermal equilibrium function for thermal incompressible fluid flows [17].
This novel numerical model gave more stability than standard lattice Boltzmann method. Present model was successfully assessed in free

convection cavity problem at laminar flow. Lattice Boltzmann analysis on natural convection heat transfer and fluid flow in a two-dimensional square enclosure with sinusoidal wave and different convection mechanism was investigated by Pichandi and Anbalagan [18].

In LBM analysis, single relaxation time (SRT) and D2Q9 lattice links was used. The working fluid was air (Pr=0.71). Nusselt number, isotherms and streamlines were observed to comprehend the physics of the problem. In recent years, the use of machine learning in natural convection problems within enclosed domain using LBM has been present [19]. Additionally, GPU parallel computing approaches [20] have also been employed for such problems

This study employs the Lattice Boltzmann Method (LBM) to model the cyclic natural convection problem within a square enclosure under laminar flow conditions. Four distinct combinations of boundary conditions, which are Horizontal Hot Horizontal Cold (HHHC), Horizontal Hot Vertical Cold (HHVC), Vertical Hot Horizontal Cold (VHHC) and Vertical Hot Vertical Cold (VHVC), are utilized to establish different cases. These cases are assessed with four Rayleigh numbers (Ra=10^4, 10^5, 10^6, and 10^7) representing laminar flow conditions. Investigating natural convection heat transfer with four different Rayleigh numbers in laminar flow under four different boundary condition combinations and writing an in-house LBM code constitutes the originality of this study.

In order to validate our code and results, the well-validated finite volume method-based commercial code, Ansys-Fluent, is employed [21]. In the VHVC model, particularly, at the highest Rayleigh number, LBM results are compared and validated against those obtained using the finite volume method. Nusselt numbers are then compared across the four cases based on their respective Rayleigh numbers, enabling the identification of cases exhibiting the highest heat transfer.

1.1. Problem definition

Figure 1 shows the physical model of the present study. A two-dimensional natural convection within a square enclosure filled with air (Pr=0.71). Length and width of the domain are same. Four different Rayleigh numbers which includes laminar flow conditions have been considered, and these values are Ra=10^4, 10^5, 10^6 and 10^7. Rayleigh number is based on length of domain. Gravitational acceleration (g) is imposed in negative y direction.

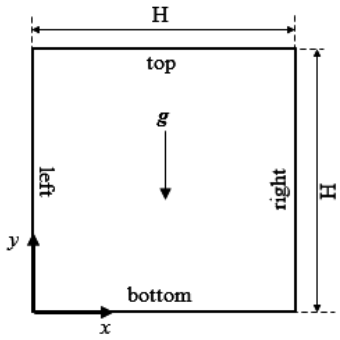

Figure 1. Physical model

In Table 1, four different cases with thermal boundary conditions are represented. The nondimensional temperature θ can range between zero and one, where θ equals 0 representing cold, and θ equals 1 representing hot. The first case is named HHHC, where the top wall and bottom wall are cold and hot, respectively, and the other walls are adiabatic ($q^{"} = 0$). The second case, HHVC, features a hot bottom wall and a cold left wall, with the other walls being adiabatic. In the third case, VHHC, the top wall and left walls are cold and hot, respectively, while the other walls remain adiabatic. Finally, the last case is VHVC, where the left wall is cold, the right wall is hot, and the other walls are adiabatic. All walls are stationary, and no-slip boundary conditions are applied for the momentum equation.

Table 1. Thermal boundary conditions

Model	top	bottom	left	right
HHHC	$\theta = 0$	$\theta = 1$	$q^{"} = 0$	$q^{"} = 0$
HHVC	$q^{"} = 0$	$\theta = 1$	$\theta = 0$	$q^{"} = 0$
VHHC	$\theta = 0$	$q^{"} = 0$	$\theta = 1$	$q^{"} = 0$
VHVC	$q^{"} = 0$	$q^{"} = 0$	$\theta = 0$	$\theta = 1$

1.2. LBM formulation

The LBM formulations most commonly utilizes rely on the single relaxation time approximation by Bhatnagar-Groos-Krook (BGK) [22]. In the

present work, incompressible LBM formulation is adopted [23]. The two-dimensional and nine-velocity lattice model (D2Q9) shown in Figure 2 is used.

Based on current modeling, two distinct distribution functions are employed—one for density (momentum) and another for temperature

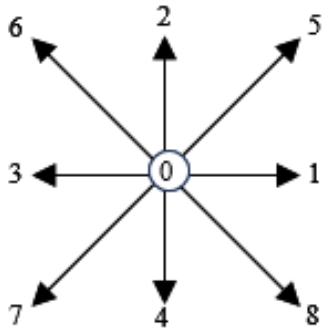

Figure 2. D2Q9 lattice model

(energy). The lattice Boltzmann evaluation equations for momentum and energy transport, discretized on a lattice, are typically addressed in two sequential steps: first, the "collision" step, followed by the subsequent "streaming" step.

- Collision

$$\tilde{f}_k(\vec{x}, t+\delta t) = f_k(\vec{x}, t) - \omega\left[f_k(\vec{x}, t) - f_k^{eq}(\vec{x}, t)\right] + F\delta t \quad (1a)$$

$$\tilde{g}_k(\vec{x}, t+\delta t) = g_k(\vec{x}, t) - \omega_T\left[g_k(\vec{x}, t) - g_k^{eq}(\vec{x}, t)\right] \quad (1b)$$

- Streaming

$$f_k(\vec{x} + \vec{c}_k\delta t, t+\delta t) = \tilde{f}_k(\vec{x}, t+\delta t) \quad (2a)$$

$$g_k(\vec{x} + \vec{c}_k\delta t, t+\delta t) = \tilde{g}_k(\vec{x}, t+\delta t) \quad (2b)$$

For natural convetion, external force (F) is defined via Boussinesq approximation. It is only applied in negative y direction due to gravitional accelaration.

$$F = \rho g \beta [T - T_{mean}] \quad (3)$$

where ρ and β are density and thermal expansion cofficient, respectively. T represents the local air temperature at square domain, while T_{mean} indicates the mean temperature of air. The collision frequencies are defined for momentum and energy equations as follows;

$$\omega = 1/\left(\left(\frac{\nu}{c_s^2}\delta t\right) + 0.5\right) \quad (4a)$$

$$\omega_T = 1/\left(\left(\frac{\alpha}{c_s^2}\delta t\right) + 0.5\right) \quad (4b)$$

Here, ν and α represents the kinematic viscosity and thermal diffusivity. And the lattice sound of speed c_s and lattice speed c are defined as:

$$c_s = c/\sqrt{3} \quad (5)$$

$$c = \delta/\delta t \quad (6)$$

The nine discrete velocities based on D2Q9 lattice model are:

$$\vec{c}_k = c\begin{bmatrix} 0 & 1 & 0 & -1 & 0 & 1 & -1 & -1 & 1 \\ 0 & 0 & 1 & 0 & -1 & 1 & 1 & -1 & -1 \end{bmatrix} \quad (17)$$

The equilibrium distribution functions are for momentum and energy equations:

$$f_k^{eq} = w_k\rho\left[1 + \frac{3}{c^2}\vec{c}_k\vec{u} + \frac{9}{2c^4}(\vec{c}_k\vec{u})^2 - \frac{3}{2c^2}\vec{u}\vec{u}\right] \quad (8a)$$

$$g_k^{eq} = w_k T\left[1 + \frac{3}{c^2}\vec{c}_k\vec{u}\right] \quad (8b)$$

with weighting foctors of D2Q9 lattice.

$$w_k = \left[\frac{4}{9} \quad \frac{1}{9} \quad \frac{1}{9} \quad \frac{1}{9} \quad \frac{1}{9} \quad \frac{1}{36} \quad \frac{1}{36} \quad \frac{1}{36} \quad \frac{1}{36}\right] \quad (9)$$

The macroscopic (density, pressure, velocity and temperature) fields are obtained from:

$$\rho = \sum_{k=0}^{8} f_k = \sum_{k=0}^{8} f_k^{eq} \quad (10a)$$

$$p = \rho c_s^2 \quad (10b)$$

$$\vec{u} = \frac{1}{\rho}\sum_{k=0}^{8} c_k f_k = \frac{1}{\rho}\sum_{k=0}^{8} c_k f_k^{eq} \quad (10c)$$

$$T = \sum_{k=0}^{8} g_k = \sum_{k=0}^{8} g_k^{eq} \quad (10d)$$

The time step size (δt) is same with lattice length (δ), therefore, lattice speed (Eq. 6) is taken as an unity. Lattice sound speed (Eq. 5) is $1/\sqrt{3}$

Detailed presentation of boundary condition implementations is omitted here for conciseness; however, it is available in A.A. Mohammad's work [21]. In LBM, boundary conditions can be implemented via distribution functions for the momentum and the energy equations. Owing to the streaming step of the LBM, there are unknown and known distribution functions, and unknown distribution functions are established using known distribution functions to apply all boundary conditions. In the momentum equations, no-slip boundary conditions are enforced at walls using the bounce-back rule, with the physical boundaries of the solution domain aligned with lattice grid lines. For the energy equation, constant temperature and zero heat flux boundary conditions are applied according to the determined four cases (Table 1). The LBM formulations described above are implemented in-house LBM code via FORTRAN programming.

1.3. Validation

To validate our LBM code, we extensively employ the validated finite-volume-based commercial CFD code Ansys-Fluent [19]. The Boussinesq approximation is utilized in the reference calculation, similar to LBM. The QUICK scheme is employed to discretize all convective terms. For pressure-velocity coupling, the SIMPLEC algorithm is utilized. The default under-relaxation parameters are set at 1.0 for pressure, 0.7 for momentum, and 1.0 for energy, respectively. Convergence criteria include a threshold of 10^{-6} for continuity, x-velocity, and y-velocity. In the case of the energy equation, a residual value of 10^{-8} is employed.

Validation is employed for the case of VHVC at the highest Rayleigh number (Ra=10^7). The same mesh numbers (200 lattices/finite volumes in the x-direction and 200 lattices/finite volumes in the y-direction) are used; therefore, a total of 40000 lattices/finite volumes are used for validation. These mesh numbers support the stability of LBM. Since the used lattice numbers are suitable for LBM stability, a grid independence study is not conducted. The dimensionless temperature gradient distribution, Nusselt number, along the hot and cold walls is calculated using the numerical grid adjacent to the wall for LBM and FVM. Then, the Nusselt number for each wall is determined by integrating the Nusselt numbers over the wall and dividing by the wall length. Table 2 represents the Nusselt number comparison for the case of VHVC at Ra=10^7. The Nusselt number is computed for both the cold and hot walls. The differences between LBM and FVM are 0.64% and 0.72% for the cold wall and hot wall, respectively. These difference values are acceptable; therefore, we validate our LBM code.

Table 2. Nusselt number comparison for VHVC at Ra=10^7

Nu	LBM	FVM	Difference (%)
Cold wall	17.8587	17.7434	0.64
Hot wall	18.0579	17.7345	2.40

2. Conclusions and Discussion

Figure 3 shows the nondimensional streamlines at the highest Rayleigh number (Ra=10^7). A total

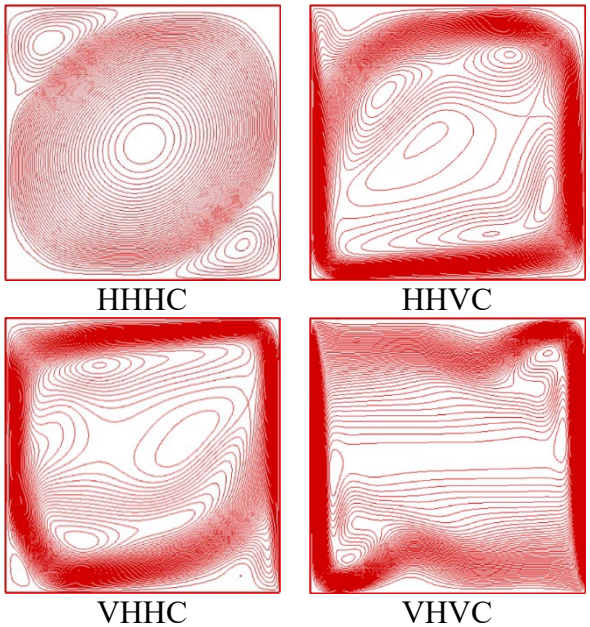

Figure 3. Nondimensional streamlines for four cases at Ra=10^7

of 51 streamlines are used in the all cases for better comparison, therefore step size between streamlines is 0.01960. In the symmetric cases, such as HHHC and VHVC, the streamlines exhibit greater symmetry. At lower Rayleigh number, which are not shown here, the degree of symmetry becomes even more evident. In

HHHC, the streamlines are less dense near the wall, whereas in the other cases, the streamlines near the wall are denser. Streamlines on heated and cooled surfaces exhibit higher density compared to adiabatic surfaces.

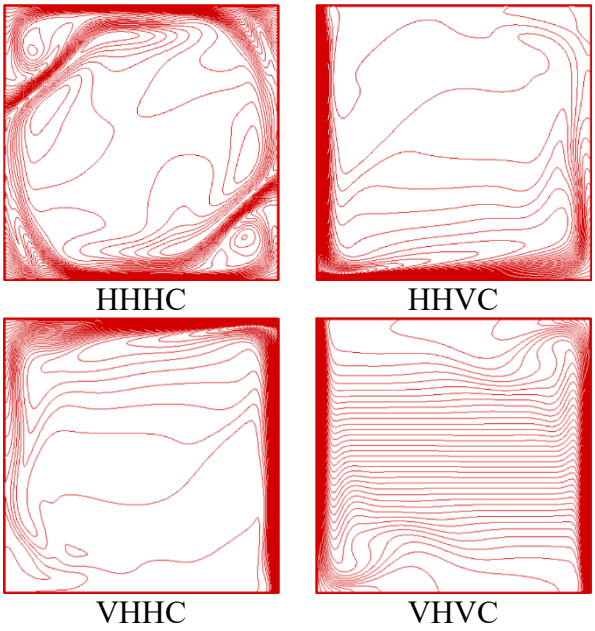

Figure 4. Isotherm for four cases at Ra=10^7

Isotherms are represented at the highest Rayleigh number (Ra=10^7) in Figure 4. Here, again a total 51 isotherms are used in the all cases for better comparison. The step size between isotherms is 0.01960. Streamlines characteristics effect the isotherms, therefore the same comments can be done for isotherms. In the symmetry cases, like HHHC and VHVC, the isotherms display greater symmetry. As we move to lower Rayleigh numbers, although not depicted here, the level of symmetry becomes even more pronounced. In the case of HHHC, the streamlines are less concentrated near the walls, whereas in other cases, the isotherms near the wall become denser. Isotherms on heated and cooled surfaces demonstrate a higher concentration when compared to adiabatic surfaces. Cases characterized by dense isothermals at the walls produce higher Nusselt numbers. Consequently, at Ra=10^7, VHVC yields the highest Nusselt number. Subsequently, cases of VHVC and HHHC produces equivalet Nusselt numbers. On the other hand, HHHC produces lowest Nusselt number.

Figure 5 exhibits the Nusselt number variation with Rayleigh numbers for (a) cold wall and (b) hot wall. The Rayleigh number is presented in Figure 5 on a logarithmic scale. Nusselt number increases with Rayleigh numbers as expected. At Ra=10^7, the Nusselt number interpretations based on isotherms contours align with Figure 5. In most cases, both cold and hot wall generally produced nearly equal Nusselt numbers, with exception occurring in nonsymmetric cases (HHVC and VHHC) for Rayleigh numbers of 10^4, 10^5 and 10^6. At lowest Rayleigh number, HHHC and VHVC yields lowest Nusselt number. At the VHVC case, the Nusselt number increases rapidly with Rayleigh numbers, reaching its peak at the highest Rayleigh number.

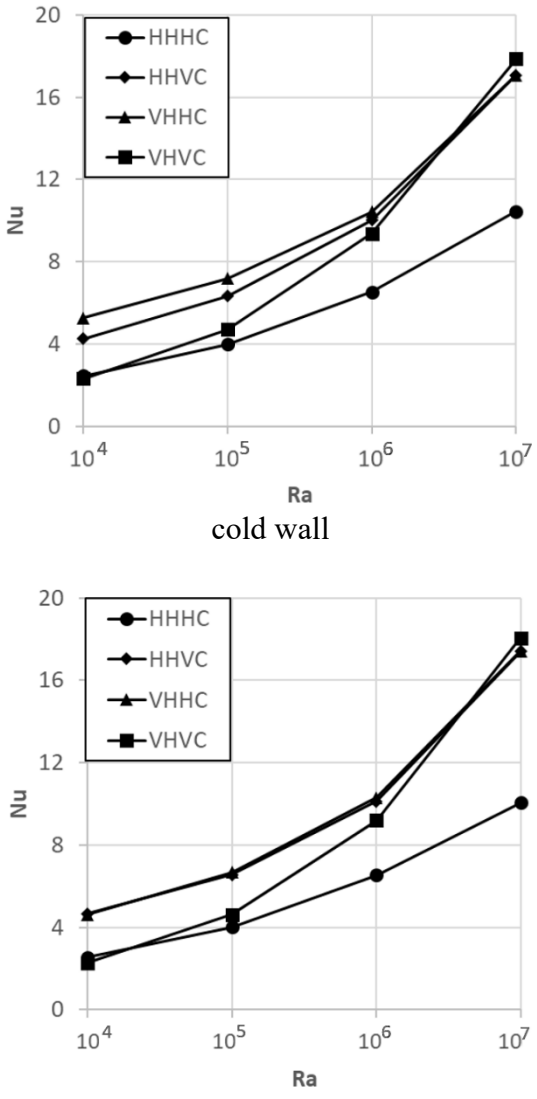

Figure 5. Nusselt number variation with Rayleigh numbers for (a) cold wall and (b) hot wall

Flow and heat characteristics are examined under four different cases and in laminar natural convection. The LBM requires more lattices due

to stability issues at higher Rayleigh or Reynolds number. This is a limitation of the LBM. This study will involve turbulent flows, meaning it will work at higher Rayleigh numbers. For this purpose, turbulence model will be added or implemented to our in-house code.

3. Conclusion

In this paper, the lattice Boltzmann method (LBM) is utilized to model the cyclic natural convection phenomenon inside a square enclosure under laminar flow conditions. Various combinations of boundary conditions are applied to create different cases which are HHHC, HHVC, VHHC and VHVC. These cases are evaluated using four Rayleigh numbers (Ra=10^4, 10^5, 10^6, and 10^7) to represent laminar flow conditions. In order to validate the results, the well-validated finite volume method-based commercial code, Ansys-Fluent, is employed [19]. Streamlines, isotherms and variation of Nusselt number with Rayleigh numbers are examined. The following conclusions can be obtained as below:

- Nusselt number increases with Rayleigh numbers.
- The characteristics of streamlines characteristics effect the isotherms, and since the isotherms are produced from nondimensional temperature contours, observations about the Nusselt number can be made by examining the isotherms.
- The case of HHHC has produces the lowest Nusselt number compared to the other cases.
- Symmetric cases (HHHC, VHVC) produce symmetric streamlines and isotherms, with the same manner, asymmetric cases (HHVC, VHHC) generate asymmetric streamlined and isotherms.
- At high Rayleigh numbers, the Nusselt numbers formed by the VHVC case are high, while at low Rayleigh numbers, the Nusselt numbers are low.
- Generally, asymmetric cases (HHVC, VHHC) produce same Nusselt numbers.
- The Nusselt numbers calculated from the cold wall and the hot wall are very close to each other especially at symmetry cases.

Nomenclature

c	lattice speed, [ms^{-1}]
$\vec{c}_k$	discrete lattice velocity set, [ms^{-1}]
c_s	lattice speed of sound, [ms^{-1}]
c_p	isobaric spesicif heat, [Jkg^{-1}K^{-1}]
F	External force (=$\rho g \beta [T - T_{mean}]$)
f_k	discrete density distribution function, [kgm^{-3}]
g	gravitational acceleration, [ms^{-2}]
g_k	discrete temperature distribution function, [K]
h	Convective heat transfer coefficient, [K]
k	Thermal conductivity, [Wm^{-1}K^{-1}]
L	length of domain, [m]
Nu	Nusselt number (=hL/k)
p	Pressure, [Pa]
Pr	Prandtl number (=$\mu c_p/k$)
Ra	Rayleigh number (=$g\beta\Delta T L^3/\nu\alpha$)
q"	heat flux, [Wm^{-2}]
T	temperature, [K]
t	time, [s]
$\vec{u}$	velocity vector
W	width of domain, [m]
w_k	weighting factors
$\vec{x}$	position vector
x, y	2D Cartesian coordinates
	Greek Symbol
α	thermal diffusivity, [m^{2}s^{-1}]
β	thermal expansion coefficient, [K^{-1}]
ΔT	temperature differences between hot and cold walls, [K]
δ	lattice unit (distance between to neighboring lattice nodes), [m]
δ_t	time step, [s]
θ	Nondimensonal temperature =($T - T_F/T_W - T_F$)
μ	dynamic viscosity, [kgms^{-1}]
ν	kinematic viscosity, [m^{2}s^{-1}]
ρ	density, [kgm^{-3}]
ω	Collision for momentum transfer [s^{-1}]
ω_T	Collision for energy transfer [s^{-1}]
	Acronyms
HHHC	Horizontal hot horizontal cold
HHVC	Horizontal hot vertical cold
VHHC	Vertical hot horizontal cold
VHVC	Vertical hot vertical cold

Article Information Form

Authors Contribution

Authors contributed equally to the study.

The Declaration of Conflict of Interest/ Common Interest

No conflict of interest or common interest has been declared by authors.

The Declaration of Ethics Committee Approval

This study does not require ethics committee permission or any special permission.

The Declaration of Research and Publication Ethics

Authors of the paper declare that they comply with the scientific, ethical and quotation rules of SAUJS in all processes of the paper and that they do not make any falsification on the data collected. In addition, they declare that Sakarya University Journal of Science and its editorial board have no responsibility for any ethical violations that may be encountered, and that this study has not been evaluated in any academic publication environment other than Sakarya University Journal of Science.

References

[1] G. De Vahl Davis, "Natural convection of air in a square cavity: A benchmark numerical solution," International Journal for Numerical Methods Fluids, vol. 3, pp. 249-264, May/June 1983.

[2] S. Ostrach, "Natural convection in enclosure," ASME Journal of Heat and Mass Transfer, vol. 110, pp. 1175-1190, 1988.

[3] J. L. Lage, A. Bejan, "The resonance of natural convection in an enclosure heated periodically from the side," International Journal of Heat and Mass Transfer, vol. 36, issue. 8, pp.2027-2038, 1993.

[4] M. Mahdavi, M. Sharifpur, H. Ghodsinezhad, J. P. Meyer, "Experimental and numerical study of the thermal and hydrodynamic characteristics of laminar natural convective flow inside a rectangular cavity with water, ethylene glycol-water and air," Experimental Thermal and Fluid Science, vol. 78, pp.50-64, 2016.

[5] N. Ugurbilek, Z. Sert, F. Selimefendigil, H. F. Oztop, "3D laminar natural convection in a cubical enclosure with gradually changing partitions," International Communications in Heat and Mass Transfer, vol. 133, 105932, 2022.

[6] T. Pesso, S. Piva, "Laminar natural convection in a square cavity: Low Prandtl numbers and large density differences," International Journal of Heat and Mass Transfer, vol. 53, issue. 3-4, pp. 1036-1043, 2009.

[7] M. Turkyilmazoglu, "Exponential nonuniform wall heating of a square cavity and natural convection," Chinese Journal of Physics, vol. 77, pp. 2122-2135, 2022.

[8] M. Turkyilmazoglu, "Driven flow motion by a dually moving lid of a square cavity," European Journal of Mechanics / B Fluids, vol. 94, pp. 17-29, 2022.

[9] Y. H. Qian, D. D'Humieres, P. Lalemand, "Lattice BGK models for Navier–Stokes equation," Europhysics Letters, vol. 17, issue.6, pp. 479-484, 1992.

[10] S. Y. Chen, G. D. Doolen, "Lattice Boltzmann method for fluid flows," Annual Reviews Fluid Mechanics, vol. 30, pp. 329-364, 1998.

[11] Y. H. Qian, S. Succi, S. A. Orszag, "Recent advance in lattice Boltzmann computing," Annual Reviews of Computational Physics III, pp. 195-242, 1995.

[12] C. K. Aidun, "Lattice-Boltzmann method for complex flows," Annual Reviews of Fluid Mechanics, vol. 42, pp. 439-472, 2010.

[13] L. Chen, Q. Kang, Y. Mu, Y. L. He, W. Q. Tao, "A critical review of the pseudopotential multiphase lattice

Boltzmann model: Methods and applications," International Journal of Heat and Mass Transfer, vol. 76, 210236, 2014.

[14] I. Taymaz, E. Aslan, A. C. Benim, "Numerical investigation of incompressible fluid flow and heat transfer across a bluff body in a channel flow," Thermal Science, vol. 19, issue. 2, pp. 537-547, 2015

[15] P. Karki, A. K. Yadav, D. A. Perumal, "Lattice Boltzmann computation of two dimensional differentially heated cavity of incompressible fluid with different aspect ratios," in International Conference on Intelligent Computing, Instrumentation and Control Technologies-2017, Kannur, Kerala, 2017, pp. 1540-1550.

[16] Y. Feng, S. Guo, W. Tao, P. Sagaut, "Regularized thermal lattice Boltzmann method for natural convection with large temperature differences," International Journal of Heat and Mass Transfer, vol. 125, pp. 1379-1391, 2018.

[17] Y. Wei, H. Yang, H. S. Dou, Z. Lin, Z. Wang, Y. Qian, "A novel two-dimensional coupled lattice Boltzmann model for thermal incompressible flows," Applied Mathematics and Computation, vol. 339, pp. 556-567, 2018.

[18] P. Pichandi, S. Anbalagan, "Natural convection heat transfer and fluid flow analysis in a 2D square enclosure with sinusoidal wave and different convection mechanism," International Journal of Numerical Methods for Heat & Fluid Flow, vol. 29, issue. 9, pp. 2158-2188, 2018.

[19] M. F. Hasan, M. M. Molla, S. Siddiqa, A. M. Khan, "Mesescopic CUDA 3D MRT-LBM simulaion of natural convection of poer-law fluids in a differentially heated cubic cavity with a machine learning cross-validation," Arabian Journal for Science and Engineering, vol. 49, pp 10687-10723, 2024.

[20] T. Li, C. Zhu, Z. Gao, P. Lei, S. Liu, "GPU parallel compuing based on PF-LBM method for simulation dendrites growth under natural convection condition," AIP Advances vol. 14, issue. 2, 025240, 2024.

[21] Ansys-Fluent, version 20.0, Canonsburf PA, Ansys-Inc, 2019

[22] P. L. Bahatnagar, E. P. Gross, M. Krook, "A Model for Collisional Processes in Gases I: Small Amplitude Processes in Charged and Neutral One-Component System," Physical Review, vol. 94, issue. 3, pp. 511-525, 1954.

[23] A. A. Mohamad, Lattice Boltzmann Fundamentals and Engineering Applications with Computer Codes. 2nd ed., London: Springer, 2019.

Sakarya Üniversitesi Fen Bilimleri Dergisi
Sakarya University Journal of Science

e-ISSN : 2147-835X
Publisher : Sakarya University

Vol. 29, No. 2, 160-170, 2025
DOI: https://doi.org/10.16984/saufenbilder.1590407

Research Article

Structural Properties and Bandgap Energy of Ga-doped Garnet-type $Li_7La_3Zr_2O_{12}$ (LLZO) Solid Electrolyte Depending on Sintering Atmosphere

Sevda Saran

Selçuk University, Faculty of Science, Department of Physics, Konya, Türkiye, sevdaaktas@selcuk.edu.tr, ror.org/045hgzm75

ARTICLE INFO

Keywords:
Garnet-type LLZO solid electrolyte
Sintering atmosphere
DRS
Band gap energy

Article History:
Received: 24.11.2024
Revised: 07.02.2025
Accepted: 05.03.2025
Online Available: 15.04.2025

ABSTRACT

Developing solid-state batteries for higher energy densities and safety has been a popular research subject in recent years. Since their first report, $Li_7La_3Zr_2O_{12}$ (LLZO) solid electrolytes have attracted extended attention due to their high ionic conductivity, chemical stability, and wide electrochemical window. Although LLZO fulfills all the requirements for high energy density and a longer lifespan, its intrinsic electronic conductivity accelerates the Li dendrite growth short-circuiting the battery. In this study, we have applied air and oxygen sintering atmospheres to prepare two types of Ga-doped LLZO pellets, to identify the effect of sintering atmospheres on the physical properties such as crystal phase, ionic conductivity, roughness, and electronic band gap energy (E_g). Both the crystal structures were found to be in cubic phase with a relatively small amount of secondary phase impurities. On the other hand, the oxygen-sintered sample showed better properties with high ionic conductivity of $1.04x10^{-4}$ Scm^{-1}, lower surface root-mean-square roughness of 0.1833 µm, and a relative density of 90.5%. Furthermore, the electronic indirect band gap energy of the oxygen-sintered sample was larger, E_g=5.77 eV, which is desired for lower electrical conductivity. It is important to note that the precise determination of E_g values of powders would be erroneous through Ultraviolet-Visible (UV-Vis) absorption spectroscopy due to the scattering effects of solids. So, to the best of our knowledge, for the first time, this study reports E_g values of oxygen and air-sintered LLZO determined by the Kubelka-Munk model on Ultraviolet-Visible-Near Infra-Red (UV-Vis-NIR) diffuse reflectance spectroscopy.

1. Introduction

Garnet-type $Li_7La_3Zr_2O_{12}$ (LLZO) solid electrolytes can be replaced with organic flammable non-safe liquid electrolytes due to their advantages, such as high ionic conductivity, wide electrochemical window, and compatibility with high-voltage cathodes and Li metal anodes. These benefits make garnet-type solid electrolytes increasingly recognized as a good candidate for solid-state batteries compared to other solid electrolytes such as sulfides, halides, NaSICONs, and polymers [1-8]. However, when Li metal is used as the anode, lithium dendrites grow through LLZO and lead to a battery short-circuit which is challenging to prevent [9-10].

Although recent studies have indicated the factors contributing to dendrite formation, such as the low relative density of LLZO, preexisting cracks on the surface, and poor contact between LLZO and Li metal, this issue has not been solved [11-13]. On the other hand, Han et al. reported that the electronic conductivity of LLZO is mostly responsible for Li dendrite formation [14]. Although the solid electrolyte and the alloy interphase at the Li/Solid electrolyte interface have low electronic conductivities, the enlarged 'effective' contact area between Li and the solid electrolyte could lower the potential in the solid electrolyte, accelerating Li dendrite formation [14]. This means that at even very low electronic conductivities Li dendrites can grow. In recent

Cite as: S. Saran (2025). Structural Properties and Bandgap Energy of Ga-doped Garnet-type Li7La3Zr2O12 (LLZO) Solid Electrolyte Depending on Sintering Atmosphere, *Sakarya University Journal of Science*, 29(2), 160-170. https://doi.org/10.16984/saufenbilder.1590407

reports, to suppress the growth of Li dendrites, electronic insulator layers have been deposited on the LLZO surface, and some compounds have been introduced into LLZO to contract electron-blocking properties, especially at the grain boundaries [15-16].

On the other hand, most current research on LLZO is focused on improving the ionic conductivity with single-element and dual-element doping strategies. However, while these strategies increase the ionic conductivity, they may also increase the electronic conductivity. That's why it is important to consider a lower electronic conductivity while considering a high ionic conductivity. In that manner, UV-Vis diffuse reflectance spectroscopy (DRS) might be a convenient and easy way to determine the electronic band gap of newly synthesized solid electrolytes with high ionic conductivity.

The electronic band gap (E_g) that can be analyzed experimentally with Ultraviolet-Visible (UV-Vis) spectroscopy is an important feature of materials that determines their intrinsic electronic conductivity. In literature, the theoretical indirect band gap of LLZO is given as 5.918 eV [17]. Experimentally, there are a few studies on the electronic band gap of LLZO. In one of the reports, a polished transparent LLZO which is complicated to prepare was studied with UV-Vis absorption spectroscopy. In that study, the indirect electronic band gap was determined as 5.46 eV for Al-doped LLZO [18]. Another study reported a band gap of ~ 6 eV determined via the UV-Vis absorption spectroscopy of LLZO powders [19].

Although UV-Vis absorption spectroscopy is frequently used to analyze the band gap of solutions or thin films, it is an inadequate technique to determine the band gap value of powder samples. Because in the case of powders, the estimated wavelength of absorbed photons is erroneous due to the scattering effects [20-21]. On the other hand, the dispersion of LLZO in most liquids is not stable [22]. Consequently, the LLZO powder concentration in the liquid changes in time which is an obstacle to estimating the accurate E_g with the UV-Vis absorption spectroscopy.

DRS is a widely used technique to analyze the optical properties of powder samples [23-24]. To the best of our knowledge, the powder LLZO solid electrolyte has not been characterized via diffuse reflectance spectroscopy. The electronic band gap of materials like other physical and chemical properties can be affected by the synthesis conditions and methods, we therefore synthesized Ga-doped LLZO solid electrolytes in oxygen (O_2) and air atmospheres [25]. Then, crystal structures, morphologies, relative densities, electronic bandgaps, and ionic conductivities of the samples were characterized.

2. General Methods

$Li_{6.4}Ga_{0.2}La_3Zr_2O_{12}$ solid electrolytes were synthesized with a solid-state reaction method by using the precursor powders (purity: 99.9%) of Li_2CO_3, Ga_2O_3, La_2O_3, and ZrO_2 in the desired stoichiometric ratio according to the following chemical equation [26],

$$3.2Li_2CO_3 + 0.1Ga_2O_3 + 1.5La_2O_3 + 2ZrO_2 \rightarrow Li_{6.4}Ga_{0.2}La_3Zr_2O_{12} + 3.2CO_2 \quad (1)$$

The powder mixture was then subjected to a series of ball milling and heat treatments. First, the mixture was ball milled in isopropanol at 400 rpm with 6-minute reversal intervals for 5 hours using a Retsch PM100 ball grinder. The powders were then dried to remove the isopropanol. Next, the dried powders were heated at 900 ºC for 8 hours in air and O_2 atmospheres. In the second step, the ball milling was repeated at 350 rpm in a dry system. Finally, the powders were pressed into pellets with a diameter of 13 mm and a thickness of 1 mm. Before sintering at 1230 ºC for 2 hours in air and O_2, the pellets were buried in the mother powder to compensate for Li loss at high temperatures. Before characterization, pellets were polished to remove the mother powder and have a smooth surface.

Crystal structure analysis was conducted using a Bruker D8 X-ray diffractometer (XRD) with a CuKα source. Electrochemical impedance spectroscopy (EIS) of the samples with silver-coated electrodes was measured between two cylindrical stainless steel at room temperature in the frequency range of 1-10^5 Hz with an AC

signal of 10 mV by Gamry PCI4/750 Potentiostat.

While a ZEISS LS 10 model scanning electron microscopy (SEM) was used to image the micron-sized area of the pellet's surface, a Filmetrics Profilm 3D model optical profilometer was used to image the millimeter-sized area (2 mm x 2 mm) of the pellet's surface.

The theoretical and experimental densities of the pellets were calculated using the lattice parameters obtained from XRD data refinement and the Archimedes principle, respectively. Bruker, VERTEX70 model spectrometer was used to collect Fourier transform infrared (FTIR) data between wavenumber of 4000-400 cm^{-1} in air. Finally, to study the electronic band gap energy of powder samples with a thickness of 1 mm, the Ultraviolet-Visible Near-Infra-Red (UV-Vis-NIR) diffuse reflection spectrum was collected between 200-1400 nm wavelengths with Shimadzu, ISR-603 spectrometer and the Ultraviolet-Visible (UV-Vis) absorption spectrum was collected between 200-1400 nm wavelengths with Jasco, V-670 spectrometer.

3. Results and Discussion

XRD data in Fig. 1 shows that the atmosphere does not play a crucial role in the crystal structures, since all the samples heated in air and O_2 have the same diffraction peaks. When the samples are sintered at 1230 °C, diffraction peaks become sharper, indicating a well-crystallized cubic phase (2241539-CIF) [27]. The XRD data were analyzed with MAUD software [28]. According to the Rietveld refinement shown in Table 1, $Li_{6.4}Ga_{0.2}La_3Zr_2O_{12}$ formed with a space group of I-43d and a lattice parameter of 12.98Å. Moreover, these samples show a relatively small amount of secondary phases $La_2Zr_2O_7$ and La_2O_3. These secondary phases are common impurity phases in literature and usually form at high temperatures [29].

SEM micrographs of the pellet surfaces after the final sintering step at 1230 °C in O_2 and air are illustrated in Fig. 2. As seen from the images, the pellet-O_2 has a denser structure, which is similar to that reported in the literature [30]. In other words, larger pores, where Li dendrites can easily grow, are observed between grains for the pellet-air. During the sintering process, oxygen occupies the pores and helps densification by diffusion into the LLZO lattice at high temperatures. On the other hand, trapped air within the pores induces structures with lower density [31].

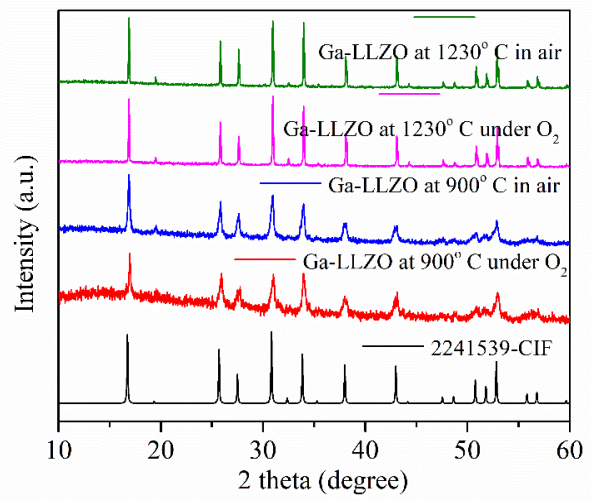

Figure 1. XRD data of LLZO samples pre-calcined at 900 °C and finally sintered at 1230 °C in air and O_2 atmospheres

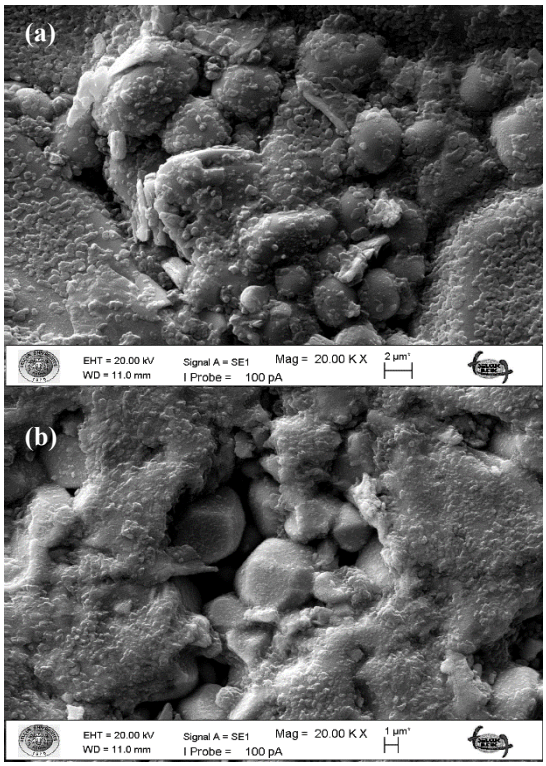

Figure 2. SEM micrographs of the surface of Ga-doped LLZO pellet sintered at 1230 °C in a) O_2 and b) air atmospheres

Table 1. Crystal structure analysis of the samples sintered in air and O_2 at 1230 °C

Sintering Atm.	Phase composition	α	β	γ	a (Å)	c (Å)	Geometry	SG	%(Weight)
Air	$Li_{6.4}Ga_{0.2}La_3Zr_2O_{12}$	90	90	90	12.98	-	Cubic	I-43d	98.64
	$La_2Zr_2O_7$	90	90	90	10.81	-	Cubic	Fd-3m:2	0.13
	La_2O_3	90	90	120	3.94	6.13	Hexagonal	P63/mmc	1.23
O_2	$Li_{6.4}Ga_{0.2}La_3Zr_2O_{12}$	90	90	90	12.98	-	Cubic	I-43d	99.14
	$La_2Zr_2O_7$	90	90	90	11.04	-	Cubic	Fd-3m:2	0.37
	La_2O_3	90	90	120	3.94	6.13	Hexagonal	P63/mmc	0.49

Table 2. The total ionic conductivity and density values of $Li_{6.4}Ga_{0.2}La_3Zr_2O_{12}$ pellets sintered in air and O_2 at 1230 °C

Sintering Atm.	σ_{total} (S cm^{-1})	Apparent Density (g/cm^3)	Theoretical Density (g/cm^3)	Relative Density (%)
O_2	1.04x10^{-4}	4.6677	5.156	90.529
Air	5.17x10^{-5}	4.4638	5.150	86.675

SEM results are also confirmed by measuring the apparent density of the pellets using the Archimedes principle. In Table 2, the results are given in terms of relative density calculated through the relation, $\frac{\rho}{\rho_t}x100$ where ρ is the measured density and ρ_t is the theoretical density determined using the lattice parameter obtained by XRD data via the equation, $\rho_t = ZM/Na^3$ where Z is the number of atoms per unit cell (8), M is the molecular mass, N is Avogadro's number and a is the unit cell parameter [32-33]. The relative density is higher for pellet-O_2 (90.5 %) than pellet-air (86.7 %) showing well-matched results with the SEM observations.

The increased density of the pellet due to the O_2 sintering atmosphere could be further confirmed with a 3D optical profilometer which creates a 3D surface image for measuring surface profiles and roughness. Fig. 3 shows the topography images taken over an area of 2 mm x 2 mm of the pellets with an optical profilometer. Before optical imaging, the surfaces of the pellets were polished with a 1200-grit number polishing paper. Although polishing conditions were the same, the pellet-O_2 showed a shiner surface than pellet-air which can also reflect some information about porosity. The topography plot of the pellet-O_2 shows cracks which are most probably due to over-sintering time in O_2, which we can conclude that the pellets can have a denser structure in a shorter time in the O_2 atmosphere compared to air [30]. Although

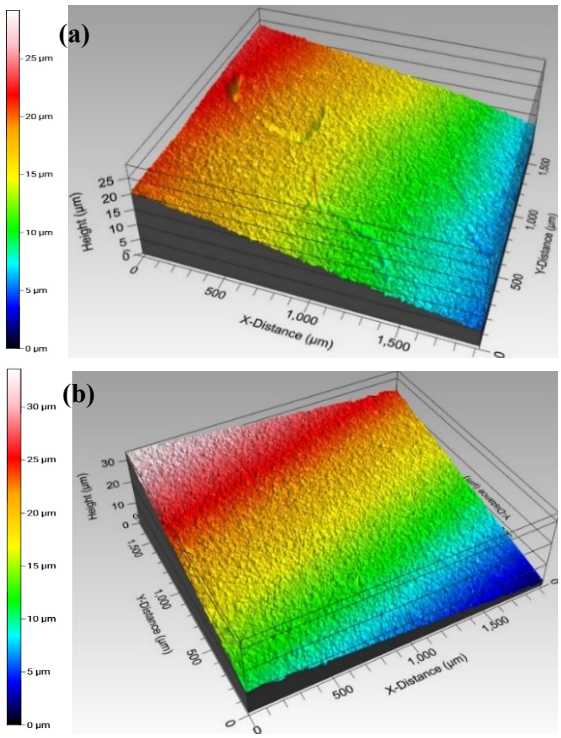

Figure 3. Topography plots of Ga-LLZO pellet-O_2 and b) Ga-LLZO pellet-air

pellet-O_2 shows cracks on its surface, it still has a lower root-mean-square (RMS) roughness of *Rq*= 0.1833 µm compared to the pellet-air (*Rq*= 0.4035 µm). The higher roughness of the pellet-air could be related to the higher porosity. A lower surface roughness is desired for a solid electrolyte since it helps to create an intimate interface with the Li anode. On the other hand, if there is limited physical contact between the solid electrolyte and the Li anode, the local electric fields arise leading to the acceleration of Li dendrite growth.

Although 3D optical profilometer, a facile and low-priced technique, is not widely used for LLZO surface roughness measurement, it gives comparable results obtained with an atomic force microscope (AFM) in the literature [34-36].

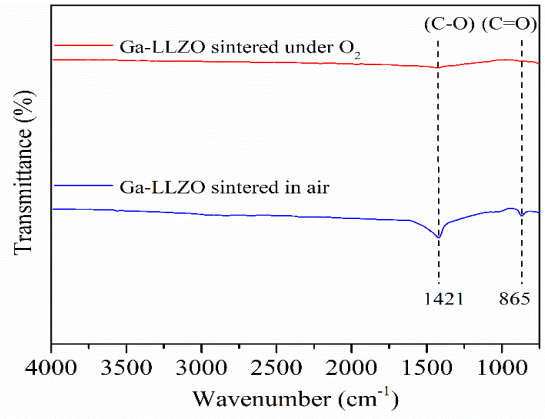

Figure 4. FTIR spectra of Ga-LLZO powder sintered in air and O_2

Before measuring the FTIR spectra in Fig. 4, pellets were polished in air, then milled in a mortar, and immediately stored in a vacuum bag, so the exposure time to air was minimized. The peaks observed at 1421 cm^{-1} and 865 cm^{-1} are attributed to the impurity of Li_2CO_3 forms when LLZO is exposed to air [37-39]. Li_2CO_3 is an undesired impurity since it makes LLZO surface lithiophobic where a limited physical contact at the solid electrolyte-Li anode interface is induced [40]. Although all conditions were the same, these peaks are absent for LLZO sintered in O_2, indicating that LLZO sintered in O_2 can be more resistive to the formation of Li_2CO_3 or it is impossible to remove Li_2CO_3 formed during air sintering from grain boundaries of LLZO. Since the poor contact at the solid electrolyte-Li anode interface accelerates the Li dendrite growth, we can conclude from the FTIR results that the life span of a battery could be longer with an LLZO pellet-O_2.

Nyquist plots of the EIS spectra of the LLZO pellets on both side silver electrodes and the equivalent circuit used to fit the experimental data are given in Fig. 5. The equivalent circuit is composed of resistors (R) and constant phase elements (CPE) which refers to a non-ideal capacitor [41]. The impedance of CPE is described as $Z_{CPE} = 1/Q(jw)^n$, here $j = \sqrt{-1}$, w is the frequency, Q is a numerical value with dimension Ss^n and n is a constant between 0 and 1. The abbreviations b, gb, and el refer to the bulk (interior of the grains), grain boundary (interface of the grains), and electrode (interface of silver electrode and pellet), respectively.

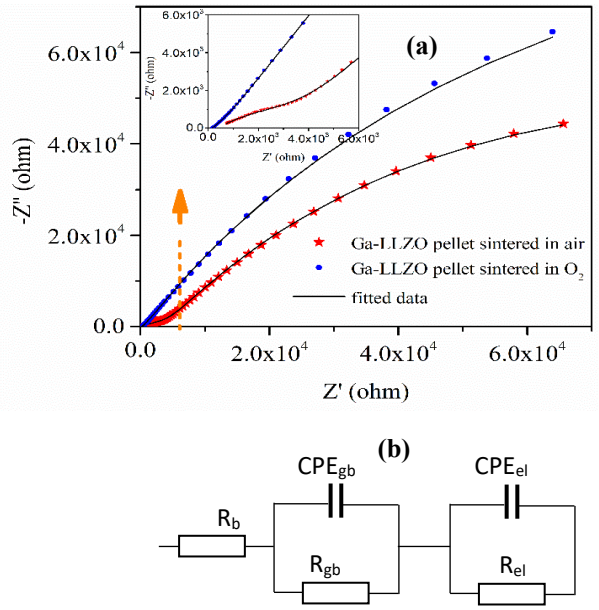

Figure 5. Nyquist plots of EIS measured at room temperature and fitted data of a) Ga-LLZO pellet-O_2 and Ga-LLZO pellet-air, and b) schematic representation of the equivalent circuit that fits experimental data

According to fit results summarized in Table 3, the $Li_{6.4}Ga_{0.2}La_3Zr_2O_{12}$ pellet sintered in O_2 shows lower bulk (R_b) and grain boundary resistances (R_{gb}) compared to the pellet sintered in air. The ionic conductivities of the pellets were calculated with the equation, $\sigma = \left(\frac{1}{R}\right)\left(\frac{l}{a}\right)$ where R is the total resistivity (bulk and grain boundary), l is the thickness of the pellet and a is the area of the electrode [42]. The oxygen-sintered pellet shows a higher ionic conductivity of $1.04x10^{-4}$ Scm^{-1}, almost two times more than that of the air sintered pellet (Table 2). Since all the conditions except the sintering atmosphere are the same for both samples, the low relative density (high porosity) is probably the main reason for lower ionic conductivity.

High density and high ionic conductivity alone may not be sufficient to suppress the growth of Li dendrites. In addition to high ionic conductivity, a good solid electrolyte should also have low electronic conductivity. As far as we know, the electronic band gap of LLZO depending on synthesis conditions has not been

studied with diffuse reflectance spectroscopy. In Fig. 6, the UV-Vis-NIR diffuse reflectance spectrum of oxygen and air-sintered powders is illustrated. As we mentioned earlier, in the case of powders, UV-Vis diffuse reflectance spectroscopy is a more convenient technique to determine the electronic band gap since UV-Vis absorption spectroscopy does not consider the scattering effects.

Table 3. Fitting results of the analysis of the impedance data of $Li_{6.4}Ga_{0.2}La_3Zr_2O_{12}$ pellets sintered in air and O_2 at 1230 °C using the equivalent circuit in Fig. 5 (b), χ^2 is the square of the standard deviation

Sintering Atmosphere	R_b (Ω)	R_{gb} (Ω)	$Q_{gb}(Ss^n)$	n_{gb}	χ^2
O_2	123.3	$1.79x10^3$	$8.14x10^{-5}$	$3.53x10^{-1}$	$1.37x10^{-4}$
Air	386.2	$3.46x10^3$	$4.15x10^{-6}$	$4.26x10^{-1}$	$3.14x10^{-4}$

However, DRS may be limited for the samples containing mixed powders for systematic underestimation of the E_g values. Fortunately, an automated method has been developed to get accurate E_g values for mixed powders. In the automated method, several concerns have been taken into account as reported in the literature [20]. On the other hand, the thickness of the sample is very important for accurate determination of E_g values. The thickness of the sample should not cause a significant change in its reflectance. That's why for accurate determination of the E_g values, a thickness of more than 0.5 mm must be used to avoid any light transmission [43].

The diffuse reflectance spectroscopy is analyzed with the Kubelka-Munk model,

$$[F(R_\infty)hv]^\gamma = B(hv - E_g) \quad (2)$$

where $F(R_\infty)$ is the Kubelka-Munk function, hv is the incident photon energy, E_g is the electronic band gap, B is a constant, and γ is related to the nature of the band transition, e.g., $\gamma = 1/2$, $\gamma = 2$, for direct and indirect band transitions, respectively [21, 44]. The Kubelka-

Munk function is expressed with the equation (3),

$$F(R_\infty) = \frac{K}{S} = \frac{(1-R_\infty)^2}{2R_\infty} \quad (3)$$

where R_∞ is the diffuse reflectance of an optically thick sample, K and S are absorption and scattering coefficients, respectively [24]. E_g values of the samples can easily be determined

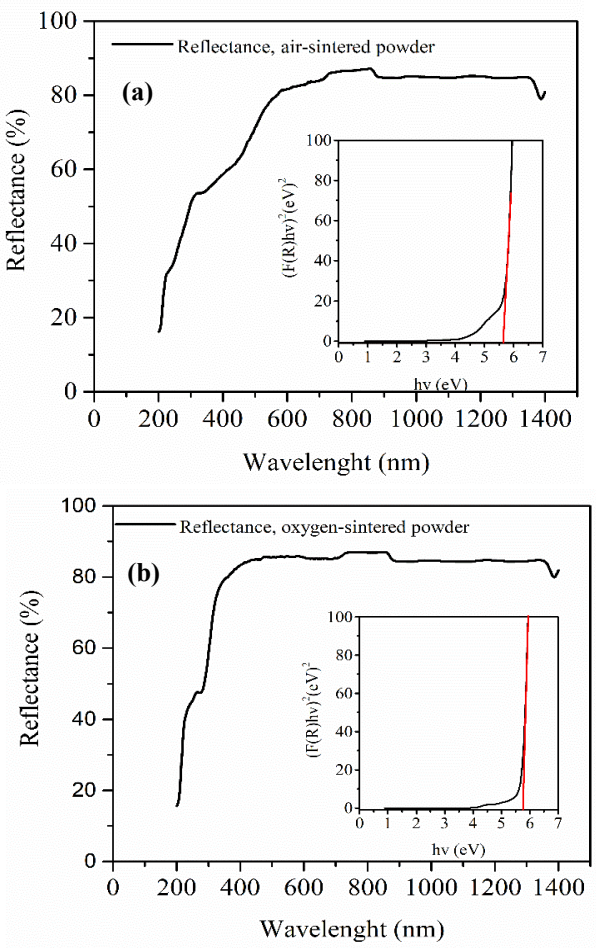

Figure 6. UV-Vis-NIR diffuse reflectance spectra of Ga-LLZO powder sintered in a) air and b) O_2, the inner graphs were obtained using the reflectance data

by extrapolating the linear part of the $[F(R)hv]^\gamma$ vs hv plot to the x-axis shown as an inner graph in Fig. 6 [43-44]. The indirect electronic band gap

Table 4. Comparison of bandgap energy values obtained with UV-Vis. absorption spectroscopy and UV-Vis. diffuse reflectance spectroscopy

		Indirect bandgap energy (eV)	Direct bandgap energy (eV)
Air-sintered powder	UV-Vis DRS. technique	5.64	5.18
	UV-Vis Abs. technique	5.42	4.63
Oxygen-sintered powder	UV-Vis DRS. technique	5.77	5
	UV-Vis Abs. technique	4.92	3.85

energy of the oxygen-sintered sample, $E_{g\text{-}O2}$=5.77 eV, is relatively larger than that of the air-sintered sample, $E_{g\text{-}air}$=5.64 eV. The direct band gap also widens when the sample is sintered in oxygen ($E_{g\text{-}O2}$=5.18 eV, $E_{g\text{-}air}$=5 eV). The literature reports that point defects like oxygen vacancies narrow the band gap by inducing intra-band gap energy states [45]. On the other hand, it is well-known that high temperatures, required for dense LLZO pellets, lead Li to evaporate by creating oxygen vacancies to preserve the charge neutrality of the lattice [46-47]. That's why we can say that low partial oxygen pressure in the air most likely increased the oxygen vacancy concentration and caused a band gap narrowing [48].

We have also obtained bandgap energies of the samples by using the UV-Vis. absorption spectroscopy to compare the results of UV-Vis. diffuse reflectance spectroscopy. LLZO powders were dispersed in a solvent for UV-Vis absorption measurements. As shown in Table 4., narrower bandgaps were obtained with the UV-Vis. absorption spectroscopy technique for both samples. Furthermore, while the obtained band gap energy of the oxygen-sintered sample is relatively larger than that of the air-sintered sample with the UV-Vis DRS technique, it is obtained narrower with the UV-Vis absorption technique. The difference is most probably due to the fact that LLZO powder is not soluble, and the dispersion of the powders is not stable. That's why scattering effects occur which are not taken into account by the UV-Vis absorption spectroscopy.

4. Conclusion

In this work, we have studied the effects of sintering atmospheres on the optical, structural, and conductivity properties of Ga-doped LLZO solid electrolytes. Both samples sintered in oxygen and air showed a cubic crystal structure. The electronic indirect band gap energy of the oxygen-sintered sample was obtained relatively larger, E_g=5.77 eV, compared to the air-sintered sample with UV-Vis DRS spectroscopy. SEM and 3D optical profilometer results indicated that the oxygen-sintered pellet was formed with lower porosity consequently leading to a higher relative density.

Furthermore, ionic conductivities also confirmed the density difference of the pellets. According to the EIS results, the oxygen-sintered pellet has a high ionic conductivity of 1.04×10^{-4} Scm^{-1}. Also, the 3D optical profilometer measured a lower surface root-mean-square (RMS) roughness of *Rq*= 0.1833 μm for the oxygen-sintered pellet which can be useful to create an intimate interface with Li anode to suppress the Li growth.

Article Information Form

Funding
The author has received financial support from Selçuk University of Priority Area Research Project with the number of 21406002 for the research, authorship or publication of this study.

The Declaration of Conflict of Interest/ Common Interest
No conflict of interest or common interest has been declared by the authors.

The Declaration of Ethics Committee Approval
This study does not require ethics committee permission or any special permission.

The Declaration of Research and Publication Ethics
The author of the paper declare that they comply with the scientific, ethical and quotation rules of

SAUJS in all processes of the paper and that they do not make any falsification on the data collected. In addition, they declare that Sakarya University Journal of Science and its editorial board have no responsibility for any ethical violations that may be encountered, and that this study has not been evaluated in any academic publication environment other than Sakarya University Journal of Science.

References

[1] A. Machín, C. Morant, F. Márquez, "Advancements and Challenges in Solid-State Battery Technology: An In-Depth Review of Solid Electrolytes and Anode Innovations," Batteries, vol. 10, no. 1, pp. 29, 2024.

[2] W. Feng, Y. Zhao, Y. Xia, "Solid Interfaces for the Garnet Electrolytes," Advanced Materials, vol. 36, pp. 2306111, 2024.

[3] F. Öksüzoğlu, Ş. Ateş, O. M. Özkendir, G. Çelik, Y. R. Eker, H. Baveghar, "Structure and ionic conductivity of NASICON-type LATP solid electrolyte synthesized by the solid-state method," Ceramics International, 2024.

[4] S. Saran, Y. R. Eker, Ş. Ateş, G. Çelik, H. Baveghar, O. M. Özkendir, W. Klysubun, "The effect of Ti to the crystal structure of $Li_{7-3x}M_xLa_3Zr_{1.8}Ti_{0.2}O_{12}$ (M=Ga, In) garnet-type solid electrolytes as a second dopant," Advances in Applied Ceramics, vol. 121, pp. 238-246, 2022.

[5] S. Saran, O. M. Özkendir, Ü. Atav, "The effect of two different substituted atoms in lithium positions on the structure of garnet-type solid electrolytes," Turkish Journal of Physics, vol. 45, no. 3, pp. 148-158, 2021.

[6] Y. Li, Z. Cao, Z. Jiang, Y. Cao, J. Liu, L. Wang, "Synergistic effect of Ga and Yb co-doping on the structure and ionic conductivity of $Li_7La_3Zr_2O_{12}$ ceramics," Ionics, vol. 28, pp. 5321-5331, 2022.

[7] W. Xia, B. Xu, H. Duan, Y. Guo, H. Kang, Li, H. Liu, "Ionic conductivity and air stability of Al-doped $Li_7La_3Zr_2O_{12}$ sintered in alumina and Pt crucibles," ACS applied materials & interfaces, vol.8, no. 8, pp. 5335-5342, 2016.

[8] S. Saran, Y. R. Eker, "Synthesis, structural and conductive properties of Nd doped garnet-type $Li_7La_3Zr_2O_{12}$ Li-ion conductor," Current Applied Physics, vol. 41, pp.1-6, 2022.

[9] C. Li, Y. Qiu, Y. Zhao, W. Feng, "Self assembled electron blocking and lithiophilic interface towards dendrite-free solid-state lithium battery," Chinese Chemical Letters, vol. 35, no. 4, pp. 108846, 2024.

[10] M. Philipp, B. Gadermaier, P. Posch, I. Hanzu, S. Ganschow, M. Meven, D. Rettenwander, G. J. Redhammer, H. M. R. Wilkening, "The Electronic Conductivity of Single Crystalline Ga-Stabilized Cubic $Li_7La_3Zr_2O_{12}$: A Technologically Relevant Parameter for All-Solid-State Batteries," Advanced Materials Interfaces, vol. 7, pp. 2000450, 2020.

[11] K. Kerman, A. Luntz, V. Viswanathan, Y. M. Chiang, Z. B. Chen, "Review-practical challenges hindering the development of solid-state Li-ion batteries," Journal of Electrochemical Society, vol. 164, pp. A1731–A1744, 2017.

[12] C. L. Tsai, V. Roddatis, C. V. Chandran, Q. Ma, S. Uhlenbruck, M. Bram, P. Heitjans, O. Guillon, "$Li_7La_3Zr_2O_{12}$ interface modification for Li dendrite prevention," ACS Applied Materials Interfaces, vol. 8, pp. 10617-10626, 2016.

[13] A. Sharafi, E. Kazyak, A. L. Davis, S. Yu, T. Thompson, D. J. Siegel, N. P. Dasgupta, J. Sakamoto, "Surface chemistry mechanism of ultra-low interfacial

resistance in the solid-state electrolyte $Li_7La_3Zr_2O_{12}$," Chemistry of Materials, 29, 7961-7968, 2017.

[14] F. Han, A. S. Westover, J. Yue, X. Fan, F. Wang, M. Chi, D. N. Leonard, N. J. Dudney, H. Wang, C. Wang, "High electronic conductivity as the origin of lithium dendrite formation within solid electrolytes, "Nature Energy, vol. 4, pp. 187-196, 2019.

[15] C. Du, Z. Li, Z. Fang, X. Fang, X. Ji, Z. Zhao, D. Liu, R. Li, X. Xiang, H. Yang, "Constructing a three-dimensional continuous grain boundary with lithium-ion conductivity and electron blocking property in LLZO to suppress lithium dendrites," Journal of Alloys and Compounds, vol. 1003, pp. 175769, 2024.

[16] X. Xiang, Z. Fang, C. Du, Z. Zhao, J. Chen, Y. Zhang, Q. Shen, "Constructing electron-blocking grain boundaries in garnet to suppress lithium dendrite growth," Journal of Advanced Ceramics, vol. 13, no. 2, pp. 166-175, 2024.

[17] C. Xu, Y. Xue, M. Zhang, N. Liao, "Atomic-level designed LLZO electrolyte for LTO electrode in all-solid-state batteries with superb interfacial properties," Surfaces and Interfaces, vol. 40, pp. 103128, 2023.

[18] T. Thompson, S. Yu, L. Williams, R. D. Schmidt, R. Garcia-Mendez, J. Wolfenstine, J. Sakamoto, "Electrochemical window of the Li-ion solid electrolyte $Li_7La_3Zr_2O_{12}$," ACS Energy Letters, vol. 2, no. 2, pp. 462-468, 2017.

[19] K. Ajith, P. C. Selvin, K. P. Abhilash, P. Sivaraj, B. Nalini, G. G. Soundarya, "A correlative study on electrochemical and optical properties of LLZO ($Li_7La_3Zr_2O_{12}$) garnet electrolyte," Materials Today: Proceedings, vol. 50, pp. 2836-2839, 2022.

[20] A. Escobedo-Morales, I. I. Ruiz-López, M. D. Ruiz-Peralta, L. Tepech-Carrillo, M. Sánchez-Cantú, J. E. Moreno-Orea, "Automated method for the determination of the band gap energy of pure and mixed powder samples using diffuse reflectance spectroscopy," Heliyon, vol. 5, no. 4, 2019.

[21] A. E. Morales, E. S. Mora, U. Pal, "Use of diffuse reflectance spectroscopy for optical characterization of un-supported nanostructures," Revista mexicana de física, vol. 53, no. 5, pp. 18-22, 2007.

[22] H. Lü, X. Chen, Q. Sun, N. Zhao, X. Guo, "Uniform garnet nanoparticle dispersion in composite polymer electrolytes, "Acta Physico-Chimica Sinica, pp. 2305016, 2024.

[23] T. Eickhoff, P. Grosse, W. Theiss, "Diffuse reflectance spectroscopy of powders," Vibrational spectroscopy, vol. 1, no. 2, pp. 229-233, 1990.

[24] H. Ranjan Sahu, G. Ranga Rao, "Characterization of combustion synthesized zirconia powder by UV-vis, IR and other techniques," Bulletin of Materials Science, vol. 23, pp. 349-354, 2000.

[25] E. O. Filatova, A. S. Konashuk, "Interpretation of the changing the band gap of Al_2O_3 depending on its crystalline form: connection with different local symmetries," The Journal of Physical Chemistry C, vol. 119, no. 35, pp. 20755-20761, 2015.

[26] S. Rezaee, H. Araghi, H. Noshad, Z. Zabihi, "Physical characteristics of fluorine-doped lithium oxide as advanced material for solid-electrolyte-interphase applications of lithium-air batteries," The European Physical Journal Plus, vol. 137, no. 1194, 2022.

[27] L. Robben, R. Merzlyakova, P. Heitjans, T. M. Gesing, "Symmetry reduction due to gallium substitution in the garnet Li6.43(2) Ga0.52 (3) La2. 67 (4) Zr2O12," Acta Crystallographica Section E: Crystallographic Communications, vol. 72, no. 3, pp. 287-289, 2016.

[28] Ç. Kaya, F. Bondino, E. Magnano, H. Gündoğmuş, I. Ulfat, W. Klysubun, O. M. Ozkendir, "Influence of Gallium Substitution on the Crystal and Electronic Properties of $Li5Ca_{1-x}Ga_xLa_3Zr_2O_{12}$ Solid State Battery Electrolyte," Journal of Electron Spectroscopy and Related Phenomena, vol. 226, pp. 45-52, 2018.

[29] M. Matsui, K. Takahashi, K. Sakamoto, Hirano, Y. Takeda, O. Yamamoto, N. Imanishi, "Phase stability of a garnet-type lithium ion conductor $Li_7La_3Zr_2O_{12}$," Dalton Transactions, vol. 43, no. 3, pp.1019-1024, 2024.

[30] F. Shen, W. Guo, D. Zeng, Z. Sun, J. Gao, J. Li, X. Han, "A simple and highly efficient method toward high-density garnet-type LLZTO solid-state electrolyte," ACS applied materials & interfaces, vol. 12, no. 27, pp. 30313-30319, 2020.

[31] Y. Li, Z. Wang, C. Li, Y. Cao, X. Guo, "Densification and ionic-conduction improvement of lithium garnet solid electrolytes by flowing oxygen sintering," Journal of Power sources, vol. 248, pp. 642-646, 2014.

[32] B. P. Dubey, A. Sahoo, V. Thangadurai, Y. Sharma, "Morphological, dielectric and transport properties of garnet-type Li6.25+yAl0.25La3Zr2-yMnyO12 (y= 0, 0.05, 0.1, and 0.2)," Solid State Ionics, vol. 351, pp. 115339, 2020.

[33] A. B. Gadkari, T. J. Shinde, P. N. Vasambekar, "Structural analysis of Sm^{3+} doped nanocrystalline Mg-Cd ferrites prepared by oxalate co-precipitation method," Materials characterization, vol. 60, no. 11, pp. 1328-1333, 2009.

[34] W. Feng, X. Dong, P. Li, Y. Wang, Y. Xia, "Interfacial modification of Li/Garnet electrolyte by a lithiophilic and breathing interlayer," Journal of Power Sources, vol. 419, pp. 91-98, 2019.

[35] V. Raj, K. G. Naik, B. S. Vishnugopi, A. K. Rana, A. S. Manning, S. R. Mahapatra, D. Mitlin, "Dendrite Growth-Microstructure-Stress-Interrelations in Garnet Solid-State Electrolyte," Advanced Energy Materials, vol. 14, no. 15, pp. 2303062, 2024.

[36] A. Baniya, A. Gurung, J. Pokharel, K. Chen, R. Pathak, B. S. Lamsal, Q. Qiao, "Mitigating interfacial mismatch between lithium metal and garnet-type solid electrolyte by depositing metal nitride lithiophilic interlayer," ACS Applied Energy Materials, vol. 5, no. 1, pp. 648-657, 2022.

[37] J. Zhang, R. Yu, J. Li, H. Zhai, G. Tan, X. Tang, "Transformation of undesired Li_2CO_3 into lithiophilic layer via double replacement reaction for garnet electrolyte engineering," Energy & Environmental Materials, vol. 5, no. 3, pp. 962-968, 2022.

[38] H. Huo, Y. Chen, N. Zhao, X. Lin, J. Luo, X. Yang, X. Sun, "In-situ formed Li_2CO_3-free garnet/Li interface by rapid acid treatment for dendrite-free solid-state batteries," Nano Energy, vol. 61, pp. 119-125, 2019.

[39] F. Du, T. Liao, T. Ye, Y. Wu, G. Guo, K. Zhu, Z. Xie, "Room-temperature, all-solid-state lithium metal batteries enabled by a moderate-temperature formation method," Journal of Materials Science, vol. 1, no. 10, 2022.

[40] L. Wang, Y. Lu, C. Zheng, M. Cai, F. Xu, Z. Wen, "In Situ Construction of a Lithiophilic and Electronically Insulating Multifunctional Hybrid Layer Based on the Principle of Hydrolysis for a Stable Garnet/Li Interface," Advanced Functional Materials, pp. 2402971, 2024.

[41] S. Gunaydin, H. Miyazaki, S. Saran, H. Baveghar, G. Celik, M. Harfouche, M. Abdellatief, O. M. Ozkendir, "The Effect of $CrFe_2O_4$ Addition on the Ionic Conductivity Properties of Manganese-Substituted $LiFeO_2$ Material, "Journal of

Electronic Materials, vol. 53, pp. 367-379, 2024.

[42] F. Öksüzoğlu, S. Ateş, O. M. Özkendir, G. Çelik, Y. R. Eker, H. Baveghar, M. A. Basyooni-M. Kabatas, "The Impact of Boron Compounds on the Structure and Ionic Conductivity of LATP Solid Electrolytes," Materials, vol. 17, pp. 3846, 2024.

[43] S. Landi Jr, I. R. Segundo, E. Freitas, M. Vasilevskiy, J. Carneiro, C. J. Tavares, "Use and misuse of the Kubelka-Munk function to obtain the band gap energy from diffuse reflectance measurements," Solid state communications, vol. 341, pp. 114573, 2022.

[44] P. Makuła, M. Pacia, W. Macyk, "How to correctly determine the band gap energy of modified semiconductor photocatalysts based on UV-Vis spectra," The journal of physical chemistry letters, vol. 9, no. 23, pp. 6814-6817, 2018.

[45] A. Sarkar, C. Loho, L. Velasco, T. Thomas, S. S. Bhattacharya, H. Hahn, R. Djenadic, "Multicomponent equiatomic rare earth oxides with a narrow band gap and associated praseodymium multivalency," Dalton transactions, vol. 46, no. 36, pp. 12167-12176, 2017.

[46] N. Kuganathan, M. J. Rushton, R. W. Grimes, J. A. Kilner, E. I. Gkanas, A. Chroneos, "Self-diffusion in garnet-type $Li_7La_3Zr_2O_{12}$ solid electrolytes," Scientific Reports, vol. 11, no. 1, pp. 451, 2021.

[47] Z. Ma, B. Zhao, W. Li, S. Jiao, W. Gong, H. Qiu, M. Yu, "Effects of fabrication atmosphere conditions on the physico-chemical properties of garnet electrolyte," Ionics, vol. 28, no. 6, pp. 2673-2683, 2022.

[48] X. Ping, Q. Zheng, B. Meng, W. Lin, Y. Chen, C. Fang, W. Liang, "Influence of sintering atmosphere on the phase, microstructure, and lithium-ion conductivity of the Al-doped $Li_7La_3Zr_2O_{12}$ solid electrolyte," Ceramics International, vol. 48, no. 18, pp. 25689-25695, 2022.

Sakarya Üniversitesi Fen Bilimleri Dergisi
Sakarya University Journal of Science

e-ISSN : 2147-835X
Publisher : Sakarya University

Vol. 29, No. 2, 171-179, 2025
DOI: https://doi.org/10.16984/saufenbilder.1625576

Research Article

Three-Point Bending Behavior of 3D-Printed Tough-PLA Lattice Beams: Effects of Lattice Topology and Beam Width

Yasin Kuddusi Kutucu, Muhammed Muaz Yalcın*

Sakarya University, Faculty of Science, Department of Mechanical Engineering, Sakarya, Türkiye, ykutucu@sakarya.edu.tr, myalcin@sakarya.edu.tr, ror.org/04ttnw109
*Corresponding Author

ARTICLE INFO

Keywords:
Bending
Tough-PLA
PLA filament
Energy absorption
Specific energy absorption

Article History:
Received: 23.01.2025
Revised: 04.02.2025
Accepted: 05.03.2025
Online Available: 15.04.2025

ABSTRACT

This study investigates the fabrication of single and double-row lattice beams utilizing three distinct lattice structures: cubic, octet, and body-centered cubic (BCC), using Tough-PLA filament. This material exhibits similar plastic deformation characteristics to traditional PLA filament but possesses superior strength. Mechanical properties of the bulk Tough-PLA filament were evaluated through standard tensile testing. Subsequently, to assess the influence of lattice configuration and beam width, the single and double-row beams were subjected to three-point bending tests. The experimental data were analyzed in terms of specific energy absorption, crush force efficiency, and specific force value, allowing for comparisons with existing literature to identify the most effective parameters. The findings indicate that the octet lattice structure, featuring angled struts, is the most efficient design as beam thickness increases. Conversely, for single-row beams with narrower widths, the BCC lattice—with both vertical and angled struts—emerges as the optimal design. Additionally, cubic lattices consistently displayed the least favorable performance due to their reliance on vertical struts across all beam widths examined.

1. Introduction

The investigation into the three-point bending of polymer beams represents a significant domain within materials science, especially concerning the elucidation of mechanical properties and the behavior of polymer-based materials when subjected to flexural stresses. This approach is commonly employed to assess the bending strength and stiffness of diverse polymer composites, particularly those augmented with fibers, which markedly improve their mechanical properties. The three-point bending test offers significant advantages owing to its straightforward methodology and the direct correlation it creates between the applied load and the resultant deflection. This facilitates a precise evaluation of material behavior when subjected to bending stresses.

PLA is a biodegradable thermoplastic sourced from renewable materials, frequently employed in the fabrication of lattice structures owing to its advantageous mechanical characteristics and processing simplicity. Studies have shown that integrating supplementary materials, including epoxy and milled glass fibers, significantly improves the mechanical properties of PLA lattices. Mustafa et al. [1] demonstrated that PLA lattices, when filled with epoxy and reinforced with milled glass fibers, showed enhanced mechanical properties in comparison to pure PLA lattices. This finding underscores the potential of multi-material structures to optimize performance. Additionally, Egan et al. [2] highlighted the critical role of design and processing strategies in influencing the mechanical properties of 3D-printed polymer lattices. They observed that changes in relative density and unit cell geometry have a substantial

Cite as: Y. K. Kutucu, M. M. Yalcın (2025). Three-Point Bending Behavior of 3D-Printed Tough-PLA Lattice Beams: Effects of Lattice Topology and Beam Width, *Sakarya University Journal of Science*, 29(2), 171-179. https://doi.org/10.16984/saufenbilder.1625576

impact on both the elastic modulus and overall strength of these materials.

The techniques utilized in the fabrication of PLA lattice structures significantly influence their overall performance. Fused filament fabrication (FFF) represents a prevalent technique that facilitates meticulous regulation of lattice geometry and porosity. Sala et al. [3] conducted an investigation into the potential of Fused Filament Fabrication (FFF) for the production of bespoke lattice structures. Their findings illustrate that alterations in nozzle diameter and the design of unit cells can result in notable variations in mechanical performance. Furthermore, the implementation of sophisticated methodologies, such as direct ink writing (DIW), has demonstrated the capability to enable the fabrication of intricate lattice structures that are difficult to realize through conventional approaches. Nevertheless, the citation associated with DIW fails to explicitly discuss PLA or its associated mechanical properties; thus, it has been omitted to enhance clarity.

The mechanical performance of PLA lattice beams is significantly affected by their structural characteristics, including factors such as porosity and the design of the unit cell. Egan et al. emphasized that a rise in porosity typically results in a reduction of the elastic modulus, a phenomenon that can be beneficial in contexts necessitating lightweight structures endowed with energy absorption properties [4]. Furthermore, an examination of the failure behavior of these lattices under compressive forces has been conducted, demonstrating that the hybrid properties of PLA lattices can offer efficient load-bearing solutions while preserving a lightweight structure [5]. This holds significant importance in the realm of biomedical applications, wherein the mechanical characteristics of scaffolds are required to closely resemble those of natural bone in order to facilitate effective tissue integration [6].

Polymer beam bending is affected by many factors. These include the polymer type, reinforcing components, and testing configuration. Cyclic three-point bending studies on biomimetic beams showed hysteresis in loading and unloading curves due to material friction and deformation [7]. Understanding polymers' viscoelastic properties, which can cause energy loss under cyclic loading, is crucial. In addition, adding fibers like glass or carbon has increased the bending strength of polymer composites. Glass fibers in I-beams increase stiffness and reduce buckling under transverse stresses. This shows that fiber reinforcement improves mechanical performance [8].

Composite materials can improve polymer beam mechanical properties. Epoxy mortars can repair and strengthen timber beams, increasing their load-bearing capacity in three-point bending tests [9]. This approach strengthens beams and extends their service life, making them suitable for existing structures. The fibers used in polymer composites greatly affect their performance. Polymer mortars made with untreated sisal fibers had the highest ultimate strength. The mechanical properties of treated fibers were inferior, highlighting the importance of fiber treatment and selection in improving mechanical performance [10].

The role of temperature in the bending behavior of polymer beams is another critical aspect. The mechanical properties of polymers can vary significantly with temperature, affecting their performance under load. For instance, introduced an experimental device to measure the temperature of deflection under load, emphasizing the thermomechanical characteristics of polymeric materials during three-point bending tests [11]. This is particularly relevant in applications where polymers are exposed to varying thermal conditions, as it can lead to changes in stiffness and strength. In addition to the mechanical properties, the bond strength between reinforcing materials and the polymer matrix plays a vital role in the overall performance of composite beams.

Research by demonstrated that the bond strength of carbon fiber-reinforced polymer (CFRP) bars in timber beams significantly influenced their bending performance, with increases in ultimate strength observed in reinforced beams compared to unreinforced controls [12]. This underscores the necessity of ensuring strong interfacial adhesion to maximize the benefits of

reinforcement in polymer beams. Furthermore, the bending failure behavior of polymer beams can be complex, often involving multiple failure modes. For instance, explored the correlations among different bending test methods for dental hard resins, revealing that the choice of testing method can significantly impact the measured flexural strength [13]. This finding is crucial for standardizing testing procedures in polymer beam evaluations to ensure consistent and reliable results across different studies.

The use of advanced materials such as graphene and basalt fibers in polymer composites has also gained attention in recent years. evaluated the mechanical properties of polyester composites reinforced with graphene, demonstrating significant enhancements in strength and stiffness through three-point bending tests [14]. Similarly, basalt fiber-modified concrete beams were investigated, highlighting the unique mechanical properties conferred by these advanced materials under bending loads [15]. These innovations in material science open new avenues for developing high-performance polymer beams suitable for demanding applications.

In recent studies, the bending behavior of functionally graded materials (FGMs) has been explored using advanced theoretical frameworks. For instance, Dang [16] proposed a third-order shear deformation theory that accounts for geometrical imperfections and thermal environments, demonstrating its applicability to rotating FGMs resting on elastic foundations. This theory enhances the understanding of how material properties vary across the beam's thickness, which is crucial for accurately predicting bending responses. Moreover, the bending characteristics of hybrid materials have been investigated, as seen in the work by Wu et al. [17], who studied a combined beam made of welded thin-walled steel and camphor pine wood. Their experimental results revealed significant improvements in bending performance due to the synergistic effects of the materials used, suggesting that innovative combinations can lead to enhanced structural capabilities. Such findings are pivotal for developing sustainable construction materials that leverage the strengths of both wood and steel.

Recent studies have shown that the flexural behavior of lattice beams can be significantly influenced by their structural design and material composition. For instance, Wang et al. [18] investigated composite sandwich beams with lattice-web reinforcement, demonstrating that the nonlinear flexural behavior is enhanced through the integration of glass fiber-reinforced plastics (GFRP) with a wood core. Their experimental and numerical analyses revealed that the lattice-web structure effectively improves flexural rigidity, which is crucial for applications requiring lightweight yet strong materials. Similarly, Cuan-Urquizo and Bhaskar [19] highlighted the flexural elasticity of woodpile lattice beams, noting that despite the practical interest in such materials, comprehensive studies on their flexural response remain limited. This indicates a gap in literature that necessitates further exploration to fully understand the mechanics of lattice beams.

Moreover, the mechanical properties of lattice beams can be actively controlled through innovative design approaches. Sinha and Mukhopadhyay [20] discussed the potential for on-demand programming of elastic moduli in lattice materials, suggesting that the stiffness and failure strength can be dynamically adjusted. This capability is particularly relevant for applications in adaptive structures where performance needs to be tailored to varying conditions. The integration of advanced materials, such as hybrid composites with bamboo layers and lattice ribs, has also been shown to enhance the flexural behavior of beams, as demonstrated by Zhang et al. [21]. Their experimental investigation highlighted the benefits of using hybrid materials to achieve superior mechanical performance.

In this study, three different lattice topologies were used to create lattice beams with different widths. Accordingly, a tensile test was conducted to obtain the mechanical properties of the bulk material of Tough-PLA filament. Following this, lattice beams were tested under 3-point bending loading conditions. Different crashworthiness

parameters were examined to obtain the most sufficient lattice beam design.

2. Materials and Method

Polylactic acid (PLA) filament represents one of the most prevalent materials utilized in the realm of 3D printing, which is a prominent technique within the broader category of additive manufacturing processes. The family of PLA filaments encompasses various types, each exhibiting distinct mechanical properties. Among these materials, PLA-Flex exhibits an exceptionally high capacity for plastic deformation, whereas Tough-PLA demonstrates superior impact resistance compared to traditional PLA filaments. In the present investigation, Tough-PLA filament was selected due to its comparable plastic deformation characteristics to those of PLA filament while also providing enhanced strength properties. Initially, to ascertain the mechanical properties of the Tough-PLA material, a dog bone tensile test specimen (refer to Figure 1) was fabricated in accordance with ISO-527 standards. Subsequently, tensile tests were conducted in strict adherence to these established standards. The mechanical properties derived from the conducted test are presented in Table 1 below.

Figure 1. Tensile test specimens are made up of Tough-PLA (after the tensile test)

Table 1. Mechanical properties of Tough-PLA bulk material

Youngs Modulus (MPa)	Yield stress (MPa)	Tensile strength (MPa)	Elongation at break (%)
2550	39	55	8.6

The design of lattice beam specimens was conducted utilizing three distinct lattice configurations: cubic, octet, and body-centered-cubic (BCC). Each specimen exhibits a relative density of 30%, resulting in an approximate equivalence in weight among them. Beams were generated through the arrangement of 16 of these lattice geometries positioned adjacently, configured in the shape of cubes, each possessing a unit dimension of 10 mm. The beam specimens were systematically categorized into two distinct groups, and a thorough analysis was conducted to evaluate the impact of beam width on their performance. In the initial set of beam specimens, a solitary row of cages was implemented throughout the length of the beam. Conversely, in the subsequent set of beam specimens, two rows of cages were employed in parallel along the length of the beam. Figure 2 illustrates the unit lattice structures as viewed from the opposing side. Figure 3 illustrates both the lateral and frontal perspectives of the beam specimen, accompanied by two rows of lattices positioned adjacent to it, along with the corresponding dimensions.

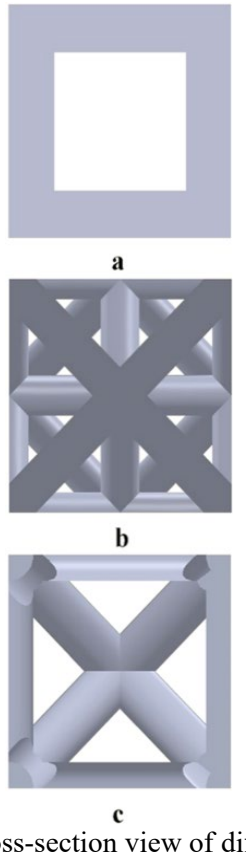

Figure 2. Cross-section view of different lattice topologies a) cubic, b) octet, and c) BCC

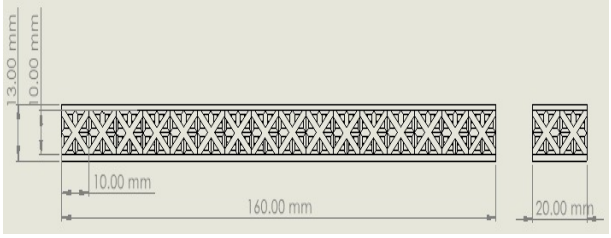

Figure 3. Longitudinal and cross-section views of octet lattice beams with dimensions

The 3-point bending tests conducted on all lattice beam specimens utilized a universal MTS brand device, which possesses a capacity of 100 kN. The tests were carried out at a speed of 2 mm/min, as illustrated in Figure 4.

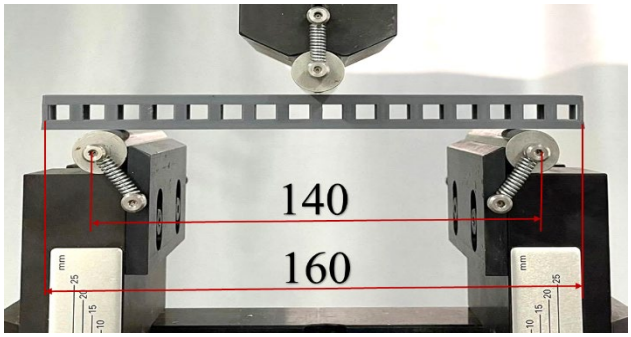

Figure 4. 3-point bending test setup

2.1. Crashworthiness parameters

To determine whether or not a structure is crashworthy, it is necessary to locate the crashworthiness indication. The literature [22, 23] states that in order to qualitatively analyze the crashworthiness of the beam constructions under three-point bending performance, three parameters were proposed. These parameters are specified as load-carrying capacity (LC), energy absorption (EA), and specific energy absorption (SEA). According to this study, the crashworthiness of auxetic beams is evaluated using three different indications. A structure's load-bearing capacity, often known as LC, is the maximum force that can be exerted on it as a result of the force story. Assuming that the force-displacement curve is taken into consideration, the EA provides an indication of the amount of energy that is absorbed by the lattice beam structure for a particular displacement value. In light of this, the EA can be described as follows:

$$EA = \int_0^d F(y)\, dy \tag{1}$$

where F(y) is the instantaneous load carried by the beam structure, and d is the compression displacement. The specific energy absorption, described as the energy absorbed per unit mass, has been broadly used as:

$$SEA = \frac{EA}{m} \tag{2}$$

where m is the mass of the lattice beam structure and is calculated for the length between the fixed supports.

3. Results and Discussion

The 3-point bending tests conducted on the lattices utilized in this study were performed a minimum of two times to ensure the reliability and repeatability of the obtained results.

3.1. Single-row lattice beams

Figure 5 presents a comparative analysis of the force-displacement curves corresponding to single-row cubic, octet, and body-centered cubic (BCC) lattices collectively. It is important to highlight that the cubic lattice is characterized by the presence of only vertical struts, while the octet lattice is distinguished by its incorporation of angled struts. Conversely, the body-centered cubic (BCC) lattice exhibits a configuration characterized by the presence of both vertical and angled struts. This arrangement represents a synthesis of the structural elements found in both cubic and octet lattices. Upon conducting an analysis of the curves, it becomes evident that the total displacement value attains its maximum in the cubic beam.

It is important to highlight that the abrupt decrease in force observed in the cubic beam transpires at significantly lower force and displacement values compared to the other two specimen types. Indeed, the specimen exhibiting the body-centered cubic (BCC) structure demonstrated the highest recorded maximum force value, which was approximately 332 N. Subsequent to this event, the octet specimen achieved a commendable second place by attaining a force measurement of 300 N. The cubic beam exhibited a reduction of 50% in comparison to its octet counterpart, maintaining a consistent force of approximately 200 N. Analysis of the force curves obtained from the specimens indicates that they exhibit comparable stiffness during the initial phase of testing. Regarding the characteristics of force, it is evident that all specimens, with the exception of the cubic lattice, demonstrate a notable similarity. Nonetheless, the octet beam exhibits a

hook-like configuration, in contrast to the BCC beam, which demonstrates a more linear decline.

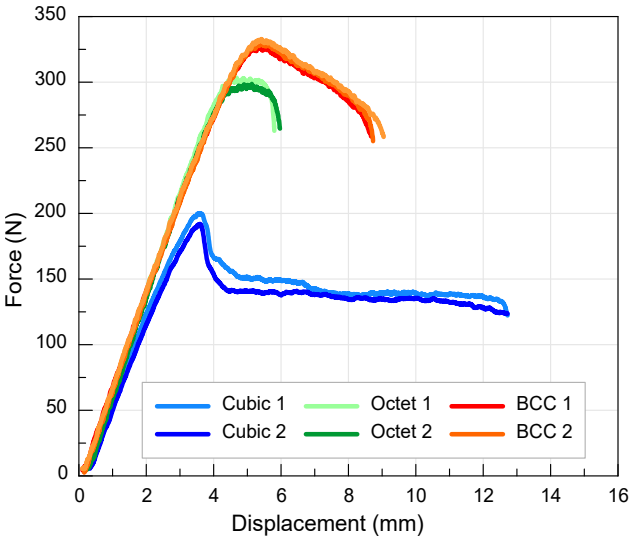

Figure 5. Force-displacement curves of the single-row cubic, octet, and BCC lattice beams

3.2. Double-row lattice beams

The force-displacement curves for the specimens featuring two cages aligned in the direction of the cage length following the completion of the bending tests are presented collectively in Figure 6. The observation that the force curves of the various cage types exhibit a remarkable degree of coincidence is significant as it underscores the efficacy of the manufacturing process employed. The characteristics of the force are evidently analogous to those observed in their single-row counterparts. The configuration of the octet beam, characterized by its hook-like shape, bears resemblance to that of its single-row equivalents, particularly in relation to the abrupt decline observed in the cubic cage structure. Similarly, the linear decline observed in the BCC specimen closely resembles that of the other specimen group.

Nevertheless, it is observed that the force curves associated with the octet and body-centered cubic (BCC) structures exhibit a displacement in comparison to their single-row counterparts. Upon examination of the force curves, it becomes evident that the force values exhibit an upward shift in comparison to their single-row counterparts. The observed enhancements in the maximum force values for cubic, octet, and BCC beams were quantified at 125%, 95%, and 130%, respectively. This observation is significant as it illustrates that the octet lattice increasingly asserts its dominance regarding force enhancement as the number of rows escalates.

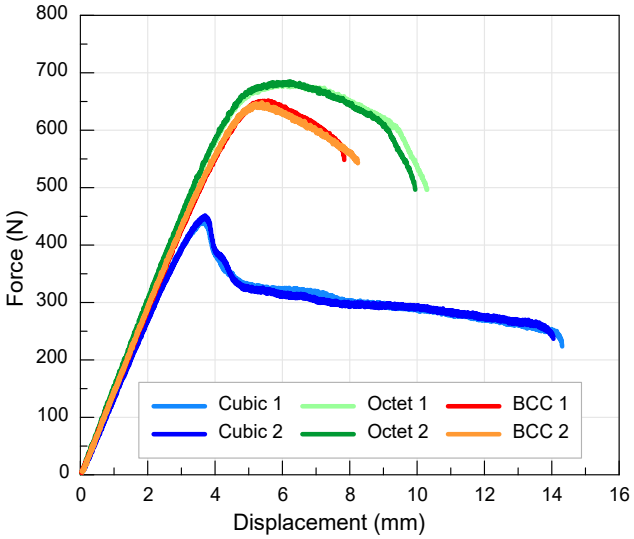

Figure 6. Force-displacement curves of the double-row cubic, octet, and BCC lattice beams

The parameters related to the crashworthiness of the beam specimens are collectively presented in Table 2. To ascertain the optimal design of the beam specimens, a comprehensive examination of various parameters was conducted. This included an analysis of specific energy absorption, specific load-carrying capacity, and crush force efficiency, alongside the evaluation of the energy absorbed by the specimens. Within the context of these parameters, the specific energy absorption parameter is determined by calculating the ratio of the absorbed energy to the weight of the specimen. Conversely, the crush force efficiency parameter is derived from the ratio of the average force value exerted on the beam specimen to the maximum force value recorded.

Furthermore, the specific force value is determined by calculating the ratio of the maximum force exerted by the beam to the weight of the specimen. The analysis of the data presented in the table indicates that the maximum energy is achieved within the octet lattice configuration of the two-row beam specimens. Indeed, the octet specimen demonstrated an energy absorption of approximately 5J, which is 25% greater than that of the cubic specimen. Given that the relative densities of the specimens, and consequently their weights, are comparable,

it is evident that an increase in energy will result in elevated specific energy absorption values.

Certainly, the octet beams once more yielded the highest SEA value observed. It is noteworthy that the BCC beam, possessing approximately double the energy and SEA values compared to the octet beam in single-row specimens, exhibits values that are roughly 35% lower than those of the octet beam in two-row specimens. This suggests that lattice elements arranged at an angle provide enhanced efficiency in load-bearing capacity for broader beams. Following the assessment conducted regarding the CFE value, it can be concluded that the optimal scenario is achieved in the two-row octet beam, despite the fact that all samples exhibit nearly comparable values. The observed data indicates that the SFV value exhibits a comparable variation to that of the CFE value. Upon careful consideration of the various parameters involved, it can be concluded that the most effective specimens for single-row beams are those characterized by a body-centered cubic (BCC) structure, while octet beams demonstrate superior efficiency in the context of double-row configurations. Consequently, when considering a single-row beam, it is advisable to favor the BCC lattice, which integrates both vertical and angled struts. In analogous situations where the implementation of a double-row beam is anticipated, it becomes evident that the selection of the octet lattice is the more suitable option, given that it exclusively comprises angled struts.

Table 2. Energy absorption efficiency parameters of the cubic, octet and BCC lattice beams

Specimen configuration		Weight (g)	Crushing displacement (mm)	F_{mean} (N)	F_{max} (N)	Absorbed energy (J)	Specific energy absorption (J/g)	Crush force efficiency (%)	Specific force value (N/g)
Single row	Cubic	11	3.69	108	200	0.4	0.036	54	18.2
			3.66	101	192	0.37	0.034	52	17.5
	Octet		5.47	183	303	1	0.09	60	27.6
			5.4	176	298	0.95	0.086	59	27.1
	BCC		5.72	189	327	1.08	0.098	58	29.7
			5.8	193	330	1.12	0.101	58	30.0
Double row	Cubic	22	14.3	286	443	4.1	0.19	64	40.3
			14.1	284	451	4.0	0.18	63	41.0
	Octet		9.7	505	684	4.9	0.22	74	62.3
			9.4	500	685	4.7	0.21	73	62.3
	BCC		7.9	446	652	3.5	0.16	68	59.3
			8.4	443	649	3.7	0.17	68	59.0

4. Conclusion

The investigation involved conducting 3-point bending tests on beam specimens that were engineered from various lattice structures, specifically cubic, octet, and body-centered cubic (BCC), and fabricated using a 3D printing technique. In the fabrication of the beams, PLA filament was utilized, and tensile tests were conducted in accordance with established standards for material characterization. Subsequently, both single and double-row lattices were meticulously fabricated and subjected to testing in order to investigate the influence of beam width. The data acquired from the experiments underwent a thorough analysis to identify the most efficient parameter. Within this framework, various efficiency parameters were employed. The parameters in question are delineated as specific energy absorption, crush force efficiency, and specific force value, in alignment with analogous investigations documented in the existing body of literature. The comprehensive data collected indicates that the octet lattice configuration, characterized by angled separations, demonstrates enhanced efficiency as the beam thickness increases. In the context of single-row beams characterized by narrower widths, the investigation revealed that the BCC lattice configuration, incorporating both vertical and angled struts, emerged as the most appropriate design choice. In the analysis of both lattice widths, it was observed that cubic beams exhibited the least favorable performance,

primarily attributable to the presence of their vertical struts.

In future research endeavors, it would be advantageous to conduct a more extensive investigation that encompasses a broader range of lattice configurations, incorporating various material types and differing lattice dimensions.

Article Information Form

Funding
Authors have not received any financial support for the research, authorship, or publication of this study.

Authors Contribution
Authors contributed equally to the study.

The Declaration of Conflict of Interest/ Common Interest
No conflict of interest or common interest has been declared by authors.

The Declaration of Ethics Committee Approval
This study does not require ethics committee permission or any special permission.

The Declaration of Research and Publication Ethics
Authors of the paper declare that they comply with the scientific, ethical, and quotation rules of SAUJS in all processes of the paper and that they do not make any falsification of the data collected. In addition, they declare that Sakarya University Journal of Science and its editorial board have no responsibility for any ethical violations that may be encountered and that this study has not been evaluated in any academic publication environment other than Sakarya University Journal of Science.

References

[1] A. Mustafa, B. Aloyaydi, S. Sivasankaran, F. Al-Mufadi, "Mechanical properties enhancement in composite material structures of poly-lactic acid/epoxy/milled glass fibers prepared by fused filament fabrication and solution casting", Polymer Composites, vol. 42, no. 12, p. 6847-6866, 2021.

[2] P. Egan, N. Khatri, M. Parab, A. Arefin, "Mechanics of 3-d printed polymer lattices with varied design and processing strategies", Polymers, vol. 14, no. 24, p. 5515, 2022.

[3] R. Sala, S. Regondi, R. Pugliese, "Design data and finite element analysis of 3d printed poly(ε-caprolactone)-based lattice scaffolds: Influence of type of unit cell, porosity, and nozzle diameter on the mechanical behavior", Eng—advances in Engineering, vol. 3, no. 1, p. 9-23, 2021.

[4] P. Egan, X. Wang, H. Greutert, K. Shea, K. Wuertz-Kozak, S. Ferguson, "Mechanical and biological characterization of 3-D printed lattices", 3-D Printing and Additive Manufacturing, vol. 6, no. 2, p. 73-81, 2019.

[5] R. Hasan, N. A. Rosli, S. Mat, M. R. Alkahari, "Failure behaviour of 3-D printed ABS lattice structure under compression", International Journal of Engineering and Advanced Technology, vol. 9, no. 3, p. 3908-3912, 2020.

[6] P. Egan, K. Shea, S. Ferguson, "Simulated tissue growth for 3-D printed scaffolds", Biomechanics and Modeling in Mechanobiology, vol. 17, no. 5, p. 1481-1495, 2018.

[7] M. Tatari, S. Kamrava, R. Ghosh, H. Nayeb-Hashemi, A. Vaziri, "Bending behavior of biomimetic scale covered beam with tunable stiffness scales", Scientific Reports, vol. 10, no. 1, 2020.

[8] L. Zhu, S. Cao, X. Zhang, L. Li, "Bending failure behavior of the glass fiber reinforced composite i-beams formed by a novel bending pultrusion processing technique", Autex Research Journal, vol. 22, no. 2, p. 172-176, 2022.

[9] S. Carvalho, T. Panzera, A. Christofóro, J. Fiorelli, F. Lahr, R. Freire, "Epoxy mortar timber beam upgrading", International Wood Products Journal, vol. 8, no. 3, p. 146-154, 2017.

[10] N. Benzannache, A. Bezazi, H. Bouchelaghem, M. Boumaaza, F. Scarpa, S. Amziane, "Effects of adding sisal and glass fibers on the mechanical behaviour of concrete polymer", Journal of Building Materials and Structures, vol. 5, no. 1, p. 86-94, 2018.

[11] A. Catangiu, D. Ungureanu, A. Poinescu, I. Gurgu, "Experimental device with data acquisition for measurement of temperature of deflection under load", Scientific Bulletin of Valahia University - Materials and Mechanics, vol. 19, no. 20, p. 31-37, 2023.

[12] M. Corradi, L. Righetti, A. Borri, "Bond strength of composite CFRP reinforcing bars in timber", Materials, vol. 8, no. 7, p. 4034-4049, 2015.

[13] D. Miura, T. Miyasaka, H. Aoki, Y. Aoyagi, Y. Ishida, "Correlations among bending test methods for dental hard resins", Dental Materials Journal, vol. 36, no. 4, p. 491-496, 2017.

[14] M. Bastiurea, M. Rodeanu, D. Dima, M. Murarescu, G. Andrei, "Evaluation of mechanical properties of polyester composite with graphene and graphite through three-point bending test", Applied Mechanics and Materials, vol. 659, p. 22-27, 2014.

[15] Y. Gong, J. Yang, X. He, X. Lyu, & H. Liu, "Structural design calculation of basalt fiber polymer-modified RPC beams subjected to four-point bending", Polymers, vol. 13, no. 19, p. 3261, 2021.

[16] N. Dang, "A third-order shear deformation theory for bending behaviors of rotating FGM beams resting on elastic foundation with geometrical imperfections in thermal environments", Mathematical Problems in Engineering, vol. 2021, p. 1-19, 2021.

[17] C. Wu, J. Duan, Z. Yang, Z. Zhao, Y. Xu, "A novel rectangular-section combined beam of welded thin-walled h-shape steel/camphor pine wood: The bending performance study", Sustainability, vol. 15, no. 9, p. 7450, 2023.

[18] Y. Wang, J. Han, R. Huo, H. Fang, J. Chen, W. Liu, "The flexural behaviour of composite sandwich beams with a lattice-web reinforced wood core", Advances in Structural Engineering, vol. 25, no. 12, p. 2496-2507, 2022.

[19] E. Cuan-Urquizo, A. Bhaskar, "Flexural elasticity of woodpile lattice beams", European Journal of Mechanics - A/Solids, vol. 67, p. 187-199, 2018.

[20] P. Sinha T. Mukhopadhyay, "On-demand contactless programming of nonlinear elastic moduli in hard magnetic soft beam based broadband active lattice materials", Smart Materials and Structures, vol. 32, no. 5, p. 055021, 2023.

[21] F. Zhang, W. Liu, L. Wang, Q. Yao, D. Zhou, H. Fang, "Flexural behavior of hybrid composite beams with a bamboo layer and lattice ribs", Journal of Reinforced Plastics and Composites, vol. 34, no. 7, p. 521-533, 2015.

[22] M. F. Kahraman, S. İriç, K. Genel, “Comparative failure behavior of metal honeycomb structures under bending: A finite element-based study”, Engineering Failure Analysis, vol. 157, p. 107963, 2024.

[23] M. M. Yalçın, “Flexural behavior of 3D-printed carbon fiber-reinforced nylon lattice beams”, Polymers, vol. 16, no. 21, p. 2991, Oct. 2024.

Sakarya Üniversitesi Fen Bilimleri Dergisi
Sakarya University Journal of Science

e-ISSN : 2147-835X
Publisher : Sakarya University

Vol. 29, No. 2, 180-190, 2025
DOI: https://doi.org/10.16984/saufenbilder.1619116

Research Article

Impact of Silicon Dioxide Nanoparticles on Nutritional Composition of Edible Insect: *Galleria mellonella* (Lepidoptera: Pyralidae) Larvae

Ata Eskin[1*], Cem Okan Özer[2]

[1] Nevşehir Hacı Bektaş Veli University, Avanos Vocational School of Fine Arts, Department of Crop and Animal Production, Nevşehir, Türkiye, ataeskin@nevsehir.edu.tr, ror.org/019jds967
[2] Nevşehir Hacı Bektaş Veli University, Faculty of Engineering and Architecture, Department of Food Engineering, Nevşehir, Türkiye, cemokanozer@nevsehir.edu.tr, ror.org/019jds967
[*]Corresponding Author

ARTICLE INFO

Keywords:
Fatty acids
Galleria mellonella
Nutritional composition
Silicon dioxide nanoparticle

Article History:
Received: 13.01.2025
Revised: 24.02.2025
Accepted: 09.03.2025
Online Available: 15.04.2025

ABSTRACT

The present study investigates the impact of SiO_2 NPs (Silicon Dioxide Nanoparticles) (500–60000 ppm) on key chemical parameters including protein, lipid, carbohydrate, moisture, ash, and fatty acid composition in *Galleria mellonella* (Lepidoptera: Pyralidae) larvae, with a view to identifying potential implications for sustainable food systems. It was determined that the protein and carbohydrate contents of larvae fed with high doses (>5000 ppm) of SiO_2 NPs were significantly reduced in comparison to the control group. Moreover, an increment in the dose of SiO_2 NPs resulted in a decrease in the fat content of the larvae. It was found that larvae exposed to 500 and 30000 ppm SiO_2 NPs exhibited a reduction in moisture content. Furthermore, the ash content of all larvae treated with SiO_2 NPs exhibited a significant increase. Finally, an increment in the dose of SiO_2 NPs in the larvae was found to be an increase in the level of palmitic acid and a decrease in the level of oleic acid. These findings demonstrate the importance of evaluating the risks associated with nanoparticle exposure in edible insect-based food products with a view to ensuring food safety and sustainability.

1. Introduction

The global food system is facing two significant challenges: The necessity of feeding an expanding population and the responsibility to minimize its environmental impact [1]. The production of conventional protein sources, such as livestock, is characterized by a high environmental impact such as gas emissions, excessive freshwater use, and large-scale deforestation and is a significant contributor to environmental degradation [2]. It is therefore evident that the examination of sustainable and alternative protein sources has become a crucial field of research and development, with the objective of ensuring global food security [3].

Edible insects, which are an important source of protein, lipids, and some essential components, represent a promising solution to this global challenge [3, 4]. The high protein content and adaptability of The Greater Wax Moth (*Galleria mellonella*) (Lepidoptera: Pyralidae) larvae make them a particularly suitable model for the study of nanoparticle interactions and their nutritional implications. The larvae of the *G. mellonella* represent a particularly noteworthy species within the diverse range of edible insects (it is not consumed directly by humans, generally it is used in zoos for insectivorous creatures). They have attracted considerable interest due to the ease with which they can be cultivated, their high nutritional value, and their adaptability.

The larvae depending on species and stage have been found to contain high levels of lipids (2–62%), and especially oleic and linoleic acids, which are considered essential for human health

Cite as: A. Keskin, C. O. Özer (2025). Impact of Silicon Dioxide Nanoparticles on Nutritional Composition of Edible Insect: Galleria mellonella (Lepidoptera: Pyralidae) Larvae, *Sakarya University Journal of Science*, 29(2), 180-190. https://doi.org/10.16984/saufenbilder.1619116

[5-7]. Furthermore, it is notable that the protein content exceeds averagely 30%. It has been reported that albumins (>45%) and glutelins (>35%) are the dominant proteins in the *G. mellonella* protein composition, with prolamins and globulins also reported [8]. The protein content of *G. mellonella* is considerably higher than that of conventional meat products and several plant-based protein sources [9]. Additionally, it has been indicated that insect proteins are comparatively more digestible than plant proteins [10]. Therefore, their nutritional profile, which includes protein, lipid, and carbohydrate reserves, makes them an attractive dietary substitute to meet the increasing global food demands [11, 12].

Although the potential of *G. mellonella* as a sustainable protein source is evident, it is important to note that the nutritional composition and quality of these larvae can be influenced by environmental exposures [13]. For example, their composition can change with exposure to various stressors such as temperature, humidity, oxygen including external chemicals or nanoparticles. Furthermore, the nutritional composition may also be changed to interactions with components commonly found in nature or food additives utilized in food applications. Silicon dioxide (SiO_2) is a notable component due to its extensive utilization and potential interactions with biological systems. SiO_2 is a metal oxide in its amorphous form and was approved as a food additive by European Food Safety Authority (EFSA) and Food and Drug Administration (FDA) [14, 15].

It has been utilized for several decades as an anti-caking, stabilizer and adsorbent in some foods and dietary foods [16, 17]. The SiO_2 is a particulate material, and nano-sized particles (1–100 nm) are probably formed during its manufacture. It has been demonstrated in previous studies that SiO_2 NPs have a damaging effect on a range of organisms, resulting in reduced survival rates, diminished cellular viability, and modifications to lipid metabolism [18-20]. Furthermore, our previous research indicated a notable reduction in hemocyte counts and viability in *G. mellonella* larvae following exposure to elevated doses of SiO_2 NPs [21]. Nevertheless, the extent to which such exposures affect the nutritional quality of *G. mellonella* larvae remains largely uninvestigated. Therefore, this study aims to address the lack of research in this area by investigating the effects of varying concentrations of SiO_2 NPs on the chemical and biochemical parameters of *G. mellonella* larvae. In particular, the impact of the nanoparticles on the nutritional value of the larvae was assessed by changes in protein, lipid, carbohydrate, moisture, ash, and fatty acid composition. By connecting the effects of nanoparticle exposure to nutritional outcomes, this research contributes to the expanding field of knowledge regarding edible insects and their part in sustainable food systems.

2. General Methods

2.1. Insect

The larvae were reared in conditions of 25±5°C, 60±5% relative humidity and a photoperiod of 12:12 (light: dark). The rearing conditions, including temperature, humidity and ambient light, were rigorously monitored and maintained throughout the experimental period. Adult insects and newly hatched larvae were raised in glass jars and honeycomb was used for their nutrition. A spherical nanopowder of SiO_2 NPs with a diameter of 22 nm was employed in all experimental treatments (Nanokar, İstanbul, Türkiye).

2.2. Characterization of SiO_2 NPs

Scanning electron microscopy (SEM) and X-ray diffraction (XRD) were employed to confirm the morphological and structural properties of the SiO_2 NPs, thereby ensuring consistency and accuracy in the experimental treatments. Results of spherical and 22 nm-sized hydrophilic amorphous SiO_2 NPs were given in detail in a study that we have previously performed [21]. The XRD results of the SiO_2 NPs revealed the presence of an amorphous peak with an equivalent Bragg angle of $2\theta=22.16$. [21, 22].

2.3. Experimental diets

A series of multiple-dose experiments at elevated doses was conducted to ascertain the LD_{50} (lethal dose) of SiO_2 NPs. However, the doses of 500,

5000, 30000, and 60000 ppm of SiO_2 NPs were identified as the experimental doses for the study, as the mortality rates observed in larvae exposed to doses below 60000 ppm were within the range of 50-90% [23]. In the study, doses of 500, 5000, 30000, and 60000 ppm SiO_2 NPs were added to the insect diet mixture recommended by Bronskill [24]. The SiO_2 NPs were sonicated in a bath sonicator for 5 min before being transferred to the experimental diets. Only pure water was added to diets of the control larvae. Forty second instar larvae were transferred to the insect feeding diets. From these larvae, 14-16 days old last instar larvae were selected for the treatments. For each experimental group, 12 larvae, with 3 repetitions and 4 larvae in each repetition were selected so that their total weight would be equivalent to 2g [25, 26]. The moisture (mg), protein (%), lipid (%), carbohydrates (%), ash content (%) and fatty acid composition of the larvae was determined.

2.4. Moisture content analysis

The samples were subjected to a drying process at 65°C for approximately 8 h until a constant weight was attained. Subsequently, the moisture content of the larvae was calculated by subtracting the dry weight from the fresh weight [27].

2.5. Ash content analysis

The samples were weighted in porcelain crucible and heated at 550°C for 12 h. Samples reached a constant weight and light grey color after the heating. After the samples were cooled to room temperature, ash content was calculated from the weight difference [28].

2.6. Protein content analysis

The protein content of samples was determined by the Kejldahl method [29]. The samples were weighted into the digestion tubes and the catalyst (K_2SO_4 and $CuSO_4$) and H_2SO_4 were added to the tubes. The samples were digested until the mixture reached a green color. After digestion, samples were distillated with Na_2SO_4 solution into the H_3BO_3 solution. Finally, distillated samples were titrated by HCl and the nitrogen content was calculated. In order to determine the total protein amount, the nitrogen content determined was multiplied by a coefficient of 5.6 [30].

2.7. Fat content analysis

The fat content of the larvae was determined by the Soxhlet extraction method [28]. The sample was weighted into Soxhlet apparatus and petroleum ether was added as solvent. The sample was extracted for a total of 6 h. The fat content of the sample was calculated based on the weight difference before and after extraction.

2.8. Carbohydrates content analysis

The carbohydrate content of the larvae was determined by the anthrone method [31]. Dried samples were stirring with distilled water at 25°C for 1 h and then centrifuged to obtain extraction. Extracts were mixed with anthrone reagent and mixed for 1 min. Then, mixture were heated at 100°C for 30 min. The absorbance of samples were determined at 620 nm by UV-VIS spectrophotometer after the samples cooled to room temperature. The results were expressed as percentage of dry sample mass.

2.9. Fatty acid composition analysis

The cuticular free fatty acids were extracted by method described by [26]. The samples were extracted for a period of 5 min in 20 ml of petroleum ether, followed by a further 5 min in 20 ml of dichloromethane. The methylation procedure of lipids and GC condition was carried out in accordance with the methodology described by Ozer and Kilic [32]. Extracted lipid from the larvae was methylated with CH_3ONa solution in methanol and BF_3 solution in methanol and analyzed by Agilent 7820A gas chromatography (Agilent Technologies, USA). The identification of fatty acids in the samples was conducted through a comparison of the starting times of the fatty acid methyl esters standards. The results were expressed as a percentage of the total gas chromatography area.

2.10. Statistical analysis

The means were compared with one way ANOVA and the differences between the means

were significant with P<0.05. The p- and F-values from the one-way ANOVA testing are presented. Tukey's test for post hoc analysis was applied (SPSS 2010). Principal component analysis (PCA) was employed for the purpose of visualizing and interpreting the multivariate relationships between fatty acid composition and the experimental treatments. PCA was conducted on the fatty acid composition and the content of polyunsaturated (PUFA), monounsaturated (MUFA), and saturated (SFA) fatty acids using the Minitab software (Minitab 21.4.1, Minitab Inc., State College, PA, USA).

3. Results and Discussion

Table 1 provides the chemical composition of larvae under varying doses of SiO_2 NPs, highlighting significant changes in key nutritional components. According to the statistical results, when protein content for *G. mellonella* larvae fed with SiO_2 NPs were examined, a notable difference was found between the control group and doses of 5000 ppm and above (x^2=65.020, F= 459.572, df=4, P=0.00) (Table 1). Depending on the increasing SiO_2 NPs dose in the diet, the observed reduction in protein content suggests a potential disruption in protein synthesis or increased degradation, likely linked to oxidative stress induced by SiO_2 NPs (Table 1). A similar situation was observed in fat content, and increasing doses of SiO_2 NPs caused a decrease in the fat content of the larvae (x^2=61.708, F= 123.9, df=4, P=0.00).

The reduction in fat content may be indicative of an interference with lipid metabolism pathways, potentially through the inhibition of lipid synthesis enzymes or enhanced lipid oxidation. The carbohydrate content demonstrated a notable dose-dependent decline, which is likely associated with the increased metabolic demand for energy under conditions of oxidative stress (x^2=0.068, F= 8.570, df=4, P=0.018). In comparison to control group, a decrease in the moisture content in groups treated with 500 and 30000 ppm SiO_2 NPs (x^2=179.600, F= 0.643, df=4, P=0.004). Finally, all of the SiO_2 NPs doses increased the ash content in larvae at a statistically significant level (x^2=0.156, F= 38.427, df=4, P=0.010). The larval total fatty acid composition of *G. mellonella* according to experimental groups are given in Table 2. In this study, thirteen different fatty acids ranging from 6 to 22 carbon atoms were identified in all larvae (Table 2). According to the results of fatty acid composition analysis, larvae contained SFA (up to 60%), followed by MUFA (up to 38%), and PUFA (up to 1.5%) (Table 2).

Among the SFAs, palmitic acid (C16:0) was a major fatty acid (up to 46%). Compared with the control group, the palmitic acid significantly increased depending on the increasing SiO_2 NPs (47–55%, respectively) (x^2=25.881, F= 0.643, df=4 P=0.000). Another most abundant fatty acid in larva was oleic acid (C18:1) (up to 29%), and there was a decline in the this fatty acid in larvae exposed to 30000 and 60000 ppm SiO_2 NPs (down to 22%) (x^2=16.345, F= 593.15, df=4, P=0.000). Similarly, compared with the control group, at all doses of the SiO_2 NPs, caused a significant decrease in the content of capric acid (C10:0) (at 500, 5000, and 30000 ppm SiO_2 NPs doses) (x^2=16.345, F= 593.15, df=4, P=0.000), heneicosenoic acid (C21:1) (at all SiO_2 NPs doses (500-60000ppm)), (x^2=1.532, F= 38.758, df=4, P=0.001), behenic acid (C22:0) (at 500 and 30000 ppm SiO_2 NP doses) (F= 46.00, df=4, P=0.000). Conversely, some doses of the SiO_2 NPs resulted in a notable increment in the linoleic acid (C18:2) (at all SiO_2 NPs doses (500-60000ppm)) (x^2=0.059, F= 10.873, df=4, P=0.011) (Table 2). There were no significant increases or decreases in the other identified fatty acids (Table 2).

PCA was conducted to investigate the differences and similarities between the treatment groups, with the fatty acid composition and saturated and unsaturated properties of fatty acids considered (Figure 1).

PCA identified the effect of SiO_2 NPs on fatty acids more clearly. It was concluded that the experimental groups in which SiO_2 NP was not used or used at a dose of 500 ppm (control and Group 1) exhibited similarities in fatty acid profiles, particularly those of C18:1, C21:1, and C14:0 (Figure 1A).

Table 1. Effects of Silicon dioxide nanoparticles (SiO_2 NPs) on chemical parameters in *Galleria mellonella* larvae[x]

Groups	Protein (%)[y]	Fat (%)[y]	Carbohydrate (%)[y]	Water Content (mg)[y]	Ash content (%)[y]
Control	43.38±0.47 [ax]	52.35±0.40 [a]	2.03±0.08 [a]	101.0±6.0 [a]	2.30±0.05 [a]
500 ppm SiO_2 NP	42.55±0.10 [a]	50.97±0.70 [a]	1.74±0.04 [b]	77.0±2.0 [b]	2.67±0.10 [b]
5000 ppm SiO_2 NP	39.37±0.30 [b]	48.43±0.09 [b]	1.58±0.03 [c]	91.5±5.5 [ab]	2.68±0.03 [b]
30000 ppm SiO_2 NP	33.00±0.02 [c]	43.55±0.30 [c]	1.44±0.01 [cd]	82.0±7.1 [b]	2.54±0.07 [b]
60000 ppm SiO_2 NP	30.67±0.18 [d]	38.92±0.71 [d]	1.31±0.04 [d]	93.0±2.3 [ab]	2.78±0.03 [b]

[x]Values are mean ± standard error from triplicate groups.
[a, b, c] Values within a row with different superscripts differ significantly at P<0.0

Table 2. Larval total fatty acid composition of *Galleria mellonella* according to experimental groups[x]

Fatty Acids Methyl Esters (FAMEs, %)		Control	500 ppm SiO_2 NP	5000 ppm SiO_2 NP	30000 ppm SiO_2 NP	60000 ppm SiO_2 NP
C6:0[y]	Caproic acid	1.67±0.03 [a]	1.60±0.02 [a]	1.67±0.02 [a]	1.64±0.08 [a]	1.59±0.01 [a]
C8:0	Caprylic acid	1.10±0.01 [a]	1.09±0.02 [a]	1.11±0.02 [a]	1.12±0.04 [a]	1.11±0.03 [a]
C10:0	Capric acid	0.49±0.04 [a]	0.35±0.02 [b]	0.32±0.02 [b]	0.38±0.01 [b]	0.41±0.03 [ab]
C12:0	Lauric acid	0.91±0.02 [a]	0.86±0.04 [a]	0.92±0.01 [a]	0.88±0.09 [a]	0.93±0.05 [a]
C14:0	Myristic acid	3.85±0.04 [a]	3.84±0.05 [a]	3.75±0.13 [a]	3.81±0.02 [a]	3.75±0.11 [a]
C15:0	Pentadecylic acid	0.91±0.04 [a]	0.87±0.02 [a]	0.86±0.05 [a]	0.89±0.01 [a]	0.86±0.02 [a]
C16:0	Palmitic acid	46.42±0.07 [a]	47.31±0.15 [b]	48.27±0.13 [c]	51.85±0.33 [d]	55.05±0.07 [e]
C16:1	Palmitoleic acid	0.32±0.03 [a]	0.32±0.02 [a]	0.35±0.01 [a]	0.33±0.04 [a]	0.34±0.02 [a]
C18:0	Stearic acid	4.87±0.19 [a]	4.75±0.07 [a]	4.42±0.17 [a]	4.42±0.04 [a]	4.66±0.17 [a]
C18:1	Oleic acid	29.17±0.03 [a]	29.15±0.06 [a]	29.05±0.12 [a]	25.67±0.22 [b]	22.81±0.03 [c]
C18:2	Linoleic acid	1.56±0.07 [a]	1.76±0.08 [b]	1.76±0.02 [b]	1.91±0.03 [bc]	2.01±0.04 [c]
C21:1	Heneicosenoic acid	8.56±0.23 [a]	7.94±0.01 [b]	7.35±0.01 [c]	6.96±0.17 [d]	6.29±0.13 [e]
C22:0	Behenic acid	0.15±0.01 [a]	0.14±0.01 [b]	0.15±0.01 [a]	0.12±0.01 [c]	0.15±0.02 [a]
∑PUFA	Polyunsaturated fatty acids	1.56±0.07 [a]	1.76±0.08 [b]	1.76±0.02 [b]	1.91±0.03 [bc]	2.01±0.04 [c]
∑MUFA	Monounsaturated fatty acids	38.06±0.23 [a]	37.41±0.09 [ab]	36.75±0.11 [b]	32.96±0.36 [c]	29.45±0.18 [d]
∑SFA	Saturated fatty acids	60.38±0.30 [a]	60.83±0.17 [ab]	61.48±0.09 [b]	65.12±0.38 [c]	68.53±0.21 [d]

[x]Values are the average of three replicates.
[a, b, c] Values within a row with different superscripts differ significantly at P<0.05

These similarities explained the observed variance to a significant extent, while the other experimental groups demonstrated notable differences from these control groups. Conversely, it can be stated that in groups 3 and 4, which have the highest SiO_2 NP usage, C16:0 and C18:2 fatty acids are differentiated from other groups by exhibiting higher values. The changes in fatty acids also affected the ratios of SFA, MUFA and PUFA in total fatty acids. Figure 1B illustrates the significant differentiation between experimental groups based on their distinct fatty acid profiles, which serves to confirm the role of SiO_2 NPs in modifying the lipid composition. Consequently, groups 3 and 4 were separated from the other groups. Conversely, Group 2 exhibits partial similarities to the other groups but also displays distinctive characteristics with regard to specific fatty acids (e.g., C18:2).

Proteins consumed through diet are broken down in the gastrointestinal system of humans or animals by enzymes such as proteases and peptidases, and then converted into amino acids, dipeptides, or tripeptides, which are absorbed in the small intestine [11]. The harmful chemicals applied to insects also affect the structure and quantity of synthesized proteins. It is thought that the increased oxidative stress induced by SiO_2 NPs may potentially disrupt mitochondrial function, which could result in impaired protein synthesis and increased proteolytic activity. Specifically, the activities of synthesized enzymes are either increasing or decreasing [33, 34]. The chemical substance used in our study, SiO_2 NPs doses (at doses of 5000 ppm and above) significantly reduced the protein content (P<0.05) (Table 1).

As known, SiO_2 NPs has the potential to damage mitochondria and subsequently facilitate the increased degradation of proteins, nucleic acids and lipids through reactive oxygen species release (ROS) [35].

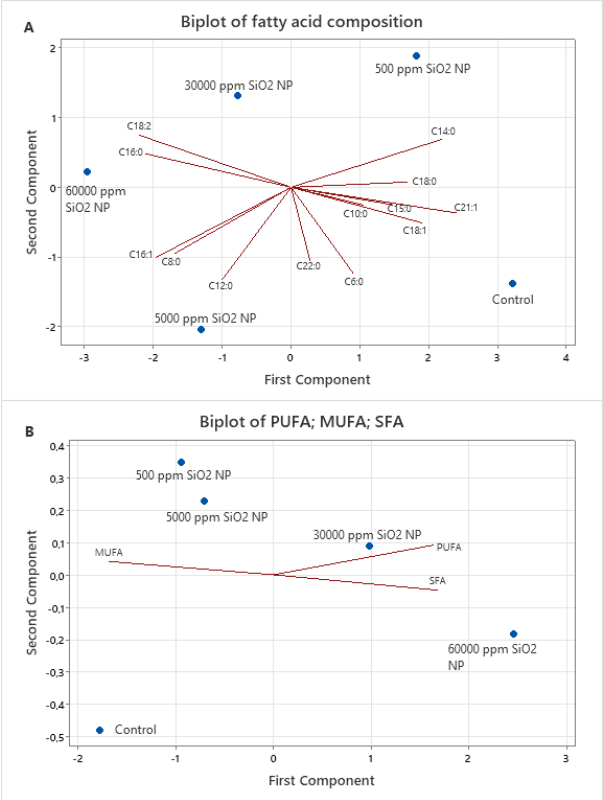

Figure 1. Loading Plot of principal component analysis on fatty acid composition (A), PUFA, MUFA and SFA content (B).

Therefore, exposure of the insect to SiO_2 NPs may have caused oxidative stress that negatively affected its chemical and biochemical parameters (Table 1). Korsloot, van Gestel [36] have noted that stress reactions in insects are known to be energy-demanding processes. It has been argued that energy-demanding stress responses, such as increased repair and detoxification activities, may have contributed to the depletion of protein, fat, and carbohydrate reserves. The organisms may divert energy to repair mechanisms, and pathogenic impacts may cause the depletion of energy stores [37]. Therefore, it is thought that the decrease in protein, fat and carbohydrate contents in *G. mellonella* larvae due to increasing SiO_2 NPs doses is related to NP-induced stress. (Table 1). In addition to all these results, NP-induced stress caused an important reduction in the body moisture content of *G. mellonella* at 500 and 30000 ppm SiO_2 NPs doses as a physiological response ($P<0.05$) (Table 1). It has been reported that loss of moisture content due to external factors may occur as a physiological response in insects [38]. Unlike the moisture content values, all of the SiO_2 NPs doses increased significantly the content of the ash content compared to the control group ($P<0.05$) (Table 1). The decreasing moisture content and increasing ash content have been reported by Markmanuel and Godwin [39] with similar to present study. The elevated ash content indicates the accumulation of mineral content, which may be attributed to disrupted metabolic pathways resulting from NP exposure [39].

The present study provides confirmation of results previously obtained, indicating that the most significant and prevalent fatty acids in *G. mellonella* are palmitic and oleic acids [40, 41] (Table 2). Additionally, larvae contained a significant amount of heneicosenoic acid. However, larvae's contained negligible levels of short-chain and very long-chain fatty acids (Table 2). It is thought that this may be related to feeding of larva's. Kazek, Kaczmarek [41] stated that the presence of short and long-chain fatty acids is related to the diet of the larvae. Furthermore, larvae fed with wax contain more short-chain and long-chain fatty acids.

The findings of studies conducted on *G. mellonella* larvae indicate that alterations in the fatty acid profile may occur as a consequence of oxidative stress, which may be the result of infection, exposure to certain ingredients or different feeding practices [41-44]. It seems probable that this is an adaptive response aimed at counteracting the harmful effects of reactive oxygen species [44]. For example, the changes in fatty acid composition has been evidenced in both LDPE-containing nutrition and *Conidiobolus coronatus* infection [44, 45]. It has been identified that polyunsaturated fatty acids can predispose larvae to oxidative damage, as they are susceptible to ROS attack and can cause to the formation of lipid hydroperoxides [42].

Nevertheless, alterations in fatty acid composition may also be affected by SiO_2 NPs the oxidative stress process within the organism. Indeed, our study demonstrated that the increase in exposure of SiO_2 NPs dose, a source of oxidative stress, resulted in an elevation in

polyunsaturated fatty acids while monounsaturated fatty acids exhibited a decline (Table 2).

Similarly, oxidative stress resulting from various infections has been shown to result in a reduction in MUFA, despite an increase in PUFA [46, 47]. Changes in the fatty acid composition of larvae after exposure to SiO_2 NPs can be attributed to a variety of underlying mechanisms. One of the most fundamental and relevant mechanisms may be oxidative stress caused by SiO_2 NPs. It is well known that NPs can produce ROS when interacting with biological systems [48]. The peroxidation of lipids induced by ROS results in the disruption of membrane integrity, which in turn leads to the degradation of unsaturated fatty acids and alterations in the fatty acid profile [49]. The most well-known consequence of oxidative stress is lipid peroxidation, which causes disruption of cellular membranes and changes in membrane fluidity and function [48].

Furthermore, the potential of SiO_2 to NPs affect lipid metabolism in larvae is also identified. NPs have the potential to inhibit the enzymatic activities involved in the synthesis and degradation of lipids. For example, SiO_2 NPs have the potential to inhibit or alter the activities of desaturase and elongate enzymes, which are essential for the synthesis of long-chain fatty acids. This may result in a reduction or increase in the levels of specific fatty acids, which could lead to alterations in the overall fatty acid profile [49]. Finally, it is hypothesized that SiO_2 NPs may influence the energy metabolism of larvae. NPs have been demonstrated to affect mitochondrial function, which is crucial for energy production and lipid metabolism. This may result in alterations to the synthesis of fatty acids. Hussain, Javorina [50] reported that NPs can disrupt mitochondrial activity, resulting in decreased ATP production and increased fatty acid oxidation as a compensatory mechanism.

4. Conclusion

In conclusion, the exposure of *G. mellonella* larvae to SiO_2 NPs resulted in significant alterations in their chemical parameters, particularly in fatty acid composition. The determined changes can be linked to oxidative stress, interference with lipid metabolism, inhibition of some enzyme activities and mitochondrial dysfunction. These findings highlight the importance of investigating the long-term impacts of nanoparticle exposure on the nutritional quality of edible insects, particularly in the context of their use as sustainable protein sources. The study raises significant questions regarding the safety and regulation of nanoparticles in food systems, emphasizing the requirement for further research and policy development.

Article Information Form

Funding
This study was supported by Nevşehir Hacı Bektaş Veli University Scientific Research Projects Unit (Project number HDP24F04).

Authors Contribution
Conceptualization, A.E. and C.O.Ö.; funding acquisition, A.E.; methodology, A.E. and C.O.Ö.; investigation, A.E. and C.O.Ö.; formal analysis, A.E. and C.O.Ö.; writing-original draft preparation, A.E. and C.O.Ö.; writing-review & editing, A.E. and C.O.Ö. All authors have read and agreed to the published version of the manuscript.

The Declaration of Conflict of Interest/ Common Interest
No conflict of interest has been declared by authors.

The Declaration of Ethics Committee Approval
This study does not require ethics committee permission or any special permission.

The Declaration of Research and Publication Ethics
Authors of the paper declare that they comply with the scientific, ethical and quotation rules of SAUJS in all processes of the paper and that they do not make any falsification on the data collected. In addition, they declare that Sakarya University Journal of Science and its editorial board have no responsibility for any ethical violations that may be encountered, and that this study has not been evaluated in any academic publication environment other than Sakarya University Journal of Science.

References

[1] J. Fanzo, A. L. Bellows, M. L. Spiker, A. L. Thorne-Lyman, M. W. Bloem, "The importance of food systems and the environment for nutrition," The American Journal of Clinical Nutrition, vol. 113, no. 1, pp. 7-16, 2021.

[2] M. Henchion, A. P. Moloney, J. Hyland, J. Zimmermann, S. McCarthy, "Review: Trends for meat, milk and egg consumption for the next decades and the role played by livestock systems in the global production of proteins," Animal, vol. 15, supplement 1, pp. 1-14, 2021.

[3] P. Kumar, N. Mehta, A. A. Abubakar, A. K. Verma, U. Kaka, N. Sharma, A. Q. Sazili, M. Pateiro, M. Kumar, J. M. Lorenzo, "Potential alternatives of animal proteins for sustainability in the food sector," Food Reviews International, vol. 38, no. 8, pp. 5703-5728, 2023.

[4] A. J. da Silva Lucas, L. M. de Oliveira, M. Da Rocha, C. Prentice, "Edible insects: An alternative of nutritional, functional and bioactive compounds," Food Chemistry, vol. 311, pp. 1-11, 2020.

[5] K. W. Lange, Y. Nakamura, "Edible insects as future food: Changes and challenges," Journal of Future Foods, 1- 1, pp. 38-46, 2021.

[6] İ. H. Tekiner, G. Darama, B. Özatila, H. Yetim, "Beslenme ve gıda teknolojisi yönünden yenilebilir böcekler," Academic Platform Journal of Halal Lifestyle, vol. 4, no. 1, pp. 18-29, 2022.

[7] M. Ryan, "Edible Insects: Future prospects for food and feed security," Library Journal, p. 32-32, 2014.

[8] Z. D. Ma, M. Mondor, F. M. Goycoolea, S. R. Ganji, A. J. Hernández-Alvarez, "Unlocking the potential of waxworm (*Galleria mellonella*) proteins: Extraction, fractionation, and protein quality assessment," Food Bioscience, Vol. 59, pp. 1-15, 2024.

[9] A. E. Ghaly, F. Alkoaik, "The yellow mealworm as a novel source of protein," American Journal of Agricultural and Biological Sciences, vol. 4, no. 4, 319-331, 2009.

[10] E. m. Teixeira, M. R. Carvalho, V. A. Neves, M. A. Silva, L. Arantes-Pereira, "Chemical characteristics and fractionation of proteins from *Moringa oleifera* Lam. leaves," Food Chemistry, vol. 147, pp. 51-4, 2014.

[11] M. H. Demirci, M., H. Yetim, "İnsan gıdası olarak böcek proteinleri tüketimi ve getirdiği sorunlar," Helal ve Etik Araştırmalar Dergisi, vol. 3, no. 2, pp. 11-22, 2021.

[12] M. A. Hussein, H. A. Salem, S. Hala, S. Mahmoud, "Effects of the nutrition of different diets and lipid content of the insect host larvae on the efficacy of indigenous entomopathogenic nematodes," Journal of Plant Protection Research, vol. 62, no. 3, pp. 265-271, 2022.

[13] M. F. Pereira, M. F., C. C. Rossi, "Overview of rearing and testing conditions and a guide for optimizing *Galleria mellonella* breeding and use in the laboratory for scientific purposes," APMIS, . vol. 128, no. 12, pp. 607-620, 2020.

[14] M. Younes, P. Aggett, F. Aguilar, R. Crebelli, B. Dusemund, M. Filipič, M. J. Frutos, P. Galtier, D. Gott, "EFSA panel on food additives nutrient sources added to food: Re-evaluation of silicon dioxide (E 551) as a food additive," EFSA Journal, vol. 16, no. 1, pp. 1-70, 2018.

[15] S. A. Khan, M. E. Johnson, M. S. Kalan, A. R. Montoro Bustos, S. A. Rabb, I. H. Strenge, K. E. Murphy, T. R. Croley, "Characterization of nanoparticles in silicon dioxide food additive," Food Additives & Contaminants: Part A, vol. 41, no. 1, pp. 9–21, 2024.

[16] C. Contado, "Nanomaterials in consumer products: A challenging analytical problem," Frontiners in Chemistry, vol. 3, no. 48, pp. 1-20, 2015.

[17] B. C. Palmer, S. Jatana, S. J. Phelan-Dickinson, L. A. DeLouise, "Amorphous silicon dioxide nanoparticles modulate immune responses in a model of allergic contact dermatitis," Scientific Reports, vol. 9, pp. 1-11, 2019.

[18] D. Altun Çolak, Ç. Ersöz, "Meyve Sineği larvalarında SiO_2 nanopartikülünün toksisite değerlendirmesi," Erzincan Üniversitesi Fen Bilimleri Enstitüsü Dergisi, vol. 11, no. 2, pp. 255-262, 2018.

[19] F. Abbasi, F., M. R. Samaei, H. Hashemi, A. Savardashtaki, A. Azhdarpoor, M. J. Fallahi, M. Jalili, S. Billet, "The toxicity of SiO_2 NPs on cell proliferation and cellular uptake of human lung fibroblastic cell line during the variation of calcination temperature and its modeling by artificial neural network," Journal of Environmental Health Science and Engineering, vol. 19, no. 11, 985-995, 2021.

[20] M. E. El-Naggar, N. R. Abdelsalam, M. M. G. Fouda, M. I. Mackled, M. A. M. Al-Jaddadi, H. M. Ali, M. H. Siddiqui, E. E. Kandil, "Soil Application of Nano Silica on Maize Yield and Its Insecticidal Activity Against Some Stored Insects After the Post-Harvest, "Nanomaterials, vol. 10, no. 4, pp. 1-19, 2020.

[21] A. Eskin, "Effects of silicon dioxide nanoparticles (SiO_2 NPs) on total hemocyte count and hemocyte viability of *Galleria mellonella,*" International Journal of Tropical Insect Science, vol. 42, no. 3., pp. 2617-2623, 2022.

[22] J. Sun, Z. Xu, W. Li, X. Shen, "Effect of nano-SiO_2 on the early hydration of alite-sulphoaluminate cement, " Nanomaterials, vol. 7, no. 5, pp. 1-15, 2017.

[23] A. Eskin, Z. U. Nurullahoglu, "Effects of zinc oxide nanoparticles (ZnO NPs) on the biology of *Galleria mellonella* L. (Lepidoptera: Pyralidae)," The Journal of Basic and Applied Zoology, vol. 83, no. 54, pp. 1-12, 2022.

[24] J. Bronskill, "A cage to simplify the rearing of the Greater Wax Moth, *Galleria mellonella* (Pyralidae)," Journal of the Lepidopterists' Society, vol. 15, 102-104, 1961.

[25] N. Ewald, A. Vidakovic, M. Langeland, A. Kiessling, S. Sampels, C. Lalander, "Fatty acid composition of black soldier fly larvae (*Hermetia illucens*)–Possibilities and limitations for modification through diet," Waste Management, vol. 102, pp. 40-47, 2020.

[26] A. K. Wrońska, M. I. Boguś, E. Włóka, M. Kazek, A. Kaczmarek, K. Zalewska, "Cuticular fatty acids of *Galleria mellonella* (Lepidoptera) inhibit fungal enzymatic activities of pathogenic *Conidiobolus coronatus,*" PLoS One, vol. 13, no. 3, pp. 1-16, 2018.

[27] H. O. Mohamed, A. Amro, "Impact of different diets' nutrition on the fitness and hemocytic responses of the Greater Wax Moth larvae, *Galleria mellonella* (Linnaeus) (Lepidoptera: Pyralidae)," The Journal of Basic and Applied Zoology, vol. 83, no. 10, pp. 1-11, 2022.

[28] AOAC, "Official methods of analysis of AOAC International″, 2005.

[29] P. L. Kirk, "Kjeldahl method for total nitrogen," Analytical Chemistry, vol. 22, no. 2, pp. 354-358, 1950.

[30] A. L. Rabie, J. D. Wells, L. K. Dent, "The nitrogen-content of pollen protein," Journal

of Apicultural Research, vol. 22, no. 2, pp. 119-123, 1983.

[31] J. Hedge, B. Hofreiter, R. Whistler, "Carbohydrate chemistry,"Acad Press, vol. 17, pp. 371-80, 1962.

[32] C. O. Ozer, B. Kilic, "Effect of conjugated linoleic acid enrichment on the quality characteristics of Turkish dry fermented sausage," Journal of Food and Science Technology, vol. 52, no. 4, pp. 2093-2102, 2015.

[33] F. Uçkan, A. Tüven, A. Er, E. Ergin, "Effects of gibberellic acid on biological parameters of the larval endoparasitoid *Apanteles galleriae* (Hymenoptera: Braconidae)," Annals of the Entomological Society of America, vol. 101, no. 3, pp. 593-597, 2008.

[34] R. Öztürk, "*Ferula halophila* ekstraktının *Galleria mellonella* L. (Lepidoptera: Pyralidae)'nın protein miktarı ve katalaz aktivitesi üzerine etkileri," Selçuk Üniversitesi Fen Fakültesi Fen Dergisi, vol. 47, no. 1, pp. 35-46, 2021.

[35] S. Abdallah, "A systematic literature review on the capability of SiO_2-np's exposure to exacerbate parkinson's (pd) pathology and the risk factors for biomedical applications in PD," University of Nebraska Medical Center, Nebraska pp. 1-29, 2022.

[36] A. Korsloot, C. A. van Gestel, N. M. Van Straalen, "Environmental stress and cellular response in arthropods," CRC press, pp. 197, Boca Raton, Florida, 2004.

[37] E. Ergin, H. Altuntas, F. Uçkan, "Effects of parasitization and envenomation by the endoparasitic wasp *Pimpla turionellae* L. (Hymenoptera: Ichneumonidae) on hemolymph protein profile of its host *Galleria mellonella* L. (Lepidoptera: Pyralidae)," Biological Diversity and Conservation, vol. 6, no. 1, pp. 62-70, 2013.

[38] Y. Kawarasaki, N. M. Teets, B. N. Philip, L. J. Potts, J. Gantz, D. L. Denlinger, R. E. Lee, "Characterization of drought-induced rapid cold-hardening in the Antarctic midge, *Belgica antarctica,*". Polar Biology, vol. 42, pp. 1147-1156, 2019.

[39] D. P. Markmanuel, J. Godwin, "Effects of culinary methods on the proximate composition of an edible insect (*Rhynchophorus phoenicis*) larvae obtained from Bayelsa State, Nigeria," European Journal of Agriculture and Food Sciences, vol. 2, no. 4, pp. 1-10, 2020.

[40] M. Gołębiowski, E. Maliński, M. I. Boguś, J. Kumirska, P. Stepnowski, "The cuticular fatty acids of *Calliphora vicina*, *Dendrolimus pini* and *Galleria mellonella* larvae and their role in resistance to fungal infection," Insect Biochemistry And Molecular Biology, vol. 38, no. 6, pp. 619-627, 2008.

[41] M. Kazek, A. Kaczmarek, A. K. Wronska, M. I. Bogus, "Diet influences the bacterial and free fatty acid profiles of the cuticle of *Galleria mellonella* larvae," PLoS One, vol. 14, no. 2, pp. 1-15, 2019.

[42] E. Büyükgüzel, Y. Kalender, "Exposure to streptomycin alters oxidative and antioxidative response in larval midgut tissues of *Galleria mellonella,*" Pesticide Biochemistry and Physiology, vol. 94, no. 2-3, pp. 112-118, 2009.

[43] E. Büyükgüzel, K. Büyükgüzel, "Oxidative impact of dietary Triclabendazole in *Galleria mellonella,*" Kafkas Universitesi Veterinerlik Fakültesi Dergisi, vol. 27, no. 3, pp. 301-306, 2021.

[44] M. Kazek, A. Kaczmarek, A. K. Wronska, M. I. Bogus, "*Conidiobolus coronatus* induces oxidative stress and autophagy response in *Galleria mellonella* larvae," PLoS One. vol. 15, no. 2, pp. 1-19, 2020.

[45] B. J. Cassone, H. C. Grove, N. Kurchaba, P. Geronimo, C. M. R. LeMoine, "Fat on

plastic: Metabolic consequences of an LDPE diet in the fat body of the Greater Wax Moth larvae (*Galleria mellonella*)," Journal of Hazardous Materials, vol. 425, pp. 1-8, 2022.

[46] I. Z. Boctor, H. S. Salama, "Effect of *Bacillus thuringiensis* on the lipid-content and composition of *Spodoptera-littoralis* larvae," Journal of Invertebrate Pathology, vol. 41, no. 3, pp. 381-384, 1983.

[47] I. M. Dubovskiy, V. V. Martemyanov, Y. L. Vorontsova, M. J. Rantala, E. V. Gryzanova, V. V. Glupov, "Effect of bacterial infection on antioxidant activity and lipid peroxidation in the midgut of *Galleria mellonella* L. larvae (Lepidoptera, Pyralidae)," Comparative Biochemistry and Physiology Part C: Toxicology & Pharmacology, vol. 148, vol. 1, 1-5, 2008.

[48] A. A. Shvedova, V. Castranova, E. R. Kisin, D. Schwegler-Berry, A. R. Murray, V. Z. Gandelsman, A. Maynard, P. Baron, "Exposure to carbon nanotube material: assessment of nanotube cytotoxicity using human keratinocyte cells," Journal of Toxicology and Environmental Health Part A, vol. 66, no. 20, 1909-1926, 2003.

[49] M. Parra-Robert, E. Casals, N. Massana, M. L. Zeng, M. Perramón, G. Fernández-Varo, M. Morales-Ruiz, V. Puntes, W. Jiménez, G. Casals, "Beyond the scavenging of reactive oxygen species (ROS): direct effect of cerium oxide nanoparticles in reducing fatty acids content in an in vitro model of *Hepatocellular steatosis*," Biomolecules, vol. 9, no. 9, pp. 1-16, 2019.

[50] S. M. Hussain, A. K. Javorina, A. M. Schrand, H. M. Duhart, S. F. Ali, J. J. Schlager, "The interaction of manganese nanoparticles with PC-12 cells induces dopamine depletion," Toxicological Sciences, vol. 92, no. 2, pp. 456-63, 2006.

Sakarya Üniversitesi Fen Bilimleri Dergisi
Sakarya University Journal of Science

e-ISSN : 2147-835X
Publisher : Sakarya University

Vol. 29, No. 2, 191-199, 2025
DOI: https://doi.org/10.16984/saufenbilder.1599129

Research Article

Effect of Chemical Composition and Annealing Parameters for Advanced Packaging Steel Applications

Ramazan Uzun*, Ümran Başkaya, Yasemin Kılıç

Eregli Iron and Steel Works Co., R&D Center, Kdz. Eregli, Zonguldak, Türkiye, ruzun@erdemir.com.tr, uerten@erdemir.com.tr, ykilic@erdemir.com.tr
*Corresponding Author

ARTICLE INFO

Keywords:
Packaging steel
Tinplate
Heat treatment
Characterization
Multiphase

Article History:
Received: 10.12.2024
Revised: 05.03.2025
Accepted: 12.03.2025
Online Available: 15.04.2025

ABSTRACT

Packaging steels are widely used across a broad range of industries, from food and beverage to chemical products, for the protection, transportation and storage of goods. In this study, the effects of chemical composition and annealing parameters on the phase transformation behavior, microstructure, and mechanical properties of packaging steels were investigated. Two steel samples, Steel A and Steel B, with different chemical compositions (designed according to ASTM A623-22 standard limitations), were prepared using a vacuum induction melting (VIM) furnace. Within the scope of simulation studies, hot rolling, cold rolling, and annealing process simulators were utilized. Before the annealing simulations, the Gleeble 3500 thermal simulation device and JMatPro software were used to determine the process conditions. A light optical microscope (LOM) and a scanning electron microscope (SEM) were used for microstructural characterization studies. Mechanical properties were characterized with tensile tests. Steel A and Steel B samples with different alloying elements and cooling rates were compared to evaluate their suitability for advanced packaging applications. The results of this analysis show that the addition of Nb and Mn to Steel B enhances bainite formation, refines grain size, and improves mechanical properties compared to Steel A.

1. Introduction

Traditional steels often struggle to balance strength and ductility; as strength increases, ductility typically decreases, making it difficult to meet safety and performance standards [1, 2]. Advanced high-strength steels (AHSS) with multiphase microstructures, including ferrite, bainite, martensite, and retained austenite, are increasingly used in automotive applications [3-7]. These steels are favored over traditional high-strength low-alloy (HSLA) steels because of their exceptional strength-to-ductility ratio, which merges high strength, excellent ductility, continuous yielding and high initial work hardening rates [8, 9]. The packaging sector has seen significant advancements in steel grades over recent decades, focusing on both higher strength materials and the need for highly formable steels suitable for complex deep drawing applications [10]. A specific example of such applications is the forming of valve cups for aerosol tops, which requires a high level of deformation, thus placing substantial demands on the materials used [11]. Packaging steels are preferred for their compatibility with human health, non-toxicity, excellent formability, weldability, and resistance to corrosion [12].

Tinplate is a versatile material primarily used in the packaging industry, particularly for food and beverage containers packaging steel finds use across a wide range of applications [13, 14]. These include diverse types of containers for food, personal hygiene products, household and automotive care items, industrial products, and paints. Additionally, it is utilized in the creation of gifts or promotional products, as well as

Cite as: R. Uzun, Ü. Başkaya, Y. Kılıç (2025). Effect of Chemical Composition and Annealing Parameters for Advanced Packaging Steel Applications, *Sakarya University Journal of Science*, 29(2), 191-199. https://doi.org/10.16984/saufenbilder.1599129

closures and aerosols [15, 16]. Tinplate materials are widely used in various industries due to their excellent properties such as corrosion resistance, high strength, and formability [17, 18].

Conventional tinplate materials primarily consist of a ferritic phase. Ferrite is characterized by its low carbon content, providing ductility and softness to the steel. This microstructure possesses high formability and low strength properties, enhancing the workability of tinplate materials and making them suitable for various packaging applications [19, 20]. Multiphase steels refer to materials that have a combination of different phases, such as ferrite, bainite, martensite and retained austenite. This combination enhances the mechanical properties of the tinplate, providing a balance of strength and ductility, which is beneficial for various packaging applications [21, 22]. In multiphase steels, high levels of alloying elements such as Mn, Si and Cr are required to achieve the desired microstructural and mechanical properties [23, 24]. However, for packaging steels that come into contact with food, the ASTM A623-22 standard imposes restrictions on the chemical composition of these elements [25]. Therefore, it is necessary to design and develop new concept packaging steels that go beyond the conventional approaches to multiphase steel production. This innovative approach aims to meet both the stringent chemical composition requirements for food contact and the mechanical performance demands of advanced packaging applications.

Recent literature reviews indicate a lack of comprehensive information on multiphase packaging steel. This is a significant gap considering the increasing demands of the packaging industry, which expects materials to maintain high strength and excellent formability even as thickness reductions become more stringent. Achieving these properties necessitates the presence of phases other than ferrite in the final microstructure. In traditional thin packaging steel production, a double cold reduction process is employed after annealing [26, 27]. This process not only reduces the material's thickness but also enhances hardness and strength, albeit at the expense of elongation percentage [14, 17, 18]. The desired mechanical properties and formability characteristics could potentially be achieved through a multiphase microstructure, thereby eliminating the need for a second cold reduction process. This approach would allow for direct utilization of the material post-annealing, meeting industry requirements for high performance without additional processing steps.

In the present work, the effects of chemical composition and annealing parameters on the phase transformation behavior, microstructure and mechanical properties of multiphase packaging steels were investigated.

2. Experimental Study

A schematic diagram illustrating the steps of the experimental procedure is shown in Figure 1.

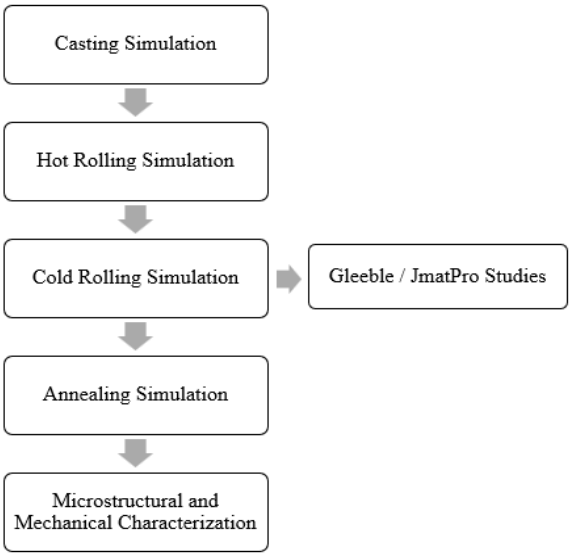

Figure 1. Schematic diagram of experimental process

2.1. Material

In the experimental studies, cold-rolled steel has been used. The chemical compositions of the materials used in the experimental studies are given in Table 1. The percentage values of the elements used in Table 1 have been designed considering the limit values specified in the ASTM A623-22 standard.

Table 1. Chemical composition of samples (wt.%)

Elements	Steel A	Steel B
C	0.110	0.110
Mn	0.350	0.530
Si	0.015	0.015
P	0.011	0.012
Cr	0.060	0.060
Nb	-	0.017

2.2. Simulation tests

Two different chemical compositions were used to produce ingots with dimensions of 500×150×225 mm in a vacuum induction melting (VIM) furnace. VIM furnace process is a technique used to melt metals under controlled vacuum conditions, typically for producing high-quality alloys. The process takes place under a vacuum environment to minimize contamination from gases such as oxygen or nitrogen, which could negatively affect the quality of the molten metal. This method is particularly useful for producing high-purity metals and alloys, as it reduces the presence of impurities that can occur in more conventional melting methods. The casting of materials with the compositions of Steel A and Steel B was completed, followed by hot rolling processes. During the hot rolling process, the finishing temperature was set at 900°C and the coiling temperature was applied at 550°C. In the cold rolling simulator, a reduction of 80% was applied to the samples. The rolled samples were subjected to annealing simulations to achieve the desired mechanical properties and to develop a multiphase microstructure. Prior to the annealing process, transformation temperatures can be predicted through physical simulations and computational software.

The production of multiphase steel involves determining the ferrite-austenite phase transition temperatures (A1 and A3), heating the material to the specified process temperature within these critical temperature ranges and maintaining this temperature to achieve the two-phase region. The material is then quenched to room temperature in order to achieve the desired microstructural features [28-29].
Computer simulations of intercritical continuous cooling transformation (CCT) diagrams, which are calculated based on chemical composition, have been utilized as a strategy to develop new chemistries for producing multiphase steels [30, 31]. The JmatPro software was performed to predict phase transformations.

Determining the transformation temperatures, Continuous Cooling Transformation (CCT) tests were conducted using a Gleeble 3500 thermal simulation device. The test involved heating solid flat specimens (Figure 2), 17.5 cm in length and 5 cm in width, to 920°C at a heating rate of 1°C/s. The specimens were held at this temperature for 30 seconds before being cooled to room temperature. It was cooled from this temperature to room temperature at a cooling rate of 1°C/s.

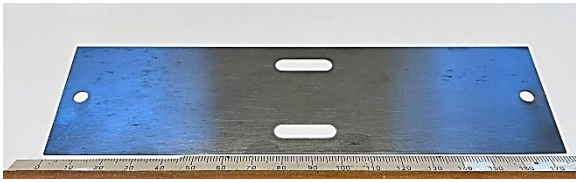

Figure 2. The sample of Gleeble 3500 thermal simulation device

2.3. Microstructural and mechanical characterization

Samples for microstructural analysis were cut along the transverse direction (TD). These sectioned specimens hot-mounted, grounded and polished in sequence. After polishing, the samples were etched with 2% nital and picral solutions for characterization. Samples were characterized using a light optical microscope (Nikon Eclipse MA200) and a scanning electron microscope (SEM, Zeiss EVO10).

Tensile tests were performed using a Zwick Z250 testing machine. The tests were conducted in accordance with the ISO 6892-1 standard [32].

3. Results and Discussion

3.1. Evaluation of simulation tests

Before annealing operation, dilatometric analyzes were carried out on the Gleeble Thermal Simulation device to determine the Ac_1 and Ac_3 transformation temperatures of the Steel A composition. The dilatation curves featured two key points corresponding to the intercritical temperatures. These points, marked by the first and second peaks on the dilatation curves, represent the Ac_1 and Ac_3 temperatures,

respectively. The CCT diagrams created and calculated with the usage of JMatPro software were used to examine the phase transformation and transition temperatures. It has been determined that the Ac_1 (725°C) and Ac_3 (870°C) temperatures obtained from CCT tests conducted on the Gleeble device are compatible with the temperatures predicted using JmatPro. The temperature values set on the Gleeble device were consistent with the measured values. The dilatometric curve of Steel A is given in Figure 3 and CCT diagram of Steel A is shown in Figure 4. According to the CCT diagram, the possible phases in the Steel A sample are ferrite and pearlite, with no additional phase transformations such as bainite and/or martensite observed as the cooling rate increases.

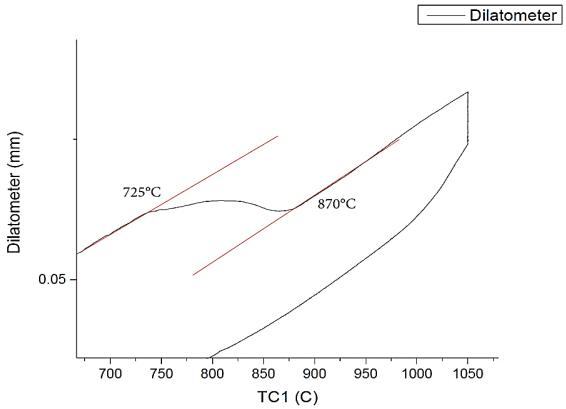

Figure 3. Gleeble dilatometry curve for Steel A

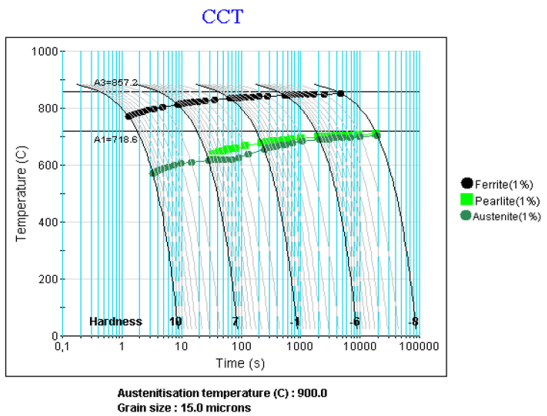

Figure 4. Continuous cooling transformation diagram for Steel A

The CCT diagram calculated for the composition of Steel B using JMatPro is presented in Figure 5. When comparing the CCT diagrams of Steel A and Steel B, it is observed that the Ac_1 and Ac_3 temperature values are close. The expected phase structures in the microstructure vary depending on the cooling rates applied in the CCT diagrams. In terms of microstructure, it is predicted that bainite and ferrite may form depending on the applied cooling rate.

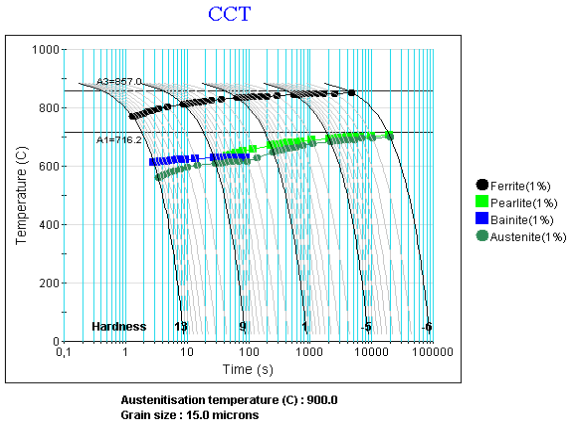

Figure 5. Continuous cooling transformation diagram for Steel B

Generally, achieving multiphase steel requires a high alloy content. However, as previously mentioned, due to the alloying limitations specified in the ASTM A623-22 standard for packaging steels, alloying can not be utilized. Therefore, process parameters were optimized to achieve the desired final properties. For cold-rolled steels with low alloy content in their chemical composition, it is necessary to apply high cooling rates during the annealing process. In the annealing process, a temperature of 810°C for 100 seconds within the A1 and A3 temperature range, was applied. Trials were performed at different cooling rates (30°C/s and 150°C/s).

3.2. Characterization of microstructure and mechanical properties

Niobium increases material strength with solid solution, grain refinement and precipitation hardening [33]. Nb is precipitated in the microstructure and delays recrystallization and forms an effective barrier to grain growth. Grain refinement effect also contributes positively to material strength and toughness [33, 34]. Microstructure images of samples etched with nital solution are given in Figure 6. Grain size of the Steel B was finer than the Steel A sample. It has been observed that niobium has a grain refining effect.

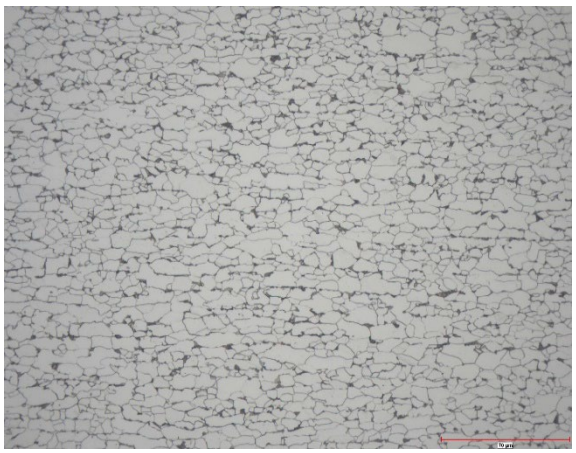

(a) Grain size 9.00 µm

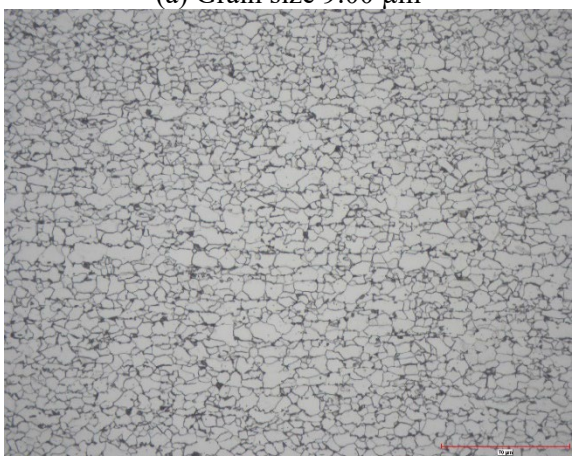

(b) Grain size 6.00 µm

Figure 6. Optical microscope micrographs of nital etched Steel A (a) and Steel B (b) samples

In the micrographs etched with nital, it was observed that the microstructure consisted of a two-phase structure. The light-toned regions represent the ferrite phase while the dark black areas are likely indicative of pearlite or bainite. The secondary phase content has been calculated using Clemex software. According to the calculation, the Steel A contains 8% secondary phase while the Steel B contains 9% secondary phase. However, this calculation does not differentiate between bainite and pearlite. In order to determine the second phase, picral etched samples were characterized by using SEM.

In the Steel A, the microstructure consists of ferrite and pearlite (Figure 7). This situation is also consistent with the CCT data in the simulation studies. Since the Steel A sample had a lean analysis, the experimental studies were continued with the Steel B sample in order to obtain the targeted microstructure and mechanical properties.

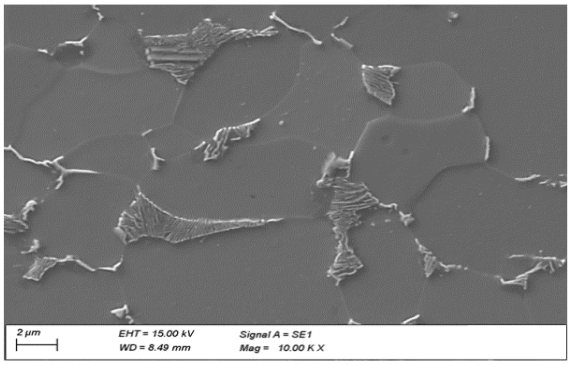

Figure 7. SEM images of steel A sample annealed at low cooling rate

In order to support the bainite transformation and strength increase, the Mn alloy element was increased and the Nb alloy element was added to the Steel B sample. In addition to alloy design within standard limits, cooling rates in the process were also revised. With the increasing cooling rate, bainite formation occurred and the microstructure consists of ferrite and bainite (Figure 8 and Figure 9).

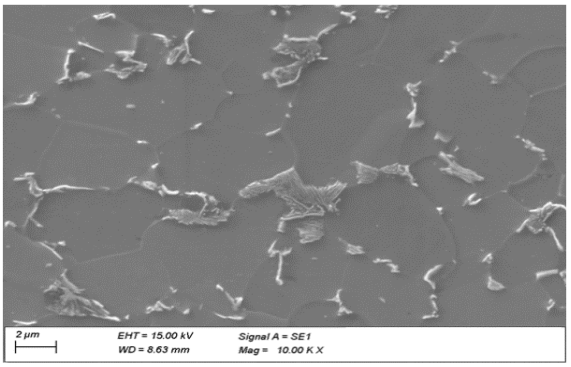

Figure 8. SEM images of Steel B sample annealed at low cooling rate

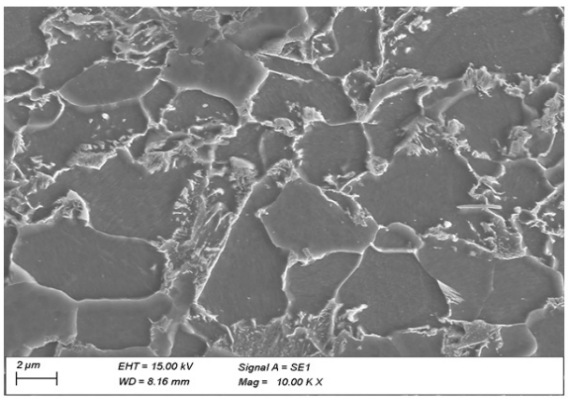

Figure 9. SEM images of Steel B sample annealed at high cooling rate

The mechanical test results observing the effects of process and alloy design for Steel A and Steel B samples are presented in Table 2. The mechanical tests were performed two times.

When simulations performed at low cooling rates are compared, it is determined that the mechanical properties of the Steel B sample are better. Although both steels contain ferrite and pearlite phases, this difference in mechanical properties can be explained by variations in grain size (Steel A: 9 µm / Steel B: 6 µm) and alloy composition. Different mechanisms are used to enhance the strength of steels. These include solid solution strengthening, precipitation hardening, grain size refinement, phase transformation and work hardening [35-37].

As the grain size decreases, the strength and toughness of the steel improve. The relationship between grain size and strength is explained by the Hall-Petch equation [35]. The precipitates present in the microstructure prevent grain boundary coarsening and contribute to achieving a fine-grained structure [35]. As the grain size decreases, grain boundaries act as barriers to dislocation motion, thereby enhancing strength. In this study, the higher strength observed in the Steel B sample compared to Steel A is attributed to the contributions of the Nb alloying element to fine grain size and precipitation strengthening, as well as the Mn alloying element to solid solution strengthening. In addition to annealing simulation studies performed at low cooling rates, the Steel B sample was carried out to both low and high cooling rates.

The microstructure of the simulation sample subjected to a low cooling rate consisted of ferrite and pearlite whereas the sample subjected to a high cooling rate exhibited the formation of ferrite and bainite (Figure 7, Figure 8 and Figure 9). In the Steel B sample, the increase in cooling rate promoted bainite formation, which positively contributed to the improvement of tensile strength.

Table 2. Mechanical values of samples

Mechanical Values	Steel A	Steel B	
	LCR	LCR	HCR
Yield Strength, MPa	351±6	370± 5	347±5
Tensile Strength, MPa	402±7	430± 7	502±6
% Elongation	21 ±1	21± 1	23± 1

LCR: low cooling rate (30°C/s)
HCR: high cooling rate (150°C/s)

3. Conclusion

This study investigated the effects of chemical composition and annealing parameters on the phase transformation, microstructure, and mechanical properties of multiphase packaging steels. The results are summarized below.

- The alloying values were used in the production of conventional multiphase steels can not be applied for packaging steel due to the alloying elements limit specified in the ASTM A623-22 standard. In the production of standard high strength packaging steel, the double reduction process enables an increase in strength. If the production of multiphase packaging steel becomes feasible, the double reduction process may not be necessary. Within this scope, a new alloy and process design has been developed.

- Mn contributed significantly to solid solution strengthening while Nb promoted grain refinement and precipitation strengthening. These modifications improved the tensile strength of Steel B compared to Steel A.

- High cooling rates facilitated the formation of bainite which was directly affected to tensile strength in Steel B. Conversely, lower cooling rates resulted in a microstructure dominated by ferrite and pearlite.

Article Information Form

Acknowledgments
Authors would like to thank Eregli Iron and Steel Works Co. for their support in experimental studies.

Funding
Authors have no received any financial support for the research, authorship or publication of this study.

Authors Contribution
Authors contributed equally to the study.

The Declaration of Conflict of Interest/ Common Interest

No conflict of interest or common interest has been declared by authors.

The Declaration of Ethics Committee Approval

This study does not require ethics committee permission or any special permission.

The Declaration of Research and Publication Ethics

Authors of the paper declare that they comply with the scientific, ethical and quotation rules of SAUJS in all processes of the paper and that they do not make any falsification on the data collected. In addition, they declare that Sakarya University Journal of Science and its editorial board have no responsibility for any ethical violations that may be encountered, and that this study has not been evaluated in any academic publication environment other than Sakarya University Journal of Science.

References

[1] E. Gutiérrez-Castañeda, C. Galicia-Ruiz, L. Hernández-Hernández, A. Torres-Castillo, D. F. De Lange, A. Salinas-Rodríguez, "Development of Low-Alloyed Low-Carbon Multiphase Steels under Conditions Similar to Those Used in Continuous Annealing and Galvanizing Lines", Metals, vol. 12, no. 8, pp. 1818, 2022.

[2] S. Keeler, M. Kimchi, P. J. Mooney, "Advanced High-Strength Steels Application Guidelines", World Auto Steel, version 6.0, 2017.

[3] S. Kılıç, F. Öztürk, "Recent trends of application of advanced high-strength steels in automotive industry to enhance sustainability", The 16th International Conference on Machine Design and Production, İzmir, Türkiye, 2014.

[4] R. Kuziak, R. Kawalla, S. Waengler, "Advanced High Strength Steels for Automotive Industry", Archives of Civil and Mechanical Engineering, vol. 8, no. 2, pp. 103–117, 2008.

[5] S. C. Ikpeseni, "Review of the Applications, Properties and Processing Parameters of Dual Phase Steels", Journal of Science and Technology Research, vol. 3, no. 2, pp. 125–139, 2021.

[6] ASM International, "Carbon and low-alloyed steels", ASM Handbook, Volume 1: Properties and Selection: Irons, Steels, and High-Performance Alloys, ASM International, 2005, pp. 697–707

[7] H. Matsuda, T. Kobayashi, Y. Fujimoto, "Cold-Rolled and Galvannealed (GA) Ultra-High Strength Steel Sheets for Automobile Structural Parts", JFE Technical Report, vol. 24, pp. 20–27, 2019.

[8] W. L. Samek, E. De Moor, J. Penning, J. G. Speer, B. C. De Cooman, "Static Strain Aging of Microstructural Constituents in Transformations-Induced-Plasticity Steel", Metallurgical and Materials Transactions A, vol. 39, no. 10, pp. 2542–54, 2008.

[9] S. H. Han, S. H. Choi, J. K. Choi, H. G. Seong, I. B. Kim, "Effect of Hot-Rolling Processing on Texture and r-Value of Annealed Dual-Phase Steels", Materials Science and Engineering A, vol. 527, pp. 1686–1694, 2010.

[10] D. K. Leu, "Prediction of the Limiting Drawing Ratio and the Maximum Drawing Load in Cup Drawing", International Journal of Machine Tools and Manufacture, vol. 37, no. 2, pp. 201–213, 1997.

[11] D. F. Knieps, M. Köhl, M. Merklein, "Drawing Capability of High Formable Packaging Steel: Comparison of Limiting Drawing Ratio and Forming Limit Curve", Key Engineering Materials, vol. 907, pp. 71–78, 2022.

[12] B. V. Salas, M. S. Wiener, J. M. Bastidas, J. R. S. Martínez, G. L. Badilla, "Use of Steel in Food Packaging", Reference Module in Food Science, 2016.

[13] Z. Berk, "Food packaging", Food Process Engineering and Technology, 3rd ed., Elsevier, 2018, pp. 625–641.

[14] G. K. Deshwal, N. R. Panjagari, "Review on Metal Packaging: Materials, Forms, Food Applications", Journal of Food Science and Technology, vol. 57, pp. 2377–2392, 2020.

[15] ASM International, "Surface engineering", ASM Handbook, Volume 5: Surface Engineering, ASM International, 1994.

[16] M. Słowik, P. Cepa, K. Czapla, P. Zabinski, "Steel Packaging Production Process and a Review of New Trends", Archives of Metallurgy and Materials, vol. 66, pp. 135–143, 2020.

[17] ITRA Tinplate Panel, Guide to Tinplate. UK, 2000, pp. 14–41.

[18] S. Pandey, K. K. Mishra, P. Ghosh, A. K. Singh, S. K. Jha, "Characterization of Tin-Plated Steel", Frontiers in Materials, vol. 10, pp. 1113438, 2023.

[19] J. Majerníková, E. Spišák, "The Comparison of Properties of Tinplates during Uniaxial and Biaxial Stress", International Journal of Engineering Science, vol. 5, no. 11, pp. 47–52, 2016.

[20] J. R. Davis, Ed., Metallurgy and Material Science. ASM International, 1998.

[21] D. Jorge-Badiola, "Advanced Multiphase Steels", Metals, vol. 13, pp. 1871, 2023.

[22] J. Bouquerel, K. Verbeken, B. C. De Cooman, "Microstructure Based Model for the Static Mechanical Behaviour of Multiphase Steels", Acta Materialia, vol. 54, pp. 1445–56, 2006.

[23] A. Gołaszewski, J. Szawłowski, W. Świątnicki, "Multiphase Steel Microstructure and Properties Optimisation through a New Heat Treatment Process", Materials Science and Technology, vol. 37, no. 1, pp. 1–7, 2021.

[24] A. Grajcar, W. Kwaśny, "Microstructural Study on Retained Austenite in Advanced High-Strength Multiphase 3Mn-1.5Al and 5Mn-1.5Al Steels", Journal of Achievements in Materials and Manufacturing Engineering, vol. 55, pp. 168–177, 2012.

[25] ASTM A623-22, Standard Specification for Tin Mill Products, General Requirements, 2022.

[26] X. F. Zheng, L. H. Liao, Y. L. Kang, W. Liu, Q. Q. Qiu, "The Effect of Chemical Composition and Processing Technology on the Microstructure, Texture, and Earing Behavior of DR Tinplate", Journal of Materials Engineering and Performance, vol. 28, pp. 485–497, 2019.

[27] B. P. Tian, L. H. Liao, G. Zhu, Y. Kang, "Effect of Secondary Cold Reduction Rates on Microstructure, Texture, and Earing Behavior of Double Reduction Tinplate", Materials, vol. 14, no. 14, pp. 2335, 2021.

[28] C. C. Tasan, M. Diehl, D. Yan, M. Bechtold, F. Roters, L. Schemmann, D. Raabe, "An Overview of Dual-Phase Steels: Advances in Microstructure-Oriented Processing and Micromechanically Guided Design", Annual Review of Materials Research, vol. 45, pp. 391–431, 2015.

[29] M. Maleki, H. Mirzadeh, M. Zamani, "Effect of Intercritical Annealing on Mechanical Properties and Work-Hardening Response of High Formability Dual Phase Steel", Steel Research International, vol. 89, no. 4, pp. 1700412, 2018.

[30] J. Ayres, D. Penney, P. Evans, “Effect of Intercritical Annealing on the Mechanical Properties of Dual-Phase Steel”, Ironmaking & Steelmaking, vol. 49, no. 6, pp. 821–827, 2022.

[31] A. Contreras, A. López, E. J. Gutiérrez, “An Approach for the Design of Multiphase Advanced High-Strength Steels Based on the Behavior of CCT Diagrams Simulated from the Intercritical Temperature Range”, Materials Science and Engineering A, vol. 772, pp. 138708, 2020.

[32] ISO 6892-1, Metallic materials - Tensile testing, Part 1: Method of test at room temperature.

[33] A. G. Kalashami, A. Kermanpur, Y. Najafizadeh, A. Mazaheri, “Development of a high strength and ductile Nb-bearing dual phase steel by cold-rolling and intercritical annealing of the ferrite-martensite microstructures”, Materials Science and Engineering A, vol. 658, pp. 355-366, 2015.

[34] W. Bleck, A. Frehn, J. Ohlert, “Niobium in Dual Phase and TRIP Steels”, Department of Ferrous Metallurgy, Aachen Univ. Technol., Aachen, Germany, 2016.

[35] J. W. Morris Jr., “The influence of grain size on the mechanical properties of steel”, Lawrence Berkeley National Laboratory, 2001.

[36] A. Kostryzhev, et al., “Comparative effect of Mo and Cr on microstructure and mechanical properties in NbV-microalloyed bainitic steels”, Metals, vol. 8, p. 134, 2018.

[37] G. Krauss, “Strengthening mechanisms in steels”, Encyclopedia of Materials: Science and Technology, 2nd ed., K. H. Jürgen Buschow, Oxford: Elsevier, 2001, pp. 8870–8881.

Sakarya Üniversitesi Fen Bilimleri Dergisi
Sakarya University Journal of Science

e-ISSN : 2147-835X
Publisher : Sakarya University

Vol. 29, No. 2, 200-207, 2025
DOI: https://doi.org/10.16984/saufenbilder.1530460

Research Article

A Novel Subclass of Harmonic Functions: Coefficient Bounds, Distortion Bounds, and Closure Properties

Serkan Çakmak

University of Istanbul Gelisim University, Faculty Economics, Administrative and Social Science, Department of Management Information Systems, İstanbul, Türkiye, secakmak@gelisim.edu.tr, ror.org/0188hvh39

ARTICLE INFO

Keywords:
Harmonic functions
Convolution
Coefficient bounds
Distortion bounds
Closure properties

Article History:
Received: 08.08.2024
Revised: 14.03.2025
Accepted: 18.03.2025
Online Available: 15.04.2025

ABSTRACT

In this paper, we introduce a new subclass of harmonic functions that significantly improves our understanding of these functions in geometric function theory. We provide a comprehensive analysis of this subclass by deriving several important properties, including coefficient bounds and decay bounds, which are necessary to evaluate the behavior and limitations of functions in this class. Additionally, we establish sufficient coefficient conditions for harmonic functions to belong to this class. Moreover, we rigorously show that this subclass is closed under both convex combinations and convolutions, meaning that any convex combination or convolution of functions in this class will also belong to the class. These results provide valuable insights into the stability and applicability of the subclass and provide a solid framework for further theoretical explorations and practical applications in complex analysis.

1. Introduction

In the study of harmonic functions, any function $\mathfrak{f}$ within the class SH^0 can be expressed as $\mathfrak{f} = \mathfrak{u} + \overline{\mathfrak{v}}$, where

$$\mathfrak{u}(z) = z + \sum_{s=2}^{\infty} u_s z^s, \mathfrak{v}(z) = \sum_{s=2}^{\infty} v_s z^s. \qquad (1)$$

Both $\mathfrak{u}$ and $\mathfrak{v}$ are analytic in the open unit disk $\mathbb{E} = \{z \in \mathbb{C}: |z| < 1\}$. If the condition $|\mathfrak{v}'(z)| < |\mathfrak{u}'(z)|$ holds in $\mathbb{E}$, then $\mathfrak{f}$ is locally univalent and sense-preserving in $\mathbb{E}$. It is important to note that, when $\mathfrak{v}(z)$ is identically zero, the class SH^0 reduces to the class S.

Let C and K denote the subclasses of S mapping $\mathbb{E}$ onto close-to-convex and convex domains, respectively. Similarly, CH^0 and $KH^0$are subclasses of SH^0, mapping $\mathbb{E}$ onto these respective domains [1-3].

Consider an analytic function $\mathfrak{u}$, where Salagean [4] defined the differential operator D^n of $\mathfrak{u}$ as follows:

$$D^0\mathfrak{u}(z) = \mathfrak{u}(z), \qquad (2)$$

$$D^1\mathfrak{u}(z) = D\mathfrak{u}(z) = z\mathfrak{u}'(z), \qquad (3)$$

$$D^n\mathfrak{u}(z) = D\left(D^{n-1}\mathfrak{u}(z)\right) \qquad (4)$$

where $n \in \mathbb{N}_0 = \{0,1,2,\dots\}$. For $\mathfrak{f} = \mathfrak{u} + \overline{\mathfrak{v}}$, Jahangiri et al. [5] defined the modified Salagean operator of $\mathfrak{f}$ as

$$D^n\mathfrak{f}(z) = D^n\mathfrak{u}(z) + (-1)^n\overline{D^n\mathfrak{v}(z)} \qquad (5)$$

where

$$D^n\mathfrak{u}(z) = z + \sum_{s=2}^{\infty} s^n u_s z^s,$$
$$D^n\mathfrak{v}(z) = \sum_{s=2}^{\infty} s^n v_s z^s. \qquad (6)$$

Cite as: S. Çakmak (2025). A Novel Subclass of Harmonic Functions: Coefficient Bounds, Distortion Bounds, and Closure Properties, *Sakarya University Journal of Science*, 29(2), 200-207. https://doi.org/10.16984/saufenbilder.1530460

Denote by $ACH(n)$ the class of functions $\mathfrak{f} = \mathfrak{u} + \overline{\mathfrak{v}}$ and satisfy

$$Re\left\{\left(D^n\mathfrak{u}(z)\right)'\right\} > \left|\left(D^n\mathfrak{v}(z)\right)'\right|. \quad (7)$$

It can be shown that the PH^0 class, as investigated by Ponnussamy et al. [6], is obtained for $n = 0$, and that the WH^0class, as investigated by Nagpal and Ravichandran [7], is obtained for $n = 1$. Furthermore, by selecting specific parameter values, the following well-known function classes can also be derived as special cases:

$ACH(0) \equiv PH(q \to 1^-, 0)$ [8]
$ACH(0) \equiv AH^0(1,0,0)$ [9]
$ACH(1) \equiv AH^0(1,1,0)$ [9]
$ACH(0) \equiv GH(0,1,0)$ [10]
$ACH(0) \equiv RH(0,0)$ [11]
$ACH(1) \equiv RH(1,0)$ [11]
$ACH(1) \equiv RH(1,1,0)$ [12]
$ACH(1) \equiv WH^0(3,1)$ [13]

For more information on function classes defined by high-order differential inequalities, refer to [14-17].

The class $AC(n)$ consists of functions $\mathfrak{u} \in S$ that satisfy the inequality:

$$Re\left\{\left(D^n\mathfrak{u}(z)\right)'\right\} > 0. \quad (8)$$

2. Geometric Properties of the Class $ACH(n)$

The first result provides a relationship between the function spaces $AC(n)$ and $ACH(n)$.

Theorem 2.1. The mapping $\mathfrak{f} = \mathfrak{u} + \overline{\mathfrak{v}} \in ACH(n)$ if and only if $\mathfrak{U}_\epsilon = \mathfrak{u} + \epsilon\mathfrak{v} \in AC(n)$ for each ϵ $(|\epsilon| = 1)$.

Proof. Suppose $\mathfrak{f} = \mathfrak{u} + \overline{\mathfrak{v}} \in ACH(n)$ and $\mathfrak{U}_\epsilon = \mathfrak{u} + \epsilon\mathfrak{v}$ for each ϵ $(|\epsilon| = 1)$,

$$\begin{aligned} Re\left\{\left(D^n\mathfrak{U}_\epsilon(z)\right)'\right\} &= Re\left\{\left(D^n\mathfrak{u}(z)\right)' + \epsilon\left(D^n\mathfrak{v}(z)\right)'\right\} \\ &> Re\left\{\left(D^n\mathfrak{u}(z)\right)'\right\} - \left|\left(D^n\mathfrak{v}(z)\right)'\right| \\ &> 0. \end{aligned}$$

Thus $\mathfrak{U}_\epsilon \in AC(n)$. Conversely, let $\mathfrak{U}_\epsilon = \mathfrak{u} + \epsilon\mathfrak{v} \in AC(n)$. We have

$$Re\left\{\left(D^n\mathfrak{u}(z)\right)'\right\} = Re\left\{-\epsilon\left(D^n\mathfrak{v}(z)\right)'\right\}.$$

With appropriate choice of ϵ $(|\epsilon| = 1)$; it follows that

$$Re\left\{\left(D^n\mathfrak{u}(z)\right)'\right\} > \left|\left(D^n\mathfrak{v}(z)\right)'\right|.$$

So, $\mathfrak{f} = \mathfrak{u} + \overline{\mathfrak{v}} \in ACH(n)$.

The next results provide a coefficient bound for functions in the $ACH(n)$class.

Theorem 2.2. Let $\mathfrak{f} = \mathfrak{u} + \overline{\mathfrak{v}} \in ACH(n)$ then for $s \geq 2$,

$$|v_s| \leq \frac{1}{s^{n+1}}. \quad (9)$$

Equality is achieved by the function $f(z) = z + \frac{1}{s^{n+1}}\overline{z}^s$.

Proof. Suppose that $\mathfrak{f} = \mathfrak{u} + \overline{\mathfrak{v}} \in ACH(n)$. If the series expansion of the function $\mathfrak{v}\left(re^{i\theta}\right)$ is used for $0 \leq r < 1$ and $\theta \in \mathbb{R}$, the following inequality is obtained:

$$\begin{aligned} & r^{s-1}s^{n+1}|v_s| \\ & \leq \frac{1}{2\pi}\int_0^{2\pi}\left|\left(D^n\mathfrak{v}\left(re^{i\theta}\right)\right)'\right|d\theta \\ & < \frac{1}{2\pi}\int_0^{2\pi} Re\left\{\left(D^n\mathfrak{u}\left(re^{i\theta}\right)\right)'\right\}d\theta \\ & = \frac{1}{2\pi}\int_0^{2\pi} Re\left\{1 + \sum_{s=2}^{\infty} s^{n+1}u_s r^{s-1}e^{i(s-1)\theta}\right\}d\theta \\ & = 1. \end{aligned}$$

Allowing $r \to 1^-$, we prove the result (9).

Theorem 2.3. Let $\mathfrak{f} = \mathfrak{u} + \overline{\mathfrak{v}} \in ACH(n)$ then for $s \geq 2$,

$$|u_s| + |v_s| \leq \frac{2}{s^{n+1}}.$$

Equality is achieved by the function $\mathfrak{f}(z) = z + \frac{2}{s^{n+1}} z^s$.

Proof. Suppose that $\mathfrak{f} = \mathfrak{u} + \overline{\mathfrak{v}} \in ACH(n)$, then from Theorem 2.2 $\mathfrak{U}_\epsilon = \mathfrak{u} + \epsilon\mathfrak{v} \in AC(n)$ for each ϵ ($|\epsilon| = 1$). Thus for each ϵ ($|\epsilon| = 1$), we have

$$Re\left\{\left(D^n\big(\mathfrak{u}(z) + \epsilon\mathfrak{v}(z)\big)\right)'\right\} > 0.$$

Therefore, $\left(D^n\big(\mathfrak{u}(z) + \epsilon\mathfrak{v}(z)\big)\right)' = P(z)$ can be achieved by an analytic function P having a positive real component in $\mathbb{E}$ and of the form $P(z) = 1 + \sum_{s=1}^{\infty} p_s z^s$. Then, we derive

$$m^{n+1}(u_s + \epsilon v_s) = p_{s-1} \quad for\ s \geq 2. \qquad (10)$$

Since $Re\{P(z)\} > 0$, we have $|p_s| \leq 2$ for $s \geq 1$. Hence, by equation (10), we get

$$s^{n+1}|u_s + \epsilon v_s| \leq 2 \quad for\ s \geq 2.$$

Since ϵ ($|\epsilon| = 1$) is arbitrary, it follows that the proof is concluded.

Now, we give a sufficient condition for a function to be in the class $ACH(n)$.

Theorem 2.4. Let $\mathfrak{f} = \mathfrak{u} + \overline{\mathfrak{v}} \in SH^0$ with

$$\sum_{s=2}^{\infty} s^{n+1}(|u_s| + |v_s|) \leq 1 \qquad (11)$$

then $\mathfrak{f} \in ACH(n)$. Equality holds for the function $\mathfrak{f}(z) = z + \frac{1}{s^{n+1}} z^s$.

Proof. Suppose that $\mathfrak{f} = \mathfrak{u} + \overline{\mathfrak{v}} \in SH^0$. Then using (11),

$$Re\left\{\left(D^n\mathfrak{u}(z)\right)'\right\} = Re\left\{1 + \sum_{s=2}^{\infty} s^{n+1} u_s z^{s-1}\right\}$$

$$> 1 - \sum_{s=2}^{\infty} s^{n+1}|u_s| \geq \sum_{s=2}^{\infty} s^{n+1}|v_s|$$

$$> \left|\sum_{s=2}^{\infty} s^{n+1} v_s z^{s-1}\right| = \left|\left(D^n\mathfrak{v}(z)\right)'\right|.$$

Hence, $\mathfrak{f} \in ACH(n)$.

This theorem highlights the distortion bounds for functions in the $ACH(n)$ class, showing how the function's derivatives can change or stretch values.

Theorem 2.5. Let $\mathfrak{f} \in ACH(n)$. Then

$$|z| + 2\sum_{s=2}^{\infty} \frac{(-1)^{s-1}|z|^s}{s} \leq |D^n\mathfrak{f}(z)|$$

and

$$|D^n\mathfrak{f}(z)| \leq |z| + 2\sum_{s=2}^{\infty} \frac{|z|^s}{s}.$$

Equality is satisfied for the function $\mathfrak{f}(z) = z + \sum_{s=2}^{\infty} \frac{2}{s^n} z^s$.

Proof. Let $\mathfrak{f} \in ACH(n)$. Then using Theorem 2.2, $\mathfrak{U}_\epsilon = \mathfrak{u} + \epsilon\mathfrak{v} \in AC(n)$ for each ϵ ($|\epsilon| = 1$). Moreover, there is an analytic function $\omega(z)$ such that

$$\left(D^n\mathfrak{U}_\epsilon(z)\right)' = \frac{1 + \omega(z)}{1 - \omega(z)} \qquad (12)$$

with $\omega(0) = 0$ and $|\omega(z)| < 1$ in $\mathbb{E}$.

Hence, we get

$$D^n\mathfrak{U}_\epsilon(z) = \int_0^z \frac{1 + \omega(t)}{1 - \omega(t)} dt = \int_0^{|z|} \frac{1 + \omega\left(re^{i\theta}\right)}{1 - \omega\left(re^{i\theta}\right)} e^{i\theta} dr.$$

Moreover using Schwarz Lemma, we have

$$|D^n\mathfrak{U}_\epsilon(z)| = \left|\int_0^{|z|} \frac{1 + \omega\left(re^{i\theta}\right)}{1 - \omega\left(re^{i\theta}\right)} e^{i\theta} dr\right|$$

$$\leq \int_0^{|z|} \frac{1 + r}{1 - r} dr$$

and

$$|D^n\mathfrak{U}_\epsilon(z)| = \left|\int_0^{|z|} \frac{1+\omega(re^{i\theta})}{1-\omega(re^{i\theta})} e^{i\theta} dr\right|$$
$$\geq \int_0^{|z|} Re\left\{\frac{1+\omega(re^{i\theta})}{1-\omega(re^{i\theta})}\right\} dr$$
$$\geq \int_0^{|z|} \frac{1-r}{1+r} dr.$$

Since

$$|D^n\mathfrak{U}_\epsilon(z)| = |D^n\mathfrak{u}(z) + \epsilon D^n\mathfrak{v}(z)|$$
$$\leq 1 + 2\sum_{s=1}^{\infty} |z|^s$$

and

$$|D^n\mathfrak{U}_\epsilon(z)| = |D^n\mathfrak{u}(z) + \epsilon D^n\mathfrak{v}(z)|$$
$$\geq 1 + 2\sum_{s=1}^{\infty} (-1)^s |z|^s,$$

in particular, we get

$$|D^n\mathfrak{u}(z)| + |D^n\mathfrak{v}(z)| \leq 1 + 2\sum_{s=1}^{\infty} |z|^s$$

and

$$|D^n\mathfrak{u}(z)| - |D^n\mathfrak{v}(z)| \geq 1 + 2\sum_{s=1}^{\infty} (-1)^s |z|^s.$$

Assume Γ is the radial segment extending from 0 to z, we get

$$|D^n\mathfrak{f}(z)| \leq \int_\Gamma (|D^n\mathfrak{u}(\zeta)| + |D^n\mathfrak{v}(\zeta)|)|d\zeta|$$
$$\leq \int_0^{|z|} \left(1 + 2\sum_{s=1}^{\infty} |z|^s\right) dt$$
$$= |z| + 2\sum_{s=1}^{\infty} \frac{|z|^{s+1}}{s+1}$$
$$= |z| + 2\sum_{s=2}^{\infty} \frac{|z|^s}{s}$$

and

$$|D^n\mathfrak{f}(z)| \geq \int_\Gamma (|D^n\mathfrak{u}(\zeta)| - |D^n\mathfrak{v}(\zeta)|)|d\zeta|$$
$$\geq \int_0^{|z|} \left(1 + 2\sum_{s=1}^{\infty} (-1)^s |z|^s\right) dt$$
$$= |z| + 2\sum_{s=2}^{\infty} \frac{(-1)^{s-1}|z|^s}{s}.$$

Next theorem shows that the $ACH(n)$ class is closed under convex combinations, meaning that any convex combination of functions in $ACH(n)$ will also belong to $ACH(n)$.

Theorem 2.6. The class $ACH(n)$ is closed under convex combinations.

Proof. Suppose $\mathfrak{f}_k = \mathfrak{u}_k + \overline{\mathfrak{v}_k} \in ACH(n)$ and $\sum_{k=1}^{\infty} c_k = 1$ $(0 \leq c_k \leq 1)$. The convex combination of functions f_k may be written as

$$\mathfrak{f}(z) = \sum_{k=1}^{\infty} c_k \mathfrak{f}_k(z) = \mathfrak{u}(z) + \overline{\mathfrak{v}(z)}$$

where

$$\mathfrak{u}(z) = z + \sum_{k=1}^{\infty} c_k \mathfrak{u}_k(z)$$

and

$$\mathfrak{v}(z) = \sum_{k=1}^{\infty} c_k \mathfrak{v}_k(z).$$

Both $\mathfrak{u}$ and $\mathfrak{v}$ are analytic functions within the open unit disk $\mathbb{E}$, satisfying the conditions $D^n\mathfrak{u}(0) = D^n\mathfrak{v}(0) = (D^n\mathfrak{u})'(0) - 1 = (D^n\mathfrak{v})'(0) = 0$ and

$$Re\left\{\left(D^n\mathfrak{u}(z)\right)'\right\} = Re\left\{\sum_{k=1}^{\infty} c_k \left(\left(D^n\mathfrak{u}_k(z)\right)'\right)\right\}$$
$$> \sum_{k=1}^{\infty} c_k \left|\left(D^n\mathfrak{v}_k(z)\right)'\right| \geq \left|\left(D^n\mathfrak{v}(z)\right)'\right|$$

showing that $\mathfrak{f} \in ACH(n)$.

If a sequence $\{u_s\}_{s=0}^{\infty}$ of non-negative real numbers satisfies the following criteria, it is

termed a "convex null sequence": as $s \to \infty$, a_s approaches 0, and the inequality

$u_0 - u_1 \geq u_1 - u_2 \geq \cdots \geq u_{s-1} - u_s \geq \cdots \geq 0$ holds.

We shall require the following Lemma 2.7, Lemma 2.8 and Lemma 2.9 to prove results of convolution.

Lemma 2.7. [18] When $\{a_s\}_{s=0}^{\infty}$ is a convex null sequence, then the function

$$Q(z) = \frac{a_0}{2} + \sum_{s=1}^{\infty} a_s z^s$$

is analytic, and the real part of $Q(z)$ is positive within the open unit disk $\mathbb{E}$.

Lemma 2.8. [19] Suppose the function Φ is analytic within the domain $\mathbb{E}$, satisfying $\Phi(0) = 1$ and $Re\,[\Phi(z)] > 1/2$ throughout $\mathbb{E}$. For any analytic function $\mathfrak{U}$ defined in $\mathbb{E}$, the function $\Phi * \mathfrak{U}$ maps to values within the convex hull of the image of $\mathbb{E}$ under $\mathfrak{U}$.

Lemma 2.9. Let $\mathfrak{U} \in AC(n)$, then $Re\left\{\frac{\mathfrak{U}(z)}{z}\right\} > \frac{1}{2}$.

Proof. Consider $\mathfrak{U}$ belonging to the class $AC(n)$, defined as $\mathfrak{U}(z) = z + \sum_{s=2}^{\infty} U_s z^s$. Then, the inequality

$$Re\left\{1 + \sum_{s=2}^{\infty} s^{n+1} U_s z^{s-1}\right\} > 0 \quad (z \in \mathbb{E})$$

can be equivalently expressed as $Re\{P(z)\} > \frac{1}{2}$ within the open unit disk $\mathbb{E}$, where

$$P(z) = 1 + \frac{1}{2}\sum_{s=2}^{\infty} s^{n+1} U_s z^{s-1}.$$

Consider a sequence $\{u_s\}_{s=0}^{\infty}$ defined by

$$u_0 = 1 \; ve \; u_{s-1} = \frac{2}{s^{n+1}} \quad \text{for } s \geq 2.$$

It is evident that the sequence $\{u_s\}_{s=0}^{\infty}$ forms a convex null sequence. By applying Lemma 2.7, we conclude that

$$Q(z) = \frac{1}{2} + \sum_{s=2}^{\infty} \frac{2}{s^{n+1}} z^{s-1}$$

is an analytic function and $Re\{Q(z)\} > 0$ within $\mathbb{E}$. Expressing

$$\frac{\mathfrak{U}(z)}{z} = P(z) * \left(1 + \sum_{s=2}^{\infty} \frac{2}{s^{n+1}} z^{s-1}\right),$$

and using Lemma 2.8, we arrive at the conclusion that $Re\left\{\frac{\mathfrak{U}(z)}{z}\right\} > \frac{1}{2}$ for z ∈ $\mathbb{E}$.

Theorem 2.10. Let $\mathfrak{U}_k \in AC(n)$ for $k = 1,2$. Then $\mathfrak{U}_1 * \mathfrak{U}_2 \in AC(n)$.

Proof. Suppose $\mathfrak{U}_1(z) = z + \sum_{s=2}^{\infty} U_s z^s$ and $\mathfrak{U}_2(z) = z + \sum_{s=2}^{\infty} V_s z^s$. Then the convolution of $\mathfrak{U}_1(z)$ and $\mathfrak{U}_2(z)$ is defined by

$$\mathfrak{U}(z) = (\mathfrak{U}_1 * \mathfrak{U}_2)(z) = z + \sum_{s=2}^{\infty} U_s V_s z^s.$$

Then, we have

$$\left(D^n \mathfrak{U}(z)\right)' = \left(D^n \mathfrak{U}_1(z)\right)' * \frac{\mathfrak{U}_2(z)}{z}. \qquad (13)$$

Since $\mathfrak{U}_1 \in AC(n)$, we get $Re\left\{\left(D^n \mathfrak{U}_1(z)\right)'\right\} > 0$. Moreover using Lemma 2.9, $Re\left\{\frac{\mathfrak{U}_2(z)}{z}\right\} > \frac{1}{2}$ in $\mathbb{E}$. Now applying Lemma 2.8 to (13) yields $Re\left\{\left(D^n \mathfrak{U}_1(z)\right)'\right\} > 0$ in $\mathbb{E}$. Thus, $\mathfrak{U} = \mathfrak{U}_1 * \mathfrak{U}_2 \in AC(n)$.

The next theorem shows that the $ACH(n)$ class is closed under the convolution operation, meaning that the convolution of functions in $ACH(n)$ will also belong to $ACH(n)$.

Theorem 2.11. Let $\mathfrak{f}_k \in ACH(n)$ for $k = 1,2$. Then $\mathfrak{f}_1 * \mathfrak{f}_2 \in ACH(n)$.

Proof. Suppose $\mathfrak{f}_k = \mathfrak{v}_k + \overline{\mathfrak{v}_k} \in ACH(n)$ with $k = 1,2$. The convolution $\mathfrak{f}_1 * \mathfrak{f}_2 = \mathfrak{u}_1 * \mathfrak{u}_2 + \overline{\mathfrak{v}_1 * \mathfrak{v}_2}$ is defined as the convolution of the

individual components of f_1 and f_2. To prove that $\mathfrak{f}_1 * \mathfrak{f}_2 \in ACH(n)$ we need to prove that $\mathfrak{U}_\epsilon = \mathfrak{u}_1 * \mathfrak{u}_2 + \epsilon(\mathfrak{v}_1 * \mathfrak{v}_2) \in AC(n)$ for each ϵ $(|\epsilon| = 1)$. By Teorem 2.10, the class $AC(n)$ is closed under convolutions for each ϵ $(|\epsilon| = 1), \mathfrak{u}_i + \epsilon\mathfrak{v}_i \in AC(n)$ for $i = 1,2$. we can assert that $AC(n)$ includes both $\mathfrak{U}_1$ and $\mathfrak{U}_2$, where

$\mathfrak{U}_1 = (\mathfrak{u}_1 - \mathfrak{v}_1) * (\mathfrak{u}_2 - \epsilon\mathfrak{v}_2)$ ve $\mathfrak{U}_2 = (\mathfrak{u}_1 + \mathfrak{v}_1) * (\mathfrak{u}_2 + \epsilon\mathfrak{v}_2)$.

combinations, we can form the function

$$\mathfrak{U}_\epsilon = \frac{1}{2}(\mathfrak{U}_1 + \mathfrak{U}_2) = \mathfrak{u}_1 * \mathfrak{u}_2 + \epsilon(\mathfrak{v}_1 * \mathfrak{v}_2)$$

belongs to $AC(n)$. Hence $ACH(n)$ is closed under convolution.

In the following example, we illustrate the application of the theoretical results.

Example 2.12. Let the functions $\mathfrak{f}(z) = \mathfrak{u}_1(z) + \overline{\mathfrak{v}_1}(z) = z + 0.075z^2 + 0.075\overline{z}^3$ and $\mathfrak{g}(z) = \mathfrak{u}_2(z) + \overline{\mathfrak{v}_2}(z) = z + 0.05z^2 - 0.05\overline{z}^3$ be given. Since $\mathfrak{u}_1(z) = z + 0.075z^2$, $\mathfrak{v}_1(z) = 0.075\overline{z}^3$, $\mathfrak{u}_2(z) = z + 0.075z^2$ and $\mathfrak{v}_2(z) = 0.075\overline{z}^3$ a straightforward computation yields $\left|\frac{\mathfrak{v}_1'(z)}{\mathfrak{u}_1'(z)}\right| < 1$ and $\left|\frac{\mathfrak{v}_2'(z)}{\mathfrak{u}_2'(z)}\right| < 1$. Consequently, the functions $\mathfrak{f}$ and $\mathfrak{g}$ belong to the SH^0 class. Moreover, since $4|0.075| + 9|0.075| = 0.975 < 1$ and $4|0.05| + 9|0.05| = 0.065 < 1$, by Theorem 2.4 the functions $\mathfrak{f}$ belongs to the $ACH(1)$ class. On the other hand, the function $\mathfrak{h}(z) = \mathfrak{f}(z) * \mathfrak{g}(z) = \mathfrak{u}_3(z) + \overline{\mathfrak{v}_3}(z) = z + 0.00375z^2 - 0.00375\overline{z}^3$, is similarly easily obtained to belong to the class $ACH(1)$.

The images of the unit disk $\mathbb{E}$ under the mappings $\mathfrak{f}$, $\mathfrak{g}$ and $\mathfrak{h}$ are shown in Figure 1, Figure 2, and Figure 3, respectively.

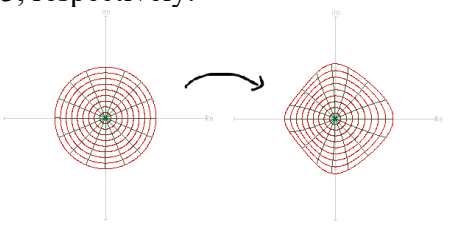

Figure 1. Image of the unit disk under the function $\mathfrak{f}$.

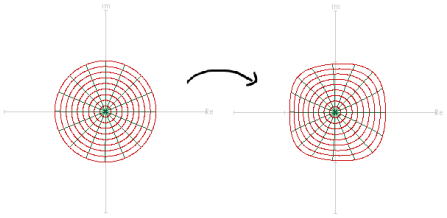

Figure 2. Image of the unit disk under the function $\mathfrak{g}$.

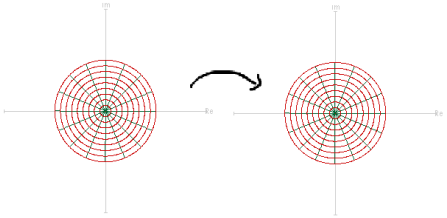

Figure 3. Image of the unit disk under the function $\mathfrak{h}$.

3. Conclusion

In this paper, we introduce a new subclass of harmonic functions. We also thoroughly analyze its properties. We derived precise coefficient bounds and distortion bounds that characterize the behavior of functions within this subclass. Additionally, we established sufficient conditions for coefficients that ensure the functions meet the desired criteria. Our results also demonstrate that this subclass is closed under both convex combinations and convolutions, highlighting its robustness and applicability. These findings contribute to the broader understanding of harmonic functions and provide a foundation for future research in geometric function theory.

Article Information Form

Funding

The author has not received any financial support for the research, authorship, or publication of this study.

The Declaration of Conflict of Interest/ Common Interest

The author declares that there is no conflict of interest or common interest related to this study.

The Declaration of Ethics Committee Approval

This study does not require ethics committee permission or any special permission.

The Declaration of Research and Publication Ethics

The author declares compliance with the scientific, ethical, and citation rules of SAUJS throughout all stages of this study. No falsification has been made in the collected data. Additionally, the author states that Sakarya University Journal of Science and its editorial board bear no responsibility for any potential ethical violations. This study has not been submitted for evaluation or publication in any academic platform other than Sakarya University Journal of Science.

Copyright Statement

References

[1] J. Clunie, T. Sheil-Small, "Harmonic univalent functions," Annales Fennici Mathematici, vol. 9, no. 1, pp. 3-25, 1984.

[2] M. Dorff, "Convolutions of planar harmonic convex mappings," Complex Variables and Elliptic Equations, vol. 45, no. 3, pp. 263-271, 2001.

[3] P. Duren, Harmonic mappings in the plane, vol. 156. Cambridge: Cambridge University Press, 2004.

[4] G. S. Salagean, "Subclass of univalent functions," in Complex Analysis-Fifth Romanian Finish Seminar, Bucharest, 1983, pp. 362-372.

[5] J. M. Jahangiri, G. Murugusundaramoorthy, K. Vijaya, "Salagean-type harmonic univalent functions," Southwest Journal of Pure and Applied Mathematics, vol. 2, pp. 77-82, 2002.

[6] S. Ponnusamy, H. Yamamoto, H. Yanagihara, "Variability regions for certain families of harmonic univalent mappings," Complex Variables and Elliptic Equations, vol. 58, no. 1, pp. 23-34, 2013.

[7] S. Nagpal, V. Ravichandran, "Construction of subclasses of univalent harmonic mappings," Journal of the Korean Mathematical Society, vol. 53, pp. 567-592, 2014.

[8] S. Çakmak, "On Properties of $ q $-Close-to-Convex Harmonic Functions of Order α," Turkish Journal of Mathematics and Computer Science, vol. 16, no. 2, pp. 471-480, 2024.

[9] S. Cakmak, E. Yaşar and S. Yalçın, "Some basic properties of a subclass of close-to-convex harmonic mappings," Turkic World Mathematical Society (TWMS) Journal of Pure and Applied Mathematics, vol. 15, no.2, pp.163–173, 2024.

[10] S. Çakmak, E. Yaşar, S. Yalçın, "Some basic geometric properties of a subclass of harmonic mappings," Boletín de la Sociedad Matemática Mexicana, vol. 28, no.2, pp. 54, 2022.

[11] E. Yaşar, S. Y. TOKGÖZ, "Close-to-convexity of a class of harmonic mappings defined by a third-order differential inequality," Turkish Journal of Mathematics, vol. 45, no.2, pp. 678-694, 2021.

[12] S. Çakmak, E. Yaşar, S. Yalçın, "New subclass of the class of close-to-convex harmonic mappings defined by a third-order differential inequality," Hacettepe Journal of Mathematics and Statistics, vol. 51, no.1, pp. 172-186, 2022.

[13] D. Breaz, A. Durmuş, S. Yalçın, L. I. Cotirla, H. Bayram, "Certain Properties of Harmonic Functions Defined by a Second-Order Differential Inequality," Mathematics, vol.11, no.19, 4039, 2023.

[14] S. Çakmak, S. Yalçin. (2025, Feb, 7). Introducing a Novel Subclass of Harmonic Functions with Close-to-Convex Properties. arXiv preprint arXiv:2502.04019. Available: https://arxiv.org/abs/2502.04019

[15] S. Yalçın, H. Bayram, G. I. Oros, “Some Properties and Graphical Applications of a New Subclass of Harmonic Functions Defined by a Differential Inequality,” Mathematics, vol. 12, no.15, 2338, 2024.

[16] M. Nas, S. Yalçın, H. Bayram, “A Class of Analytic Functions Defined by a Second Order Differential Inequality and Error Function,” International Journal of Applied and Computational Mathematics, vol. 10, no.2, pp. 42, 2024.

[17] S, Çakmak, “Regarding a novel subclass of harmonic multivalent functions defined by higher-order differential inequality,” Iranian Journal of Science, vol. 48, no. 6, pp. 1541-1550, 2024.

[18] L. Fejér, " Uber die Positivit\"at von Summen, die nach trigonometrischen oder Legendreschen Funktionen fortschreiten,” Acta Litteraria Academiae Scientiarum Hungaricae Szegediensis, pp. 75-86, 1925.

[19] R. Singh, S. Singh, "Convolution properties of a class of starlike functions," Proceedings of the American Mathematical Society, vol. 106, no. 1, pp. 145-152, 1989.

Sakarya Üniversitesi Fen Bilimleri Dergisi
Sakarya University Journal of Science

e-ISSN : 2147-835X
Publisher : Sakarya University

Vol. 29, No. 2, 208-217, 2025
DOI: https://doi.org/10.16984/saufenbilder.1356825

Research Article

Bioaccumulation of Nickel Ions by *Rhizopus delemar*

Gülşah Başkan[1*], Ünsal Açıkel[2]

[1] Uşak University, Technology Transfer Office, Project Support Unit, Uşak, Türkiye, gulsah.mersin@usak.edu.tr, ror.org/05es91y67
[2] Sivas Cumhuriyet University, Engineering Faculty, Department of Chemical Engineering, Sivas, Türkiye, uacikel@cumhuriyet.edu.tr, ror.org/04f81fm77
*Corresponding Author

ARTICLE INFO

Keywords:
Rhizopus delemar
Bioaccumulation
Nickel
Microbial growth
Molasses sucrose

Article History:
Received: 07.09.2023
Revised: 06.02.2025
Accepted: 27.03.2025
Online Available: 15.04.2025

ABSTRACT

The current research investigated the bioaccumulation of Ni(II) ions by *Rhizopus delemar* in molasses-containing fluids in a batch reactor. Due to the low pH requirements that *R. delemar* requires, it may grow in wastewater, which has an acidic pH. In the absence of Ni(II) ions, the influence of pH and molasses concentration on the growth rate and concentration of *R. delemar* were examined. The highest level of microbial growth occurred at a pH of 4.0. Up to 20 g/L of sucrose content increased the maximum *R. delemar* concentration and the specific growth rate. While the substrate content in each growing medium including molasses was kept constant at 10 g/L, initial concentrations of metal ions were changed between 50 and 250 mg/L to evaluate the bioaccumulation of Ni(II) ions. It was discovered that when metal ions existed, the rate of microorganism growth slowed down as the metal ion concentration increased. The maximum growth rates were discovered to be 0.257 h^{-1} in the presence of 50 mg/L Ni(II). When media containing 50 mg/L Ni(II) ions, the efficiency of Ni(II) bioaccumulation was found to be 51.8%.

1. Introduction

Along with the growth of industry and human activities, the concentration of heavy metals in wastewater has been growing. Heavy metal-containing wastewater that enters the environment endangers both the ecology and the health of people. Heavy metals are dangerous because they cannot biodegrade and may result in cancer [1]. The heavy metals from different industries that are of the most concern include lead, zinc, copper, cadmium, chromium, and nickel. These substances come from a variety of sources, including metal complex dyes, insecticides, fertilizers, textile fixing agents, and bleaching agents [2]. Tolerable limits for various heavy metals in drinking water have been established by the WHO [3]. Heavy metal removal from industrial effluents is accomplished using conventional treatment methods such as chemical precipitation, ion exchange, coagulation/flocculation, adsorption, and electrochemical removal.

The ineffective removal of heavy metals and the production of toxic sludge are just two of the significant drawbacks of these low-cost systems. Reverse osmosis, nanofiltration, and ultrafiltration, among other membrane separation techniques, have all been applied to the treatment of water in recent years [4]. Because the production of activated carbon and ion exchange resins is dependent on fossil fuels such as coal and oil, they are not sustainable. However, the bioaccumulation technique is commonly favoured for its affordability, environmental friendliness, and ease of usage [5].

Heavy metals enter microorganisms' interior spaces via bioaccumulation, a metabolically active process involving the importer compounds that form a translocation channel across the

Cite as: G. Başkan, Ü. Açıkel (2025). Bioaccumulation of Nickel Ions by *Rhizopus delemar*, *Sakarya University Journal of Science*, 29(2), 208-217. https://doi.org/10.16984/saufenbilder.1356825

bilayer of lipids. The heavy metals can be trapped inside the intracellular space by proteins and peptide ligands [6]. Metal is actively bioaccumulated by microorganisms. Numerous microorganisms, such as bacteria, algae, and fungi, have bioaccumulated metals from polluted habitats. The microorganisms that are utilized for bioaccumulation should be capable of withstanding one or more contaminants at increasing concentrations.

Additionally, they might be able to biotransform hazardous chemicals into less toxic or benign forms, reducing the toxicity of the pollutant and keeping it confined [7]. The bioaccumulation process involves two steps. In the first stage, metal ions cover the cell's surface, and metabolism is passive. The cell is then entered by metal ions. Only metabolically active cells can complete the second stage. If the second stage's ideal circumstances for organism growth are maintained, biomass production rises. This makes it possible for larger concentrations of metal ions to bind [8].

Bioremoval cultivating cultures may eliminate the requirement for other sources of biomass technologies such as cultivation, harvesting, drying, etc., but the uses of these methods are limited by the requirements of sustaining cell growth [9]. Additionally, environmental factors like temperature, pH, and biomass content always have a substantial influence on how well living cells can take in metal ions [10].

Fungi's cell walls are largely made up of polysaccharides which account for around 80% of their dry weight and may make up an additional 30% of their dry weight. According to Mir-Tutusaus et al. [11], fungi contain a large number of cell wall components with a high capacity to bind metals, making them efficient bio-sorbents. Fungi's cell walls include significant amounts of chitin, chitosan, glucan, and mannan in addition to a small quantity of glycoprotein. These polymers commonly contain hydroxyl (OH), carboxyl (R-COOH or R-CO_2H), amine (NH_2), and phosphate (PO_4^-, PO_3^-) functional groups as metal-binding ligands [12]. Fungi are inexpensive, kind to the environment, and abundant in nature [13]. It is known that the fungus uses both metabolism-dependent and independent mechanisms to survive in environments with high metal stress.

R. delemar is an opportunistic pathogen that lives in the soil on decaying plants [14] and is known as a superb metal accumulator. The maximum Cu(II) bioaccumulation was measured by *R. delemar* at pH 6.0, 32.6°C, with an initial concentration of 50 mg/L of Cu(II) [15]. Similar to this, *R. delamar* determined the maximal Zn(II) removal to be 26.31 mg/L in the bioaccumulation medium containing 30 mg/L Zn(II) initially at pH 5.0 and 35°C [16]. *R. arrhizus* was able to remove the most Cu(II) at an initial concentration of 75 mg/L, with a maximum specific intake of 10.76 mg/g [9].

Nickel is a common industrial chemical that is also regarded as a prominent pollutant of aquatic ecosystems. Basically, Ni forms soluble salts with other chemicals in aquatic ecosystems, which can adsorb onto other substances and have a variety of synergistic and antagonistic effects. Numerous factors, such as Ni concentration, water quality, and an organism's physiological state, affect the degree of Ni toxicity. In aquatic systems, nickel is a major contaminant. It has been stated that fish exposed to nickel collect nickel in their gills. Fish have suffered from compromised digestive and respiratory systems as a result. Ion regulation in fish is inhibited by Ni poisoning, which results in oxidative stress [17]. The World Health Organization (WHO) has established a Ni limit of 0.07 mg/L in drinking water [18].

The uptake of Ni(II) ions by *R. delemar* in a molasses medium was studied in this work both with and without Ni(II) ions. It was found that *R. delemar* may be used as an efficient biomass for metal ion bioremoval, such as Ni(II).

2. General Methods

2.1. *R. delemar* growth and preparation for bioaccumulation

The Fungi, *R. delemar,* was provided for the work by the NRRL of the US Department of Agriculture. The growing medium for *R. delemar* contains 2.0 g/L yeast extract, 0.5 g/L K_2HPO_4, 0.2 g/L $MgSO_4.7H_2O$, and 10 g/L molasses

sucrose. To accomplish the sterilization procedure, the growth medium was autoclaved (t: 15 min T: 121°C P: 1.2 atm). We bought KH_2PO_4 and $MgSO_4.7H_2O$ from Sigma Aldrich Company. A sugar plant in Ankara (Türkiye) offered the molasses sucrose. For the *R. delemar* development, molasses served as the only carbon source.

2.2. Bioaccumulation media preparation

$Ni(NO_3)_2$ was added to in distilled water at an average concentration of 1.0 g/L to make Ni(II) solution from stock. The prepared fermentation media had a range of 50 to 500 mg/L for metal concentrations. By adding HNO_3 (0.1 N) and NaOH (0.1 N) the fermentation media's pH was set to 4.0.

2.3. Bioaccumulation studies and measurements of the concentrations of *R. delemar*, molasses sucrose, and Ni(II)

In a batch system with a working capacity of 100 mL, bioaccumulation tests were conducted at a temperature of 25°C. The experiments employed a shaker running at 150 rpm. Once the cells had entered the exponential growth phase, sterilization was done to keep additional microorganisms out of the growth medium. The cells were modified with metal ion-containing media before inoculum. A 1 mL solution of microorganisms was added to begin the bioaccumulation tests. At time periods, samples from growing media were removed and centrifuged. The quantity of sucrose in the collected liquid was determined using a UV-Vis spectrophotometer (CHEBIOUS UV-spectrophotometer) set at 575 nm. Dinitrosalicylicacid was employed to color sucrose complexes. The quantity of unbioaccumulated Ni(II) ions in the effluent was measured at 232 nm using an AAS (GBC Avanta) with an air-acetylene flame. At 360 nm, the culture medium was measured spectrophotometrically [19].

2.4. Modelling growth and bioaccumulation of *R. delemar*

Models of microbial growth often depict variation in the maximum specific growth rate (μm), which is a reflection of metabolic activity [20]. Using microorganism cultures, microbial growth can be examined and modeled. The growth of a microorganism isolate is depicted by a sigmoidal curve made up of distinct and distinguishable growth phases including lag, exponential (log), stationary, and death (Fig. 1) [21].

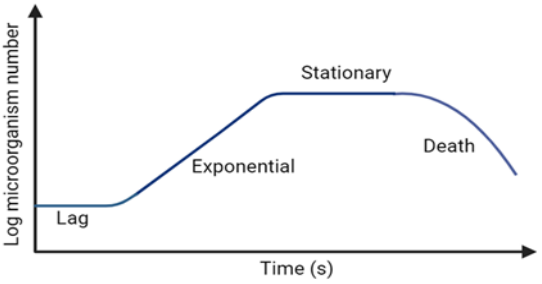

Figure 1. The microorganism batch-culture growth curve

In the batch system, the specific growth rate is used to indicate how the concentration of microorganisms changes over time during the exponential growth phase.

$$\frac{dX}{dt} = \mu X \quad (1)$$

Equation 2 is obtained by integrating Equation 1 at the boundary conditions of $X=X_o$ at time t=0 and X=X at time t=t.

$$In\frac{X}{X_0} = \mu t \quad (2)$$

where μ is specific growth rate (h^{-1}), X is dry microorganism concentration (g /L), and t is time (h).
The connection between the quantity of the rate-limiting nutrient (sucrose) and the specific growth rate may be determined using the Monod growth kinetics expression in the absence of inhibition. The formula is shown as follows:

$$\mu = \frac{\mu_m S}{K_s + S} \quad (3)$$

where Ks is the saturation constant (g/L), and μ_m is the maximum specific growth rate when S>>Ks [22].

The uptake of Ni(II) by *R. delemar* was determined using the following equation 4:

$$q = \frac{C_i - C_f}{X} = \frac{C_{acc}}{X} \quad (4)$$

where q is bioaccumulated Ni(II) ions per unit weight of dried biomass (mg/g mo), C_i is the initial Ni(II) ion concentration (mg/L), C_f is the residual Ni(II) concentration in solution (mg/L), X represents the amount of microorganisms per liter (g/L), and C_{acc} is the amount of bioaccumulated Ni(II) ions per liter (mg/L) [23]. The removal percentages of Ni(II) were determined with an equation as below:

$$\%removal = \frac{C_i - C_{eq}}{C_i} x100 \quad (5)$$

where C_o is the initial Ni(II) concentration (mg/L) and C_{eq} is the residual metal concentration at equilibrium (mg/L).

3. Results and Discussion

3.1. Influence of pH on microbial growth of *R. delemar*

Environmental elements necessary for microbial survival and development are influenced by pH. By altering the salinity and composition of aqueous solutions, it controls the bioavailability of nutrients and trace elements. Additionally, pH affects the reactivity of naturally occurring organic matter as well as the activities of extracellular enzymes [24]. pH could inhibit microbial metabolism. The majority of laboratory cultures are found in a pH range of 3–4 units, which corresponds to a 3–4 order of magnitude difference in proton chemical activity [20]. Based on their optimal growth pH, microorganisms may be divided into three groups: alkaliphiles, which grow quickly above pH 9, neutrophiles, which grow best between pH 5 and 9, and acidophiles, which grow best at pH 5 [25]. When the ambient pH deviates from the optimal pH ranges, microbial growth rates decrease. The topologies of microbial populations can be affected by pH through changing the thermodynamics and kinetics of redox reactions. Numerous redox activities produce or consume protons, hence pH affects the free energy outputs of these processes [26].

The pH of wastewater is significantly impacted by the presence of heavy metals in natural circumstances [27]. To study the impact of pH on microorganisms concentration and specific growth rate, the growth media's pH was changed between 2.0 and 5.0. At pH 4.0, the highest concentration and growth rate of *R. delemar* were found to be 3.76 g/L and 0.297 h^{-1} respectively as shown in Fig. 2. According to Evirgen and Sağ Acikel [16], the greatest biomass concentrations of *R. delemar* were achieved on days 4 and 5 of development, at pH 5.0 and temperatures of 25 and 35 °C, respectively, in the metal-free medium. These concentrations were 1.09 and 1.16 g/L, respectively [16].

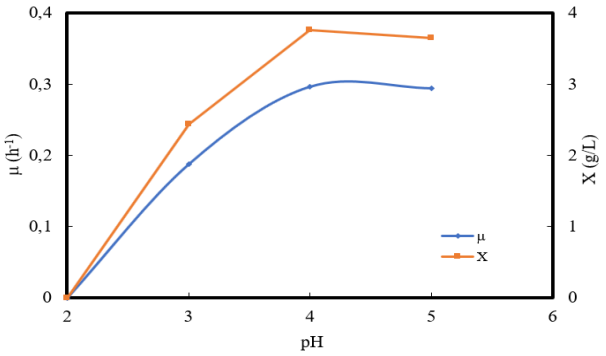

Figure 2. Effect of the initial pH value on the maximum concentration of microorganisms and the specific growth rate (S_o: 10 g/L)

Functional groups on the fungal cell surface, such as COOH, OH, NH_2, and PO_4^{3-}, are important for the sorption of heavy metal ions and display different behaviors depending on the medium's pH. The chemical properties of the biomaterial and their surface functional groups (including COOH, PO_4^{2-}, and NH_2) were significantly influenced by the pH of the medium [28].

3.2. The effect of initial sucrose content on *R. delemar* microbiological growth

Molasses, which contain a high concentration of sugars, is a low-cost feedstock for the generation of value-added bioproducts via bioconversion [29]. It can be used as a resource for ethanol production since it contains carbon sources required for yeast strain growth and metabolism [30]. Research shows that molasses is a suitable medium for the cultivation of microorganisms such as algae [31], yeast [32] and bacteria [33].

Table 1 shows the results of testing the effects of molasses sucrose concentration on specific growth rates and maximum microorganism concentrations at concentrations ranging from 1 to 20 g/L. The specific growth rate and maximum

microorganisms concentration were found a 0.365 h^{-1} and 4.55 g/L, respectively at 20 g/L sucrose concentration. Using the Monod equation, the maximum specific growth rate and saturation constant were estimated to be 0.406 h^{-1} and 24.182 g/L, respectively. According to Aksu and Dönmez, raising the sucrose content from 5 to 20 g/L enhanced the specific growth rate of *Kluyveromyces* cells from 0.090 to 0.222 h^{-1} [34]. Authors in another research achieved similar results. *Candida* cell specific growth rate increased from 2.28 to 4.80 day^{-1} when sucrose concentration was raised from 5 to 15 g/L in the absence of dye anions [35].

Table 1. Specific growth rates and maximum concentrations of *R. delemar* at different molasses concentration

S_o (g/L)	μ (h^{-1})	X (g/L)
1	0.085	0.98
2	0.145	1.67
5	0.212	2.55
10	0.297	3.76
15	0.350	4.24
20	0.365	4.55

3.3. The influence of initial nickel concentration on *R. delemar* growth

The majority of microorganisms have a biphasic reaction to a variety of heavy metals. Growth is promoted at low metal concentrations, but as the metal concentration grows, growth is hindered and finally ceases. The "transition" area between metal excitation and inhibition is often in a relatively small concentration range [36].

The bioaccumulation of Ni(II) ions in *R. delemar* was studied at initial molasses sucrose concentrations of 10 g/L, pH 4.0, and initial metal ion concentrations ranging from 50 to 500 mg/L. Fig. 3 depicts the relationship between the specific growth rate, the maximum microorganism concentration, and initial metal ion concentrations. As the initial Ni(II) ion concentration grew up to 500 mg/L, the specific growth rate and maximum microorganism concentration dropped. Metal ion concentrations rose in the growth medium, impeding microorganism development. At 100 mg/L initial Ni(II) ion concentration, the specific growth rate and maximum microorganisms concentration were 0.222 h^{-1} and 2.36 g/L, respectively. Açıkel and Alp [37] stated that as the initial metal ion concentration increased, *R. delemar* growth was inhibited. *Aspergillus niger* growth was detected in the presence of Cu(II), Pb(II), and Cr(VI) ions by Dursun et al. [38].

Maximum biomass production by *A. niger* has been documented in the absence of metal ions, but all tested amounts of Cr(VI) hindered growth. Additionally, according to Acikel and Ersan [39], the specific growth rates of *R. delemar* dramatically decreased when Ni(II) ion concentrations increased in the region of 0–50 mg/L. Naskar et al. [40] studied the bioaccumulation of Ni(II) in developing *Bacillus sp.* cells. They reported that no increase in microbial growth at metal ion concentration over 50 mg/L.

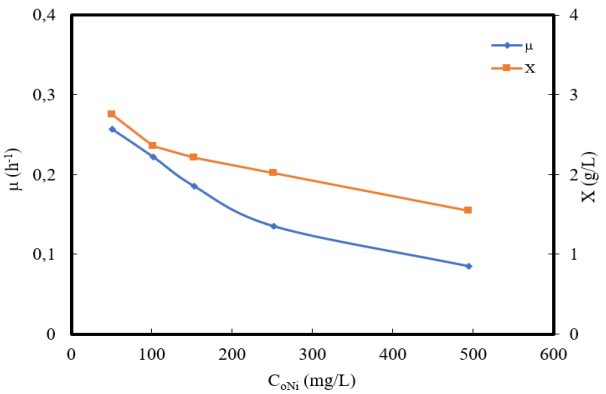

Figure 3. The effect of initial nickel content on the specific growth rate and maximum microorganism concentration of *R. delemar* (S_o: 10 g/L)

Through various interactions with enzymes involved in biodegradation or general metabolism, metal ions have been demonstrated to inhibit microbial processes [41]. Metal ions (e.g., Cd^{2+}) are capable of binding to DNA bases to break single-stranded DNA or binding to sulfhydryl (-SH) groups of enzymes [42]. Metal ions may substitute for physiologically essential cations within an enzyme, for example, Cd^{2+} substitutes for Zn^{2+} [43]. Three patterns of the detrimental effects of metal ions on cytoplasmic biodegradation have been observed at the level of microbial communities. (1) As metal ion concentration rises, inhibition rises gradually. (2) High metal ion concentrations impede biodegradation, while low metal ion concentrations promote it. (3) Biodegradation is less inhibited by high metal concentrations than

by low amounts of metal. So, in order to resist hazardous metals, microbes have evolved to use a variety of techniques, such as metal reduction, metal efflux pump, and metal chelate synthesis. As a result, various biological systems may be more or less tolerant of certain metal ions depending on their toxicity and effect [44].

3.4. The influence of the initial concentration of nickel on bioaccumulation

The correlation between bioaccumulated Ni(II) ion concentrations and the quantity of Ni(II) bioaccumulated per unit dry weight of *R. delemar* versus initial Ni(II) ion concentration is depicted in Fig. 4. The bioaccumulated Ni(II) ion concentrations and quantities of Ni(II) bioaccumulated per unit dry weight of fungal cell at 100 mg/L initial Ni(II) ion concentration were 48.8 mg/L and 20.67 g Ni(II)/g dry weight of microorganism, respectively. Li et al. [45] investigated cadmium bioaccumulation in *Zygosaccharomyces rouxii* and *Saccharomyces cerevisiae* cultures. They found that both yeasts had a high cadmium removal rate at low cadmium concentrations. At the same initial cadmium concentration, *Z. rouxii* had a greater removal rate than *S. cerevisiae*. Total, intracellular and cell-surface cadmium bioaccumulation of both yeasts increased when cadmium concentrations rose in the medium.

The bioaccumulation efficiency of *R. delemar* decreased as the initial metal ion concentration increased (Table 2). The removal efficiency decreased from 51.75% to 20.44% when initial metal ion concentration increased from 50 mg/L to 500 mg/L. Heat-treated *Saccharomyces cerevisiae* were tested for their ability to remove Cu(II) ions from aqueous solutions by Stanescu et al. [46].

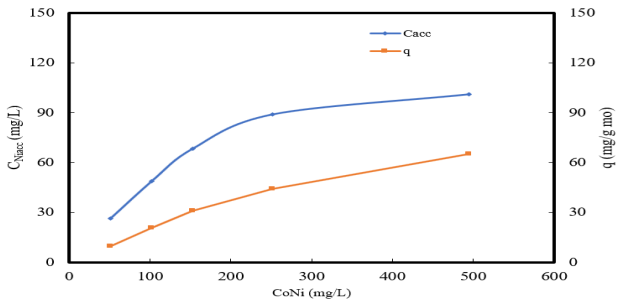

Figure 4. The effect of initial nickel concentration on bioaccumulated nickel concentration and bioaccumulated nickel quantity per unit dry weight of microorganism (S_o: 10 g/L)

They discovered that as the initial metal concentration increased, the removal efficiency declined (55.89-39.04%) for the most concentrated samples (100-250 mg/L). This is due to Ni(II) ions in solution not being connected to the biomass at greater concentrations due to biomass saturation induced by an increase in the number of ions competing for available binding sites.

Table 2. Bioaccumulation efficiency of nickel in the growth medium (S_o=10 g/L)

C_{oNi} (mg/L)	S_o (g/L)	Bioaccumulation efficiency %
50	10.12	51.75
100	9.95	47.70
150	10.15	44.91
250	9.98	35.30
500	9.95	20.44

Toxic contaminants in soil or water can be reduced or removed using fungus. According to the species, type, and concentration of the heavy metal, the threshold for the fungus's tolerance to it varies, ensuring that the inhibition of growth by a low concentration of one metal does not pose a barrier to its tolerance of another metal with a high concentration. Most likely, inherent physiological mechanisms are to blame for the variance in how different fungi react to trace metals. Most fungi species are not universally sensitive to all metals, even if they are sensitive to one or more types of metals [47].

4. Conclusion

The bioaccumulation of Ni(II) ions by *R. delemar* in molasses media in the presence and absence of Ni(II) ions was investigated in this work. The removal of comparatively non-toxic metals through bioaccumulation is very promising, but the detrimental effects of toxic metals make this process complex. *R. delemar* was able to remove Ni(II) at low concentrations, which was mostly due to intracellular Ni(II) bioaccumulation. Microbial growth was greatest at pH: 4 and 25°C. Increases in molasses sucrose content up to 20 g/L resulted in increases in growth rate and microorganism concentration. The rate of microorganism growth slowed when metal ion concentration increased. The removal % of Ni(II) bioaccumulation by *R. delemar* reduced as initial Ni(II) concentrations increased.

We think that *R. delemar* might be used as a biomass for Ni(II) removal in wastewater. A more complete research of operational parameters such as temperature, biomass content, agitation, and so on should be carried out to better understand *R. delemar*'s Ni(II) bioaccumulation.

Article Information Form

Funding
Authors has no received any financial support for the research, authorship or publication of this study.

Authors Contribution
Authors contributed equally to the study.

The Declaration of Conflict of Interest/ Common Interest
No conflict of interest or common interest has been declared by authors.

The Declaration of Ethics Committee Approval
This study does not require ethics committee permission or any special permission.

The Declaration of Research and Publication Ethics
Authors of the paper declare that they comply with the scientific, ethical and quotation rules of SAUJS in all processes of the paper and that they do not make any falsification on the data collected. In addition, they declare that Sakarya University Journal of Science and its editorial board have no responsibility for any ethical violations that may be encountered, and that this study has not been evaluated in any academic publication environment other than Sakarya University Journal of Science.

References

[1] N. A. A. Qasem, R. H. Mohammed, D. U. Lawal, "Removal of heavy metal ions from wastewater: A comprehensive and critical review", NPJ Clean Water, vol. 4, no. 36, 2021.

[2] Renu, M. Agarwal, K. Singh, "Heavy metal removal from wastewater using various adsorbents: A review", Journal of Water Reuse and Desalination, vol. 7, no. 4, pp. 387-419, 2017.

[3] E. Priyadarshini, S. S. Priyadarshini, B. G. Cousins, N. Pradhan, "Metal-Fungus interaction: Review on cellular processes underlying heavy metal detoxification and synthesis of metal nanoparticles", Chemosphere, vol. 274, 2021.

[4] R. Shrestha, S. Ban, S. Devkota, S. Sharma, R. Joshi, A. P. Tiwari, H. Y. Kim, M. K. Joshi, "Technological trends in heavy metals removal from industrial wastewater: A review", Journal of Environmental Chemical Engineering, vol. 9, no. 4, 2021.

[5] P. Diep, R. Mahadevan, A. F. Yakunin, "Heavy metal removal by bioaccumulation using genetically engineered microorganisms", Frontiers in Bioengineering and Biotechnology, vol. 6, 2018.

[6] A. Mishra, A. Malik, "Recent advances in microbial metal bioaccumulation", Critical Reviews in Environmental Science and Technology, vol. 43, no. 11, pp. 1162-1222, 2013.

[7] N. D. Nnaji, H. Onyeaka, T. Miri, C. Ugwa, "Bioaccumulation for heavy metal removal: A review", SN Applied Sciences, vol. 5, no. 125, 2023.

[8] M. Zabochnicka-Świątek, M. Krzywonos, "Potentials of biosorption and bioaccumulation processes for heavy metal removal", Polish Journal of Environmental Studies, vol. 23, no. 2, pp. 551-561, 2014.

[9] A. Y. Dursun, G. Uslu, O. Tepe, Y. Cuci, H. I. Ekiz, "A comparative investigation on the bioaccumulation of heavy metal ions by growing *Rhizopus arrhizus* and *Aspergillus niger*" Biochemical Engineering Journal, vol. 15, no. 2, pp. 87-92, 2003.

[10] F. Aslam, A. Yasmin, S. Sohail, "Bioaccumulation of lead, chromium, and nickel by bacteria from three different genera isolated from industrial effluent", International Microbiology, vol. 23, no. 2, pp. 253-261, 2020.

[11] J. A. Mir-Tutusaus, R. Baccar, G. Caminal, M. Sarrà, "Can white-rot fungi be a real wastewater treatment alternative for organic micropollutants removal? A review", Water Research, vol. 138, pp. 137-151, 2018.

[12] A. Singh, D. B. Pal, A. Mohammad, A. Alhazmi, S. Haque, T. Yoon, N. Srivastava, V. K. Gupta, "Biological remediation technologies for dyes and heavy metals in wastewater treatment: New insight", Bioresource Technology, vol. 343, 2022.

[13] Y. Li, G. Zou, S. Yang, Z. Wang, T. Chen, X. Yu, Q. Guo, R. He, T. Duan, W. Zhu, "Integration of bio-inspired adsorption and photodegradation for the treatment of organics-containing radioactive wastewater", Chemical Engineering Journal, vol. 364, pp. 139-145, 2019.

[14] Q. J. Choudhury, S. Ambati, Z. A. Lewis, R. B. Meagher, "Targeted delivery of antifungal liposomes to *Rhizopus delemar*", Journal of Fungi, vol. 8, no. 4, 2022.

[15] O. A. Evirgen, Y. S. Acikel, "Simultaneous copper bioaccumulation, growth and lipase production of Rhizopus delemar in molasses medium: Optimisation of environmental conditions using RSM", Chemistry and Ecology, vol. 30, no. 1, pp. 39-51, 2014.

[16] O. A. Evirgen, Y. S. Acikel, "Investigation of mutual interactions of physicochemical parameters on simultaneous Zn(II) bioaccumulation and lipase production of R. delemar", Desalination and Water Treatment", vol. 53, no. 13, pp. 3543-3556, 2015.

[17] F. Jamil Emon, M. F. Rohani, N. Sumaiya, M. F. Tuj Jannat, Y. Akter, M. Shahjahan, Z. Abdul Kari, A. B. Tahiluddin, K. W. Goh, "Bioaccumulation and bioremediation of heavy metals in fishes-A review", Toxics, vol. 11, no. 6, 2023.

[18] A. Muhammed, A. Hussen, T. Kaneta, "Trace nickel analysis in water samples via paper-based devices coupled with co-precipitation", South African Journal of Chemistry, vol. 77, pp. 01-07, 2023.

[19] D. F. Boltz, Colorimetric Methods of Analysis., Including Photometric Methods vol. 2A, Princeton: N.J, 1959.

[20] L. Rosso, J. R. Lobry, S. Bajard, J. P. Flandrois, "Convenient model to describe the combined effects of temperature and pH on microbial growth", Applied and Environmental Microbiology, vol. 61, no. 2, pp. 610-616, 1995.

[21] J. M. Gonzalez, B. Aranda, "Microbial growth under limiting conditions-future perspectives", Microorganisms, vol. 11, no.7, 2023.

[22] Ü. Açıkel, M. Erşan, "Investigation of inhibition kinetics of Zn(II) Ions on the acid phosphatase activity and growth of R. delemar and Zn(II) bioaccumulation", Desalination and Water Treatment, vol. 57, no. 8, pp. 3689-3699, 2016.

[23] F. Huang, C.L. Guo, G. N. Lu, X. Y. Yi, L. D. Zhu, Z. Dang, "Bioaccumulation characterization of cadmium by growing Bacillus cereus RC-1 and its mechanism", Chemosphere, vol. 109, pp. 134-142, 2014.

[24] A. Paul, T. R. Stösser, A. Zehl, E. Zwirnmann, R. D. Vogt, C. E. W. Steinberg, "Nature and abundance of organic radicals in natural organic matter: Effect of pH and irradiation", Environmental Science & Technology, vol. 40, no. 19, pp. 5897-5903, 2006.

[25] A. Matin, "pH homeostasis in acidophiles", Novartis Found Symp, vol. 221, pp. 152-166, 1999.

[26] C. M. Bethke, R. A. Sanford, M. F. Kirk, Q. Jin, T. M. Flynn, "The thermodynamic ladder in geomicrobiology", American Journal of Science, vol. 311, no. 3, pp. 183-210, 2011.

[27] C. Abourached, T. Catal, H. Liu," Efficacy of single-chamber microbial fuel cells for removal of cadmium and zinc with simultaneous electricity production", Water Research, vol. 51, pp. 228-233, 2014.

[28] V. Kumar, S. K. Dwivedi, "Mycoremediation of heavy metals: processes, mechanisms, and affecting factors", Environmental Science and Pollution Research, vol. 28, pp. 10375–10412, 2021.

[29] S. Zhang, H. Jiang, S. Xue, N. Ge, Y. Sun, Z. Chi, G. Liu, Z. Chi, "Efficient conversion of cane molasses into fructooligosaccharides by a glucose derepression mutant of aureobasidium melanogenum with high β-fructofuranosidase activity", Journal of Agricultural and Food Chemistry, vol. 67, no. 49, pp. 13665-13672, 2019.

[30] S. Pattanakittivorakul, N. Lertwattanasakul, M. Yamada, S. Limtong, "Selection of thermotolerant Saccharomyces cerevisiae for high temperature ethanol production from molasses and increasing ethanol production by strain improvement", International Journal of General and Molecular Microbiology, vol. 112, no. 7, pp. 975-990, 2019.

[31] G. Y. Yew, B. K. Puah, K. W. Chew, S. Y. Teng, P. L. Show, T. H. P. Nguyen, "Chlorella vulgaris FSP-E cultivation in waste molasses: Photo-to-property estimation by artificial intelligence", Chemical Engineering Journal, vol. 402, 2020.

[32] G. Mersin, Ü. Açıkel, "Production of Candida biomasses for heavy metal removal from wastewaters", Trakya University Journal of Natural Sciences, vol. 22, no. 1, pp. 67-76, 2020.

[33] X. Zi, Y. Liu, T. Chen, M. Li, H. Zhou, J. Tang, "Effects of sucrose, glucose and molasses on fermentation quality and bacterial community of stylo silage", Fermentation, vol. 8, no. 5, 2022.

[34] Z. Aksu, G. Dönmez, "The use of molasses in copper(II) containing wastewaters: Effects on growth and copper(II) bioaccumulation properties of Kluyveromyces marxianus", Process Biochemistry, vol. 36, no.5, pp. 451-458, 2000.

[35] Z. Aksu, G. Dönmez, "Combined effects of molasses sucrose and reactive dye on the growth and dye bioaccumulation properties of Candida tropicalis", Process Biochemistry, vol. 40, no.7, pp. 2443-2454, 2005.

[36] W. R. Sadler, P. A. Trudinger, "The inhibition of microorganisms by heavy metals", Mineralium Deposita, vol. 2, pp. 158-168, 1967.

[37] Ü. Açikel, T. Alp, "A study on the inhibition kinetics of bioaccumulation of Cu(II) and Ni(II) ions using Rhizopus delemar", Journal of Hazardous Materials, vol. 168, no. 2–3, pp.1449-1458, 2009.

[38] A. Y. Dursun, G. Uslu, Y. Cuci, Z. Aksu, "Bioaccumulation of copper(II), lead(II) and chromium(VI) by growing Aspergillus niger", Process Biochemistry, vol. 38, no. 12, pp. 1647-1651, 2003.

[39] Ü. Açikel, M. Erşan, "Acid phosphatase production by Rhizopus delemar: A role played in the Ni(II) bioaccumulation process", Journal of Hazardous Materials, vol. 184, no. 1-3, pp. 632-639, 2010.

[40] A. Naskar, R. Majumder, M. Goswami, "Bioaccumulation of Ni(II) on growing

cells of Bacillus sp.: Response surface modeling and mechanistic insight", Environmental Technology & Innovation, vol. 20, 2020.

[41] M. Zhu, X. Feng, G. Qiu, J. Feng, L. Zhang, P. C. Brookes, J. Xu, Y. He, "Synchronous response in methanogenesis and anaerobic degradation of pentachlorophenol in flooded soil", Journal of Hazardous Materials, vol. 374, pp. 258-266, 2019.

[42] T. M. Roane, I. L. Pepper, T. J. Gentry, Microorganisms and Metal Pollutants, in: Environmental Microbiology, 3rd. ed. Academic Press, Elsevier, 2015.

[43] T. R. Sandrin, R. M. Maier, "Impact of metals on the biodegradation of organic pollutants", Environmental Health Perspectives, vol. 111, no. 8, pp. 1093-1101, 2003.

[44] Q. Lu, X. Zou, J. Liu, Z. Liang, H. Shim, R. Qiu, S. Wang, "Inhibitory effects of metal ions on reductive dechlorination of polychlorinated biphenyls and perchloroethene in distinct organohalide-respiring bacteria", Environment International, vol. 135, 2020.

[45] C. Li, W. Jiang, N. Ma, Y. Zhu, X. Dong, D. Wang, X. Meng, Y. Xu, "Bioaccumulation of cadmium by growing Zygosaccharomyces rouxii and Saccharomyces cerevisiae", Bioresource Technology, vol. 155, pp.116-121, 2014.

[46] A. M. Stanescu, L. Stoica, C. Constantin, I. Lacatusu, O. Oprea, F. Miculescu, "Physicochemical characterization and use of heat pretreated commercial instant dry baker's yeast as a potential biosorbent for Cu(II) removal", Clean-Soil, Air, Water, vol. 42, no. 11, pp. 1632-1641, 2014.

[47] F. Mohamadhasani, M. Rahimi, "Growth response and mycoremediation of heavy metals by fungus Pleurotus sp.", Scientific Reports, vol. 12, 2022.

Sakarya Üniversitesi Fen Bilimleri Dergisi
Sakarya University Journal of Science

e-ISSN : 2147-835X
Publisher : Sakarya University

Vol. 29, No. 2, 218-225, 2025
DOI: https://doi.org/10.16984/saufenbilder.1414507

Research Article

Densification of CuO-ZrO_2 Nanocomposites by Flash Sintering

Zeynep Çetinkaya[1-2]

[1] Konya Technical University, Department of Metallurgical and Materials Engineering, Konya, Türkiye, zcetinkaya@ktun.edu.tr, ror.org/02s82rs08
[2] University of Colorado Boulder, Department of Mechanical Engineering, Materials Science and Engineering, Boulder, CO, USA, zeynep.cetinkaya@colorado.edu, ror.org/02ttsq026

ARTICLE INFO

Keywords:
CuO/ZrO_2
Conventional sintering
Flash sintering
Hydrothermal synthesis
Nanocomposites

Article History:
Received: 04.01.2024
Revised: 18.02.2025
Accepted: 27.03.2025
Online Available: 15.04.2025

ABSTRACT

This study is a comprehensive investigation into CuO-doped ZrO_2 nanoparticles (NPs) produced by the hydrothermal method and its conventional (CS) and flash-sintering (FS) processes. Besides this production, the effect of the differences in sintering techniques and density was investigated to prove the results. However, to the authors' knowledge, the FS of CuO/ZrO_2 nanocomposite (NC) material has yet to be studied, which is *the first report* on this material. The CuO/ZrO_2 nanocomposite particle (NCP) pellet was sintered at 1250 °C for 1 hour using CS. The other sintering method is FS, which obtains highly dense NCs. The CuO/ZrO_2 NCPs pellet was successfully produced with the lower sintering temperature (673 °C) and duration (60 seconds) by FS under a current density of 50 mA/mm^2, and electric field (100 V/cm). The microstructure and density of the pellets produced from CS and FS experiments were evaluated. The SEM results showed that the CuO/ZrO_2 NCPs with the FS experiment were successfully performed, and density results with 4.38 g/cm^3 proved this success compared to CS pellet density (3.72 g/cm^3). The FS process for CuO/ZrO_2 NCPs consumes ~ 2.2 kJ (0.227 kJ/cm^3), whereas CS samples require ~ 13 kJ (54 kJ/cm^3), making FS approximately six times more energy-efficient. This significant reduction in energy consumption highlights FS as a promising method for future applications focused on carbon emission reduction and energy efficiency.

1. Introduction

Copper and its alloys are ideal candidates due to their excellent thermal and electrical conductivity. Despite these properties, copper exhibits low wear resistance and limited strength. To improve such properties, ceramics are added to the metal composition to produce materials with a new composition and properties. In the literature, these materials with metal-ceramic combinations are called metal-doped composites. Metal-doped materials are widely used in high-performing aerospace, defense, and automotive applications. Since these materials can be found in many variations due to their structure, they can be combined with excellent thermal stability and mechanical properties. Additionally, materials with high electrical and thermal conductivity can be produced for use in various applications [1, 2].

Recently, scientists have investigated various material compositions by enhancing their properties using CuO-doped ceramics with materials such as ZrO_2, Al_2O_3, TiB_2, SiO_2, and graphene [3-5]. This approach has led to extensive research on CuO-doped ZrO_2 ceramics, demonstrating excellent mechanical and physical properties [2, 6-8].

Zirconium dioxide (ZrO_2) is well-known for its high thermal stability, mechanical strength, and excellent ionic conductivity in terms of hardness, photocatalytic degradation, and wear resistance. When doped with materials such as copper, cerium, or yttrium, the properties of zirconia can be further enhanced, resulting in improved structural characteristics and thermal properties.

Cite as: Z. Çetinkaya (2025). Densification of CuO-ZrO2 Nanocomposites by Flash Sintering, *Sakarya University Journal of Science*, 29(2), 218-225. https://doi.org/10.16984/saufenbilder.1414507

This doping process increases the material's resistance to deformation and enhances its overall stability under extreme conditions. These combined properties make ZrO_2 a critical component in various industrial applications, including fuel cell technology and advanced ceramics [9].

CuO/ZrO_2 NCPs have drawn significant attention due to their enhanced functional properties and the broad range of applications [10]. These NCs combine the catalytic efficiency of CuO with the robust structural and thermal properties of ZrO_2. The CuO/ZrO_2 NCPs are notably used in catalysis for reactions such as the benzylation of benzene, where they demonstrate higher catalytic efficiency than individual CuO or ZrO_2 catalysts. This increased efficiency is attributed to the synergistic interactions between CuO and ZrO_2, leading to improved dispersion of active sites and greater stability under reaction conditions [11, 12]. Furthermore, these NCPs are utilized in environmental applications such as the electrochemical reduction of CO_2 to ethylene, demonstrating high faradaic efficiency and current density, which are critical for sustainable energy solutions. The unique properties of CuO/ZrO_2 NCPs make them valuable in various fields, including energy storage, environmental remediation, and catalysts in chemical synthesis and industrial processes [12].

The literature indicates that mechanical alloying [1, 2], hydrothermal processes [13], sol-gel methods [14], and electrospinning [13, 15, 16] can be used to prepare metal-doped composites. After these production methods, powders are compacted and sintered. Sintering has been conducted in various ways over the last decade, including CS, microwave sintering [4], spark plasma sintering (SPS) [17], and FS [16]. Using these sintering techniques CuO/ZrO_2 NCPs can be used in various applications, including photocatalytic degradation, wear resistance, and improvement of electrical conductivity. Despite the use of other ceramic materials to enhance the properties of ZrO_2, research on integrating a very fine grain structure into CuO and exploring its physical, microstructural, and sintering techniques remains limited.
This study investigated the effect of CS and FS on the microstructures and densities of CuO/ZrO_2 NCPs produced by the hydrothermal method in a 1:1 weight ratio, providing insights for future research. CS of CuO/ZrO_2 NCPs requires several hours at 1200 to 1500°C to achieve full density [18]. However, FS offers a mechanism for achieving similar results at lower temperatures in shorter periods. Additionally, a comparison of FS and CS effects on CuO/ZrO_2 NC microstructures and density has not yet been reported. To the best of the authors' knowledge, this study is the first report to explore this comparison of the CuO/ZrO_2 NCPs densification.

2.2. Materials And Methods

2.1. Materials

Zirconium (IV) nitrate pentahydrate ($Zr(NO_3)_4.5H_2O$, China) and sodium oleate (NaOL, $CH_3(CH_2)_7CH$, China) were used for the production of ZrO_2 NPs. Urea ($Co(NH_2)_2$, Sigma Aldrich) and copper (II) nitrate hydrate ($Cu(NO_3)_2.2.5H_2O$, Sigma Aldrich) were purchased for the production of the CuO particles. Ammonia was purchased to adjust pH and used for synthesizing both particles. Distilled water was utilized for hydrothermal synthesis.

2.2. Synthesis of CuO/ZrO_2 NCPs

In the previous study, CuO/ZrO_2 NCPs were produced by hydrothermal synthesis [15]. Briefly, this synthesis has two steps and is schemed in Figure 1. First, in two separate beakers, $Zr(NO_3)_4.5H_2O$ (metal source) was dissolved in 30 ml and NaOL (surfactant) in 15 ml of water mixed in a 1/2 volume ratio for 10 minutes at room temperature. The solution pH was adjusted to 9.4 with NH_3, and the white precipitate became homogeneous. Then, in two separate beakers, 0.1 M $Cu(NO_3)_2.2.5H_2O$, and urea were dissolved in 50 ml of water and stirred for 15 minutes. After mixing solutions, the pH was adjusted to 9.4. The two solutions were stirred in a 1/1 volume ratio for 10 minutes. The final solution was transferred to the hydrothermal unit at room temperature and heated at 200 ^oC for 13 hours. In the second step of this process, after 13 hours at 200 °C, the autoclave was cooled down to room temperature. Black precipitation was washed with water, ethanol, and acetone and

heat-treated at 600 ºC for 3 hours. Additionally, each NP (ZrO_2 and CuO) solution can be prepared individually using the same procedure.

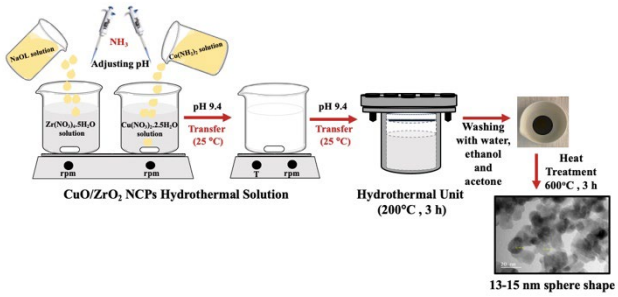

Figure 1. Scheme of the synthesis of the CuO/ZrO_2 NCPs

2.3. Preparation of the CuO/ZrO_2 NCPs pellets

The CuO/ZrO_2 NCPs were pressed using a uniaxial press (Hidroliksan, 2013) to make identical pellets under 50 bar pressure. The pellet-type stainless steel die has a 13 mm diameter and 2 mm thickness. These green-density pellet samples of the CuO/ZrO_2 NCPs were prepared and used in the CS and FS stages.

2.4. CS and FS methods

One of these samples was prepared for the CS. CS was performed for 1 hour in a furnace (Protherm, PLF 130/10) heated to 1250 °C with a heating rate of 3 °C /min.

A power source (Ametek, XG600-2.6) was used for the FS experiment to apply the DC electric field with the current control system. The maximum current was applied from the DC power source. The computer-aided system recorded the electric field and current flow (Fig. 2). The pellet was positioned in a parallel plate capacitor experimental setup, a sandwich form for FS. The FS setup details have been mentioned frequently in our previous studies [16, 19-21]. The pellet was placed, and the wires were attached to the power source. A quartz glass window settled on the front of the furnace to record the FS experiment.

The FS experiment furnace was programmed to increase the temperature to 800 °C with a heating rate of 15 °C /minute. When the flash started, the furnace temperature paused and was kept at that temperature. The graph was plotted using data obtained just before the flash started. (The data collected until the furnace temperature reached 673 °C were not included in the graph). The power supply (DC) generates an electric field of chosen voltages to trigger the flash of the CuO/ZrO_2 NCPs pellet. With the previous experience, the cut-off value was 50 mA/mm^2 to minimize joule heating and avoid thermal runaway. Thanks to the current draw by the pellet would lead to joule heating, the internal temperature of the pellet was increased over the furnace temperature. This study has determined the current cut-off and electric field values.

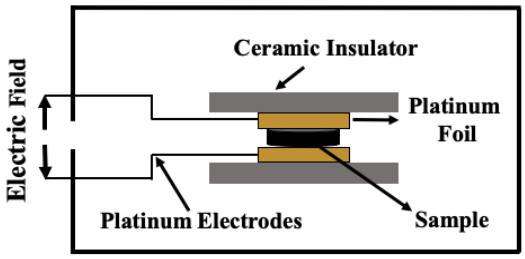

Figure 1. Parallel plate capacitor type of FS experiment setup [19]

2.5. Characterization

After the CS and FS experiments, the first phase structure was checked from the X-ray diffraction analysis (XRD, Europe 600 Benchtop XRD Instrument, Cu-Kα, λ=1.54 Å) in the range of 10-100° and the scanning speed was 2 °/min. Then, the morphology of the before-sintering (green) CuO/ZrO_2 NCP sample was examined by transmission electron microscopy (TEM, JEOL-JEM 2100). Using scanning electron microscopy (SEM, Zeiss LS- 10) equipped with an energy dispersive X-ray spectroscopy (EDX) analysis was conducted on a gold-coated cross-sectional area of the CuO/ZrO_2 NCPs pellet sample for the study of the after CS and FS experiment microstructures. After that, green, CS, and FS sample densities were measured using the Archimedes method.

3. Results and Discussion

The XRD pattern of the CuO/ZrO_2 NCPs after heat treatment at 600 °C is presented in Figure 3. It is proven that, after heat treatment, a mixture of CuO and ZrO_2 was achieved. The CuO and ZrO_2 phases remain unchanged. The previous

study showed that ZrO_2 peaks have broader intensity values than CuO peaks and ZrO_2 NPs are smaller than CuO particles [15].

The ZrO_2 and CuO-doped ZrO_2 NCPs crystallite sizes were determined to be 8.8 and 12.3 nm by the Debye-Scherrer formula, respectively.

$$D = (k\,\lambda)/\beta\cos\theta \quad (1)$$

In this equation, where D is the grain size, λ is the wavelength of X-ray diffraction (λ= 1.5404 Å), K= 0.9 which is the correction factor, β is FWHM of the most intense diffraction factor (calculated with Origin software), and θ is the Bragg angle.

The shape and size of the CuO/ZrO_2 NCPs were investigated by TEM (Fig. 4), which are illustrated to be spherical-shaped, with a particle size of between 13-15 nm. This production method produces smaller particles than other methods, such as mechanical alloying [5].

Fine particles are good for forming composites because they have suitable dislocation for movement barriers and can be uniformly dispersed at inter-particle boundaries [22]. Similarly, spherical-shaped ceramic particles resulted in better bonding than irregular ones for Cu/ZrO_2 composites [13, 14].

The high-resolution transmission electron microscopy (HR-TEM) inset in Fig. 4 reveals that a spherical shape and 14.6 nm maximum particle size were produced with this NCP procedure. Furthermore, the inset of Fig. 4 exhibits that the interplanar spaces are uniform and 1.3 Å.

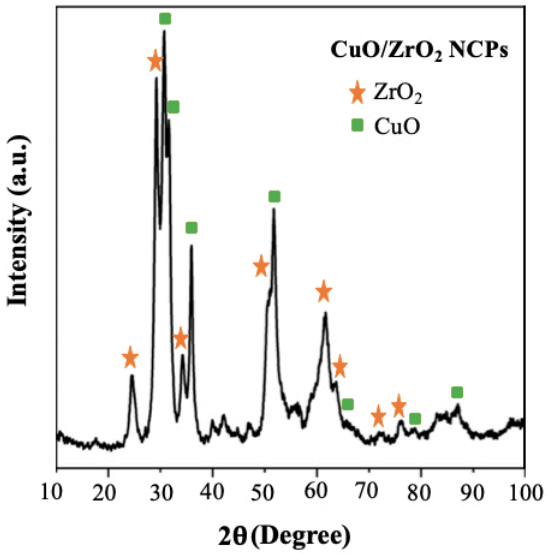

Figure 3. XRD pattern of the as-synthesis of the CuO/ZrO_2 NCPs

The 100 V/cm electric fields were applied to the CuO/ZrO_2 NCPs pellet in a parallel plate capacitor geometry. The current was kept constant at 50 mA/mm^2 to be sure the current density was not exceeded. The sample was heated to 800 °C with a 15 °C /min heating rate. The current-voltage data was recorded as a function of time.

The electric field-assisted system is described in three stages. Stage I is incubation, Stage II is the transition stage, and Stage III is the steady state. Stage I shows no current draws until flash starts and Stage II shows the current's cut-off value. At Stage III, the current control of the power supply is maintained (Fig. 5).

CuO/ZrO_2 NCP pellet under the 100 V/cm applied field showed no current draw until the furnace reached 670 °C (Stage I). At the end of Stage I, the sample showed insulator behavior (between 25 °C and 670 °C). The current leakage was detected as 1.6 mA/mm^2 during this stage. When the furnace reached 673 °C, the current had a maximum point of 50 mA/mm^2, and the electric field decreased to 40 V/cm. As the flash began 673 °C, the furnace temperature was paused and maintained at a constant level. This allowed for the measurement of the sample temperature during the flash process. In the graph part of the incubation stage was shown and finished in less than 28 seconds.

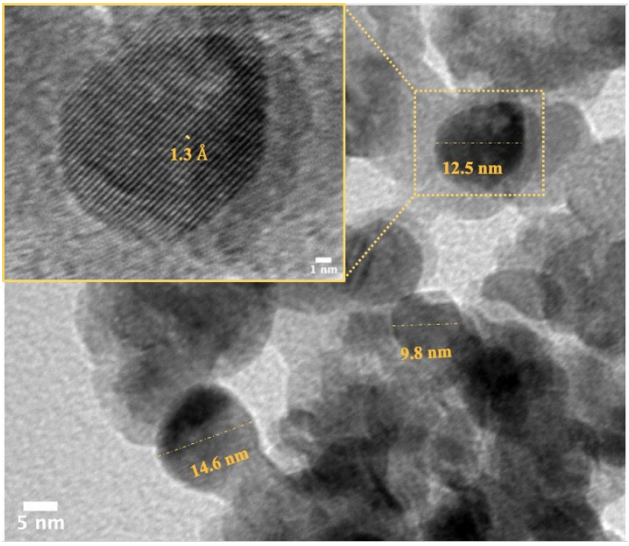

Figure 4. TEM images of the CuO/ZrO_2 NCPs (the inset on the left side of the figure presents the magnification of the circled area)

At Stage II, the sample conductivity started to increase. Furthermore, the transition stage showed a rapid increase in the current draw at 673 °C. The DC power source was changed from voltage control to a current control system to avoid excessive Joule heating. At that time, the sample had a maximum power absorption at this stage of the FS. After the flash, the sample temperature reached at 773 °C in 15 seconds. Overpower absorption could lead to high Joule heating, causing abnormal grain growth, which is not recommended. The Stage III of this experiment is to retain the current control of the power supply. The power source shut down within 30 seconds when the current density was stabilized. FS (Stage II), spanning 15-20 seconds during Stage III, is believed to be part of the FS process.

The FS experiment was completed in 60 seconds with three stages. In the literature, at least 1 hour of production time at 1250 °C is required for the CS process in CuO/ZrO_2 NCPs [23]. The method used in this study reduced the sintering temperature by 577 °C and the sintering time to 60 seconds with electric field assisted/FS.

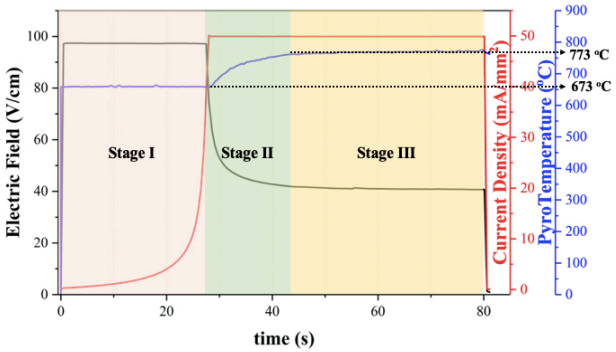

Figure 5. FS experiment of CuO/ZrO_2 NCPs under 100 V/cm electric field at 673 °C furnace temperature

The FS energy consumption of the CuO/ZrO_2 NCPs is approximately 2.2 kJ, corresponding to an energy density consumption of 0.227 kJ/cm³. In contrast, CS samples in the same furnace consume around 13 kJ per unit, which corresponds to an energy density consumption of 54 kJ/cm³. Thus, the energy consumption of the flash-sintered sample was approximately six times lower than that of the sample sintered using the conventional method. The FS method shows promise for producing CuO/ZrO_2 NCPs in future applications, particularly concerning carbon emission reduction and energy saving.

Figure 6 represents the microstructure morphology of the conventional and flash-sintered samples taken from the cross-sectional area. SEM micrographs taken from the cross-sectional area of the CuO/ZrO_2 NCPs material for CS are shown in Figure 6a.

The orange dashed area inset of Fig. 6a was given as the magnified area of the selected. Besides, Figs. 6c and 6d show the elemental mapping of the orange dashed line area in Figs. 6a and 6b, respectively. Furthermore, the EDX spectrum in Figs. 6c and 6d reveal that the sample comprises Cu, Zr, and O elements. Fig. 6a observes that the intergranular boundaries do not disappear with CS, and the sintering process does not take place sufficiently. The microstructure shows the formation of a less porous, high-density structure, confirming the density measurement with the FS pellet (Fig. 6b). After the sample was brought to room temperature, the density was measured according to Archimedes' principle.
The density for the green, conventional, and flash-sintered samples was measured as 2.92, 3.72, and 4.38 g/cm^3, respectively. FS has been

demonstrated to decrease grain size, resulting in a higher density compared to samples sintered using conventional methods. Moreover, with this value, it was proven that the sintering process obtained from the SEM micrograph was successful and convenient. These values were very reasonable compared to the literature [1-3, 22].

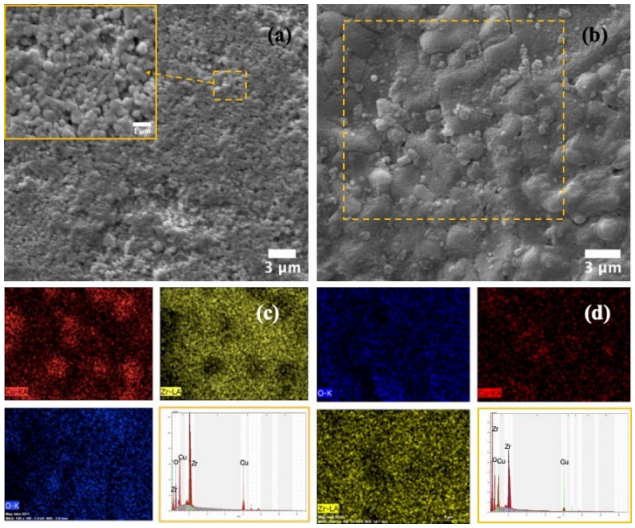

Figure 6. SEM micrograph of a) conventional, b) flash-sintered CuO/ZrO_2 NCPs and EDS and EDX analysis of c) CS and d) FS sample selected areas

4. Conclusion

This study was compared with an applied electric field-assisted/FS and CS technique to obtain highly dense CuO/ZrO_2 NCPs. The best authors' knowledge from the literature, FS of CuO/ZrO_2 NCP material has yet to be studied. Thus, this study is *the first report* on this material using the FS method.

The CuO/ZrO_2 NCP pellet sample was exposed to an electric field of 100 V/cm with a current density of 50 mA/mm^2, and no current draw was recorded in the experimental system. The maximum current density was achieved at 673 °C, and the power supply was self-regulated by the electric field-current relationship. Furthermore, in the flash experiment, the system measured the sample temperature of ~737 °C.

The CS of the CuO/ZrO_2 NCPs pellet was sintered at 1250 °C for 1 hour. The density of the green, CS, and FS of the CuO/ZrO_2 NCPs samples was measured by the Archimedes method as 2.92, 3.72, and 4.38 g/cm^3, respectively. In light of the SEM micrographs, the grain boundaries cannot disappear with CS. However, the FS experiments allow for obtaining denser microstructures than those obtained with CS. The density results of the CS and FS pellets confirmed the SEM micrograph images. This experimental procedure reduced the sintering temperature by 577 °C and the processing time from 1 hour to 60 seconds for producing products with CuO/ZrO_2 NCPs at lower temperatures and resulted in a denser structure. The FS process significantly reduces energy consumption, requiring about six times less energy than the CS method. This makes FS a promising technique for producing CuO/ZrO_2 NCPs, especially in applications where reducing carbon emissions and energy saving are the priorities.

Article Information Form

Acknowledgments
The author would like to thank TUBITAK 2219-International Postdoctoral Research Fellowship Program for supporting her research at the University of Colorado at Boulder.

Funding
The author gratefully acknowledges the financial support provided by the Scientific Research Projects Coordination Unit of Konya Technical University (Contract # BAP- 211019030) for the examining the samples.

The Declaration of Conflict of Interest/ Common Interest
No conflict of interest or common interest has been declared by the author.

The Declaration of Ethics Committee Approval
This study does not require ethics committee permission or any special permission.

The Declaration of Research and Publication Ethics
The author of the paper declare that they comply with the scientific, ethical and quotation rules of SAUJS in all processes of the paper and that they do not make any falsification on the data collected. In addition, they declare that Sakarya University Journal of Science and its editorial board have no responsibility for any ethical violations that may be encountered, and that this study has not been evaluated in any academic

publication environment other than Sakarya University Journal of Science.

References

[1] A. Fathy, O. Elkady, A. Abu-Oqail, "Production and properties of Cu-ZrO_2 nanocomposites," Journal of Composite Materials, vol. 52, no. 11, pp. 1519–1529, 2018.

[2] Y. Sakka, T. S. Suzuki, K. Ozawa, T. Uchikoshi, K. Hiraga, "Sintering and ionic conductivity of CuO-doped tetragonal ZrO_2 prepared by novel colloidal processing," Journal of the Ceramic Society of Japan, vol. 109, no. 1276, pp. 1004–1009, 2001.

[3] A. Fathy, A. Wagih, A. Abu-Oqail, "Effect of ZrO_2 content on properties of Cu-ZrO_2 nanocomposites synthesized by optimized high energy ball milling," Ceramics International, vol. 45, no. 2, pp. 2319–2329, 2019.

[4] P. S. Selvamani, J. Judith Vijaya, L. John Kennedy, A. Mustafa, M. Bououdina, P. Joice Sophia, R. Jothi Ramalingam, "Synergic effect of Cu_2O/MoS_2/rGO for the sonophotocatalytic degradation of tetracycline and ciprofloxacin antibiotics," Ceramics International, vol. 47, no. 3, pp. 4226–4237, 2021.

[5] Y. A. Sorkhe, H. Aghajani, A. Taghizadeh Tabrizi, "Mechanical alloying and sintering of nanostructured TiO_2 reinforced copper composite and its characterization," Materials & Design, vol. 58, pp. 168–174, 2014.

[6] M. K. G. Abbas, S. Ramesh, K. Y. Sara Lee, Y. H. Wong, C. Y. Tan, U. Johnson Alengaram, P. Ganesan, F. Musharavati, and E. Zalnezhad "Densification of copper oxide doped alumina toughened zirconia by conventional sintering," Ceramics International, vol. 48, no. 5, pp. 6287–6293, 2022.

[7] S. Azhar, K. S. Ahmad, I. Abrahams, W. Lin, R. K. Gupta, A. El-marghany, "Synthesis of phyto-mediated CuO–ZrO_2 nanocomposite and investigation of their role as electrode material for supercapacitor and water splitting studies," Journal of Materials Research, vol. 22, pp. 4937–4950, 2023.

[8] M. Shojaei, A. Hasani, Z. Amiri, G. R. Khayati, "Using the group method for the synthesis of copper/ZrO_2 nanocomposites to achieve high wear resistance by ball milling and spark plasma sintering," Ceramics International, vol. 48, no. 12, pp. 17576–17588, 2022.

[9] S. G. Giniyatova, N. A. Sailaukhanov, E. Nesterov, M. V. Zdorovets, A. L. Kozlovskiy, D. I. Shlimas, "Research of Structural, Strength and Thermal Properties of ZrO_2-CeO_2 Ceramics Doped with Yttrium," Crystals, vol. 12, no. 2, p. 242, 2022.

[10] A. H. Shukor, H. A. Alhattab, I. Takano, "Electrical and optical properties of copper oxide thin films prepared by DC magnetron sputtering," Journal of Vacuum Science & Technology B, vol. 38, no. 1, p. 012803, 2019.

[11] S. N. Basahel, M. Mokhtar, E. H. Alsharaeh, T. T. Ali, H. A. Mahmoud, K. Narasimharao, "Physico-Chemical and Catalytic Properties of Mesoporous CuO-ZrO_2 Catalysts," Catalysts, vol. 6, no. 4, 2016.

[12] P.-P. Guo, Z.-H. He, S.-Y. Yang, W. Wang, K. Wang, C.-C. Li, Y.-*Y.* Wei, Z.-T. Liu, B. Han, "Electrocatalytic CO_2 reduction to ethylene over ZrO_2/Cu-Cu_2O catalysts in aqueous electrolytes," Green Chemistry, vol. 24, no. 4, pp. 1527–1533, 2022.

[13] İ. C. Kaya, Ç. Çetin, H. S. Aydın, M. S. Yavuz, B. Z. Büyükbekar, M. Uyaner, V.

Kalem, H. Akyıldız, "Production of $CuAlO_2$ in powder, bulk and nanofiber forms," Journal of Ceramic Processing Research, vol. 16, no. 5, pp. 648–655, 2015.

[14] J. Liu, J. Shi, D. He, Q. Zhang, X. Wu, Y. Liang, Q. Zhu "Surface active structure of ultra-fine Cu/ZrO_2 catalysts used for the CO_2+ H_2 to methanol reaction," Applied Catalysis A: General, vol. 218, no. 1–2, pp. 113–119, 2001.

[15] Z. Çetinkaya, "Production of CuO/ZrO_2 Nanocomposites in Powder and Fiber Forms," *KONJES*, vol. 12, no. 1, pp. 221–230, 2024.

[16] Z. Çetinkaya, E. Güneş, İ. Şavkliyildiz, "Investigation of biochemical properties of flash sintered ZrO_2–SnO_2 nanofibers," Materials Chemistry and Physics, vol. 293, p. 126900, 2023.

[17] J. Baneshi, M. Haghighi, N. Jodeiri, M. Abdollahifar, H. Ajamein, "Homogeneous precipitation synthesis of CuO–ZrO_2–CeO_2–Al_2O_3 nanocatalyst used in hydrogen production via methanol steam reforming for fuel cell applications," Energy Conversion and Management, vol. 87, pp. 928–937, 2014.

[18] Z. A. Hamid, "Composite and nanocomposite coatings," Journal of Metallurgical Engineering, vol. 3, no. 1, pp. 29–42, 2014.

[19] Z. Çetinkaya, "Flaş sinterleme yönteminin uçucu kül mikroyapısına etkisi," Journal of The Faculty of Engineering and Architechure of Gazi University, vol. 37, no. 1, pp. 137–144, 2021.

[20] Z. Çetinkaya, A. Gökhan, S. Dursun, İ. Şavkliyildiz, "Reusing blended leach residue by flash sintering method," International Journal of Applied Ceramic Technology, vol. 21, pp. 1567-1573, 2024.

[21] Z. Çetinkaya, "Investigation of Reusing Copper Converter Slag Residue with the Flash Sintering Method," JOM, vol. 75, no. 12, pp. 5361–5371, 2023.

[22] W. Li, H. Assadi, F. Gaertner, S. Yin, "A Review of Advanced Composite and Nanostructured Coatings by Solid-State Cold Spraying Process," Critical Reviews in Solid State and Materials Sciences, vol. 44, no. 2, pp. 109–156, 2019.

[23] M. Khaloobagheri, B. Janipour, N. Askari, E. Shafiee Kamal Abad, "Characterisation of powder metallurgy Cu-ZrO_2 composites," Advances in Production Engineering And Management, pp. 242–248, 2013.

Sakarya Üniversitesi Fen Bilimleri Dergisi
Sakarya University Journal of Science

e-ISSN : 2147-835X
Publisher : Sakarya University

Vol. 29, No. 2, 226-239, 2025
DOI: https://doi.org/10.16984/saufenbilder.1585752

Research Article

A New Risk Assessment Methodology Based on Control Limits

Müfide Narlı[1*], Şeyda Taşkınırmak[2] Cansu Dağsuyu[2], Ali Kokangül[1]

[1] Cukurova University, Faculty of Engineering, Department of Industrial Engineering, Adana, Türkiye, mnarli@cu.edu.tr, kokangul@cu.edu.tr, ror.org/05wxkj555
[2] Alparslan Türkeş Science and Technology University, Faculty of Engineering, Department of Industrial Engineering, Adana, Türkiye, scelikcan@atu.edu.tr, cdagsuyu@atu.edu.tr
*Corresponding Author

ARTICLE INFO

Keywords:
Operating room
Risk analysis
FMEA
Control limits

Article History:
Received: 15.11.2024
Revised: 03.02.2025
Accepted: 12.03.2025
Online Available: 18.04.2025

ABSTRACT

Operating rooms where surgical procedures are conducted involve hazards under various groups and potentially many health problems may arise from these hazards. The degree of the importance of the hazard in each risk group varies according to the groups and it is important to reflect this situation in the risk analyses. In the present study, the dangers may occur in the main groups, namely physical, chemical, and psychological hazard groups in the operating rooms, and the potential health problems that may result from these hazards were evaluated with Failure Mode Effect Analysis (FMEA) method for the first time. By taking the distribution of the FMEA values about the health problems due to hazards that may occur in each main group into consideration, a new approach is suggested in this study. With the new scale that is created based on the average and standard deviation of FMEA values, the comparative importance of the hazards within their groups was revealed. Thus, considering the comparative evaluations, the degrees of importance for health problems in terms of physical, chemical, psychological, and biological categorization were put forth. The COVID-19 outbreak caused a pandemic in the world was also considered in the biological risk class in the study. At the end of the study, the most critical health problems in the operating rooms were detected to be from the risk group resulting from chemical conditions.

1. Introduction

The healthcare industry is one of the fields where employees are faced with a high degree of physical and psychological tension due to the broadness and complexity of its activity area [1-3]. Because the patients, illnesses, and the rate at which the illnesses spread are ever-increasing, healthcare services and safety have been gradually gaining importance. The mistakes that may occur in the healthcare industry can easily jeopardize both the employee's and the patient's health. The risks that occur can cause serious results as well as small damages for those who are exposed to them. While providing healthcare services, these risks may cause injury to the patients, prolonged hospital stay, disability, and even death. These increase the risk of exposure to the health care problem for healthcare workers and lead to many problems for them such as injury.

Because the hazard factors creating risks in health services cause serious results, it is important to manage healthcare mistakes proactively [4]. According to the report entitled "To Err Is Human" prepared by the Institute of Medicine in 1999, 44000 – 98000 people lose their lives in the USA due to preventable medical mistakes every year. In the report, it is also stated that the deaths resulting from medical mistakes are greater in number than those caused by traffic accidents, lung cancer, and AIDS [5]. Surgical interventions constitute 52% of all patients presenting to the hospital [6]. This ratio displays the importance of operating rooms, where

Cite as: M. Narli, Ş. Taşkınırmak, C. Dağsuyu, A. Kokangül (2025). A New Risk Assessment Methodology Based on Control Limits, *Sakarya University Journal of Science*, 29(2), 226-239. https://doi.org/10.16984/saufenbilder.1585752

surgical interventions are conducted, in hospitals. Hence, it is important to determine the risks that may occur in healthcare institutions especially in operating rooms beforehand and to analyse them.

The risks that may occur in every unit in health institutions and their effect degrees are different from each other. Because the operating rooms where surgical procedures are carried out are used by many units, the risks that may occur in them may have an impact on the whole health institution. Prolonged working times depending on the time needed for the procedures make the operating room a critical unit.

In recent years, technological evolution has played an important role also in the development of surgery. This brings about important changes in the working conditions of the operating room. An increased number of complex devices leads to an increase in the interactions between people and technology [7]. Surgical operations are a key health service constituting 40% of the expenditures of the hospital [8]. In addition to this, hospital and operating room directors should determine preventive precautions for hazards that may create danger in the operating room to decrease the probability of risks that occur depending on the infrastructure-materials, experience, education and the services given and to eliminate them.

The hazards that may occur in the operating room are evaluated under three main headings in general, namely physical, chemical, and psychological hazards. The hazards that may occur in the operating rooms where the hazards are more effective on hospital workers cause temporary and permanent health problems for employees. Furthermore, it is stated that the gradual increase in the high cognitive and physical workloads of the workers may even affect the career life of the workers [2]. Thus, the hazards should be analysed by taking the health problems caused by them and their levels of importance into consideration. These analyses would also be effective in determining the precautions to be taken.
The studies in the literature have investigated the risks that may occur in the operating room, the results of these risks, and health care problem. Pan et al. (2018), have studied the risk factors of the infections associated with the operating room after coronary artery bypass grafting [9]. They detected that factor such as the operation durations exceeding four hours, guests in the operating room, and the successive use posed a high risk. When Sheikhzadeh et. (2009) examined the ergonomic risk factors of the nurses and technicians in the surgical environment, they stated that the workers perceived the operating room as a demanding, stressful, and complex work environment and that they had tiring physical work activities resulting in problems of musculoskeletal system [1].

Some studies demonstrate that the conditions of the operating room cause long-term occupational healthcare problems for the workers. In the study conducted by El Ata et al. (2016), back pain was detected as the most prevalent problem amoung the nurses in the operating room with a ratio of 76.1% among the workers as a result of having to stand up for extended periods and repeated motions and this problem is followed by the problems of the knees, shoulders, and ankles as the most affected organs [10]. In the study carried out by Yu et al. (2016), working for 6 or more years, more than one-night shifts, working for 40 or more hours during the week, weak health status, and feeling of fatigue were found to be associated with musculoskeletal system injuries due to work [2]. It has been stated that nurses working night shifts were more inclined to exhaustion, emotional inconsistency, and emotional depletion and their feeling of personal achievement was lower. Some studies that evaluate the operating rooms ergonomically [3, 11].

Vos s et al. (2017) argued that the surgeons tried to optimize the working conditions which were not ergonomic and that they had to take a break frequently [11]. By examining the working conditions of the operating room in terms of ergonomic risk factors, and grouping them as physical, cognitive, and corporate ergonomic risk factors, Vural and Sutsunbuloğlu (2016), makes recommendations for the specified risks [3]. Matern and Koneczny (2007) state that general working positions were found to be uncomfortable or painful by 84% of the surgeons, that sunlight is insufficient in the

operating room environment, and that the air created a sense of dryness [7].

By examining the operating rooms in terms of air conditions, lighting, temperature, and oxygen status, the risks that may be caused by these factors were studied [12-15]. Ho et al. (2009) recommend a layout for supply grills for removal of the contaminating materials by simulating air conditions in the operating room [12]. In the study in which they evaluated the physical conditions of the operating rooms, Daskalakis et al. (2009), detected the temperature, moisture, ventilation, and light conditions to be more satisfactory while finding the air quality of the operating room insufficient [13]. Rinder (2008), stated that operating rooms had fire risks due to factors such as laser and oxygen use [14]. Culp et al. (2013), evaluated the ignition properties of the materials depending on the changing oxygen concentrations in the operating rooms [15]. They observed that the ignition time increased as the oxygen concentration decreased.

As seen in the literature the operating room consist of many risks and it is crucial to calculate their importance level them by using risk assessment techniques such as FMEA, Fine Kinney, AHP, etc. In the health sector, the use of FMEA is increasing due to the advantages it presents especially in the analysis and evaluation of the caused by people and medical devices [16]. Mosallanezhad (2018) handled the five basic processes, namely patient admission to the operating room transferring the patient, cleaning of the operating room, request for equipment repair in the operating room, and request for medical and pharmaceutical products in the operating room of a hospital, and analysed the risks that may occur by Fuzzy FMEA method [17]. Corrective precautions were recommended for the risks with RPN values over 4.

Khasha et al. (2013) used the Fuzzy FMEA method to determine the importance of investigating the factors that cause surgical cancellations [8]. As a result of this method, insufficient intensive care beds, high-risk intervention, high blood pressure, and diabetes patients were analysed as the most important factors causing surgical cancellations. Liu et al. (2014) proposed a 2-part hybrid-weighted method that considered the subjective and objective weights of risk factors and developed the classical FMEA method [18]. The proposed method was used in the blood transfusion study. Health risk analysis studies were examined which is different than the FMEA method [19-22].

Trucco and Cavallin (2006) proposed the “Clinical Risk and Error Analysis” method, which also takes into account the quantitative evaluation of critical organizational factors affecting patient safety [19]. The study was tested in drug applications in the vascular surgery department. Guo (2015) developed a risk management program based on Australian risk management standards in a hospital operating room in China [20]. The effects of risks were examined with the X-type matrix diagram for the 10 risk groups that were identified. Kasatpibal et al. (2016) examined the risk factors that cause blood-borne pathogenic diseases in operating room nurses using logistic regression analysis [21]. Pinhole and sharp blade injuries were found to be at high risk. Amghar et al. (2017) proposed a fuzzy Bayes network to identify and analyse operating room risks [22]. It has been demonstrated that factors such as the patient's age, physical condition, anaesthesia type, and wrong drug use have different effects on the patient's risk of death.

In the studies in the literature, the hazards that may come up in the operating rooms and their groups are studied. However, no risk analysis study comparing the importance levels of the hazards quantitatively was encountered in the literature review. In the present study, the risk groups that may occur in the operating room and the hazards that may come up in these groups were described and a risk analysis was done. The FMEA method recommended by the World Health Organization was preferred while conducting the risk analysis. The Joint Commission (JC), formerly called the Joint Commission on Accreditation of Health Care Organization (JCAHO), now requires all acute care hospitals to perform FMEA regularly [23]. The Technical Committee of the International Organization for Standardization (ISO) also suggests FMEA as a method for reducing high medical risks (ISO/TS 22367). In classical

FMEA studies, the risk score is determined according to the FMEA scale values but the change between the hazard groups and the hazards is not taken into consideration.

On the other hand, the risk score with the same value that may occur at different hazard dimensions (physical, chemical, psychological etc.) is expected to have different impacts. This situation was taken into consideration in the present study, and by considering the average and distribution values in the FMEA parameter values of the health problems that may occur in the main hazard sources in each hazard dimension, a new methodology was proposed. Thus, in the comparison of the scores of the health problems that may result from probable risks, the change in the hazard dimension would also be considered. In the proposed method, the total risk score, which was determined according to the average and distribution values of each hazard, was obtained and the hazard analysis was done precisely and comparatively. The rest of the study is organized as such: methodology is in Section 2; case study is in Section 3 and conclusion is in section 4.

2. General Methods

The method proposed in this study is based on the principle of considering the distributions in the groups by grouping the hazards. Risk analysis constitutes the first step of this method. Of the risk analysis methods, FMEA, which is commonly used in healthcare, was preferred. The FMEA method consists of Probability (P), severity (S) and detectability (D) parameters. The scale values for these parameters are given in

Table 1,2 and 3 respectively. This scale was determined by the Institute of Healthcare Improvement for Healthcare. The risk score according to the FMEA method is obtained by the multiplication of these three parameters as seen in Equation 1. The hazards that occur in real systems may be caused by different hazard sources and these hazards are categorized according to their sources. In the classical approach, when the hazards in different hazard sources have the same RPN value, this causes these hazards to be interpreted with equal importance. However, assessment of the hazards in the hazard source they belong to and their interpretation accordingly would be more effective in determining the importance levels of the hazards.

$$RPN = PxSxD \quad (1)$$

The approach developed as being based on the consideration of hazards consists of the following steps.

1. Description of the hazard sources
2. Determining the sub-hazards depending on the hazard sources or the health problems that may occur about to the hazard sources
3. Calculation of RPN values for each health problem based on hazards with Equation (1) by taking the scales in Table 1-3 into consideration.
4. Determining the control limits of P, S and D parameters (average (μ), standard deviation (σ), 2σ and 3σ values) based on of each hazard source(n)
5. Creating the scale table given in Table 4 according to the average and standard deviation values of each hazard

The FMEA scale consists of integer numbers. Thus, the limit values found in the scale table created according to the new approach are rounded to the nearest integer number. The limit values change according to the FMEA evaluation conducted. Although the lower limit's being smaller than 1 is not taken into consideration, the upper limit can be a maximum of 10.

Table 1. FMEA probability (P) scale [24]

Criteria/ risk	Rating	Description (Detection of failure)
None	1	Remote: failure is unlikely, one occurrence in greater than five years
Very Low	2	One occurrence every three to five years
Low	3	Low: relatively few failures, one occurrence every one to three years
Moderate	4	One occurrence per year
	5	One occurrence every six months to one year
	6	Moderate: occasional failures, one occurrence every three months
High	7	One occurrence every month
Very High	8	High: repeated failures, one occurrence per week
Extremely High	9	One occurrence every three to four days
Dangerously High	10	Failure is almost inevitable. More than one occurrence per day

Table 2. FMEA severity (S) scale [24]

Criteria/ risk	Rating	Description (Detection of failure)
None	1	No noticeable effects
Very Minor	2	Slight inconvenience at delivery; minor rework. Failure detected and corrected at delivery.
Minor	3	Slight inconvenience at next function; minor rework. Failure detected and corrected at next step of the process.
Very Low	4	Inconvenience at subsequent function; minor rework. Failure detected and corrected at subsequent step of the process.
Low	5	Inconvenience for patient and provider with failure being detected.
Moderate	6	Failure causes disruption of patient activities of daily living leading to dissatisfaction
High	7	Failure seriously affects patient's health leading to high patient dissatisfaction.
Very High	8	Failure causes patient's health to be seriously affected and patient has to return for major correction.
Extremely High	9	Failure involves regulatory noncompliance and could cause long term disability.
Dangerously high	10	Failure could cause terminal injury or death of the patient

Table 3. FMEA detection (d) scale [24]

Criteria/ risk	Rating	Description (Detection of failure)
Almost certain	1	Current controls almost certain to detect the failure mode. Reliable detection controls are known with similar processes. Process automatically prevents further processing.
Very High	2	Current controls almost certain to detect the failure mode. Process automatically detects failure mode.
High	3	Current controls almost certain to detect the failure mode. Process automatically detects failure mode.
Moderately High	4	Controls have a good chance of detecting failure mode. Error detection at service delivery.
Moderate	5	Controls may detect the existence of a failure mode. Error likely to be detected after service delivery.
Low	6	Controls may detect the failure.
Very Low	7	Controls have a low chance of detecting the existence of failure.
Remote	8	Controls have a poor chance of detecting the existence of failure mode.
Very Remote	9	Controls probably will not detect the existence of failure mode. Control achieved with indirect or random checks only.
Absolute Uncertainty	10	Controls will not or cannot detect the existence of a failure. No known controls available to detect failure mode.

If σ value is less than 1; for P, S, and D value in ($\mu, \mu+\sigma$) interval not to have a value less than the value in $(\mu-\sigma,\ \mu\ )$ interval, $1/\sigma$ value is considered as σ and this situation is reflected in Table 4. Also, since the upper limit value will not be greater than 10if the μ+3σ

value is greater than 10 for the P, S, and D values, this value is accepted as 10 and this situation is reflected in Table 4.

P, S, and D values for the hazard (i) in each hazard source (n) are determined according to the scale values found in Table 4 for P, S, and, D and the proposed RPN ($\boldsymbol{RPN_n}$) value is calculated with Equation (2).

$$\boldsymbol{RPN_{ni} = P_n * S_n * D_n} \quad \text{i=1,2,..m} \qquad (2)$$

By taking the sum of $\boldsymbol{RPN_n}$ values about a sub-hazard of each hazard group, the importance levels of the sub-hazards are determined.

$$\boldsymbol{Total\ RPN_n} = \sum_{i=1}^{m} \boldsymbol{RPN_{ni}} \qquad (3)$$

Table 4. Proposed scale method

Class	Limit Values		Scale value (P_n, S_n, D_n)
	Lower limit	Upper limit	
1	$\mu + 2\sigma$	if $(\mu + 3\sigma) \geq 10.10$ otherwise $\mu + 3\sigma$	3σ
2	$\mu + \sigma$	$\mu + 2\sigma$	2σ
3	μ	$\mu + \sigma$	σ
4	$\mu - \sigma$	μ	$if\ \ \sigma \geq 1.1/\ \sigma$ $otherwise\ \ \ \sigma$
5	$\mu - 2\sigma$	$\mu - \sigma$	$1/\ 2\sigma$
6	$if\ \ (\mu - 3\sigma) \leq 1.\ 1/\ \sigma$ $otherwise\ \ \ \sigma$	$\mu - 2\sigma$	$1/\ 3\sigma$

3. Case Study

The study was conducted out in a private hospital with a high bed capacity and operating room with different characteristics. The hazards that occur in the operating room were examined under 4 main headings, which are physical, chemical, psychological, and biological hazards. A description of the hazards that may occur under each main heading and the assessment of the health problems resulting from these hazards were carried out with the classical risk analysis approach and with the approach proposed in this study. The hazards were determined by literature review and by taking the operating room team. The risks taken from the literature are given in the tables together with their sources. Determining the hazards and their assessment were conducted in collaboration with the operating room team of a large-scale hospital.

i. Risk Analysis for Physical Conditions

The physical hazards that might take place in the operating room were gathered under three main headings noise, insufficient ventilation, and lighting by the literature and expert opinion. The health problems that may occur due to physical conditions such as hearing loss, cardiovascular disorder problems, etc. are given in Table 5. Risk analysis was done based on FMEA with Equation (1) according to the health problems caused by physical hazards and the results are given in Table 5. This risk analysis determined that the most important health problem for the noise hazard was "headache", the most important health problem caused by insufficient ventilation was "heat injury" and the most critical health problem occurring as a result of lighting hazard was "eye disorders". The "hearing loss" and "cardiovascular disorder" with 25 RPN values calculated by Equation (1) as a result of FMEA have the respective 3rd and 2nd importance levels in the hazard group they belong to. This situation necessitates the investigation of distributions in the hazard group when determining the RPN values. Thus, for each hazard group, value description was done according to distribution of P, S, and D values of FMEA parameters. P, S, and D values for each hazard group are given in Table 5.

The average and standard deviation values for these values were rounded to the nearest integer number and scale values for P, S, and D parameters according to Table 4 are given in Table 6, 7, and 8. It can be seen in Table 5 that although the rankings of the health problems in the hazard group do not change according to the classical RPN and the proposed RPNn, differences occur in the comparisons between hazards. Although "hearing loss" in the noise hazard group and "cardiovascular disorder" under the insufficient ventilation group possess equal importance in the classical assessment (RPN=25), the order of importance could be determined with the proposed method and it is seen in Table 5 that the "cardiovascular disorder" has a higher level of importance. Moreover, some hazards have a higher ranking in importance according to the proposed method despite having a lower RPN value. The "psychological disorder" in the noise hazard group has a higher RPN value than the "eye disorder" under lighting. But "eye disorder" has a higher importance level with the RPNn value where distribution in the hazard groups is taken into consideration. Thus, the level of importance for each health problem based on each hazard is determined and a more precise and

correct assessment is done. With Equation (3), the RPNn values of the health problems in each hazard group were added mathematically and the importance levels of the health problems were determined and given in Table 5. According to this evaluation, as seen in Table 5 the order of the health problems due to physical hazards in the operating room according to importance can be sequenced as "headache", "heat injury", "psychological disorder" and "cardiovascular disorder". However, the order of importance does not change for the health problems when the sum of the classical RPN values is taken into consideration. It is seen that the importance level of other health problems is examined. It can be seen in Table 5 that total prioritization can be made between health problems (hearing loss and cardiovascular disorder) with equal total RPN value in the classical evaluation with the proposed method.

Table 5. Risk assessment for physical conditions

No (i)	Health Problems	Noise					Insufficient air conditioning					Lighting					Total RPN	Total RPN_n	Rankig RPN_n
		P	S	D	RPN	RPN_{ni}	P	S	D	RPN	RPN_{ni}	P	S	D	RPN	RPN_{ni}			
1	Hearing loss	1	5	5	25	0.079 [25]											25	0.079	10
2	Cardiovasculer disorder						1	5	5	25	0.715						25	0.715	4
3	Psychological disorder	3	3	8	72	0.341 [25]	1	3	5	15	0.442						87	0.782	3
4	Heat injury						3	4	4	48	1.294						48	1.294	2
5	Heat loss						2	4	3	24	0.566 [26]						24	0.566	5
6	Faint						1	5	1	5	0.156						5	0.156	9
7	Tearing											5	3	2	30	0.331	30	0.331	7
8	Eye disorder											2	5	4	40	0.378 [27]	40	0.378	6
9	Headache	7	4	4	112	1.468	1	3	4	12	0.442 [13]	3	4	2	24	0.283	148	2.193	1
10	Fluid loss						3	3	2	18	0.175						18	0.175	8

Table 6. Noise hazard P, S and D description

	P			S			D		
	Lower Value	Upper Value	Value	Lower Value	Upper Value	Value	Lower Value	Upper Value	Value
$\mu+2\sigma, \mu+3\sigma$				6	7	3.00			
$\mu+\sigma, \mu+2\sigma$	7	10	6.11	5	6	2.00	8	10	4.16
$\mu, \mu+\sigma$	4	7	3.06	4	5	1.00	6	8	2.08
$\mu-\sigma, \mu$	1	4	0.33	3	4	1.00	3	6	0.48
$\mu-2\sigma, \mu-\sigma$	0	1	0.16	2	3	0.50	1	3	0.24
$\mu-3\sigma, \mu-2\sigma$				1	2	0.33			

i. Risk Analysis for Chemical Conditions

The hazards that may occur due to chemical conditions in the operating room were classified under four main headings "disinfectants and sterilizers, "Cleaning Chemicals", "laser" and "waste gases" given in Table 9 as a result of expert opinion and literature review. According to the classical FMEA assessment, the most important health problem for the "disinfectants and sterilizers" "allergic reaction". 'Toxic effects such as nausea and dizziness' and the "destroying the skin's protective properties" are the problems with equal and highest importance for the

heading cleaning chemicals; "destroying the skin's protective properties" is again the health problem with the highest importance for the laser hazard group, and "toxic effects such as nausea and dizziness" is the most important health problem for waste gases hazard group.

Table 7. Insufficient ventilation hazard P, S and D description

	P			S			D		
	Lower Value	Upper Value	Value	Lower Value	Upper Value	Value	Lower Value	Upper Value	Value
$\mu+2\sigma,\mu+3\sigma$	4	5	2.85	6	7	2.70	6	8	4.54
$\mu+\sigma,\mu+2\sigma$	3	4	1.90	5	6	1.80	5	6	3.02
$\mu,\mu+\sigma$	2	3	0.95	4	5	0.90	3	5	1.51
$\mu-\sigma,\mu$	1	2	0.95	3	4	0.90	2	3	0.66
$\mu-2\sigma,\mu-\sigma$	0	1	0.53	1	3	0.56	1	2	0.33
$\mu-3\sigma,\mu-2\sigma$				0	1				

Table 8. Lighting hazard P, S and D description

	P			*S*			*D*		
	Lower Value	*Upper Value*	*Value*	*Lower Value*	*Upper Value*	*Value*	*Lower Value*	*Upper Value*	*Value*
$\mu+2\sigma,\mu+3\sigma$	6	8	4.58	6	7	3	5	6	3.46
$\mu+\sigma,\mu+2\sigma$	5	6	3.06	5	6	2	4	5	2.31
$\mu,\mu+\sigma$	3	5	1.53	4	5	1	3	4	1.15
$\mu-\sigma,\mu$	2	3	0.65	3	4	1	2	3	0.87
$\mu-2\sigma,\mu-\sigma$	1	2	0.33	2	3	0.5	1	2	0.43
$\mu-3\sigma,\mu-2\sigma$				1	2	0.33			

With the consideration of distribution in the hazard group in Equation (2) based on Table 4 formulations proposed in the study;

- It could be determined that among the health problems "toxic effects such as nausea and dizziness" and "destroying the skin's protective properties" that are in the cleaning chemicals hazard group and have equal RPN values, the 'destroying the skin's protective properties was more critical; and that 'allergic reactions' was more critical when compared with the health problem 'headache'.

- In the laser hazard group, 'headache' and "eye disorders" have equal points and importance according to classical RPN assessment but with RPN_n, "eye disorders" were detected to be more critical in this group.

- Although "eczema" and "fatigue" health problems caused by disinfectants and sterilizers and "waste gases" hazards respectively have the same importance in terms of classical RPN value, it was determined that "fatigue" problem due to "waste gases" had more critical importance when compared with the proposed method. When the total value of classical RPN values resulting from chemical conditions are taken into consideration, it is seen in Table 9 that the most important health problem is "toxic effects such as nausea and dizziness". According to the total risk score values calculated by equation (3), the order of health problems according to importance are "destroying the skin's protective properties", 'toxic effects such as nausea and dizziness' and "allergic reaction". Working in a closed environment for long hours and especially the use of many disinfectants sterilizers and components in the operating room make the operating room critical due to exposure to chemical effects.

ii. Risk Analysis for Psychological Conditions

Another main hazard group encountered in the operating rooms is psychological hazards due to intensive and stressful working conditions. Psychological hazards were divided into three basic hazard groups, namely 'working conditions', 'night shift' and 'fear of contamination". The sub-hazards that may be

caused by these hazards and the risk evaluation of these hazards are given in Table 10. By taking the distribution of the "over fatigue" hazard group within itself into consideration, it is seen that (RPN_{ni}) "over fatigue" creates a greater risk in the "night shift" than the "working conditions" that has the same RPN value with the classical analysis. While "unwillingness to work" on the night shift has a lower importance point than all the hazards caused by working conditions according to the classical RPN value, it was detected to have a higher importance than the hazards caused by the working conditions because of the RPNni assessment. In the general evaluation, the most important hazards according to the Total RPN value are ranked as follows: 'anxiety disorder,' non-adaptation to the working environment, and depression. However, the order of importance of the probable hazards, based on the RPN values calculated with Equation (3), is: 'anxiety disorder,' depression, and 'unwillingness to work,' as shown in Table 10."

Table 9. Risk assessment for chemical conditions

No	Health Problems	Disinfectants and sterilizers					Cleaning chemicals					Laser					Waste gases					Total RPN	Total Risk Score RPN_n	Rank RPN_n
		P	S	D	RPN	RPN_{ni}	P	S	D	RPN	RPN_{ni}	P	S	D	RPN	RPN_{ni}	P	S	D	RPN	RPN_{ni}			
1	Allergic Reaction	9	7	2	126	2.216	2	3	4	24	0.501											150	2.717	3
2	Toxic Effects Such as Nausea and Dizziness	8	7	2	112	2.216	3	5	3	45	0.706						2	5	3	30	0.765	187	3.686	2
3	Fatigue											1	2	4	8	0.174	3	2	4	24	0.330	32	0.504	7
4	Headache	8	5	2	80	0.484	4	3	2	24	0.252	1	3	5	15	0.354	1	3	2	6	0,.63	125	1.253	5
5	Destroying the Skin's Protective Properties	3	8	2	48	0.111 [28]	3	5	3	45	2.520 [28]	4	6	3	72	2.855						165	5.486	1
6	Egzama	6	4	1	24	0.024 [28]	4	4	2	32	0,50 [28]											56	0.528	6
7	Eye Disorders	1	7	7	49	1.044						1	5	3	15	0.638						64	1.681	4

Table 10. Risk assessment for psychological conditions

No	Health Problems	Working Conditions					Night Shift					Fear of Contamination					Total RPN	Total Risk Score to Ensure Accuracy	Ranking
		P	S	D	RPN	RPN_{ni}	P	S	D	RPN	RPN_{ni}	P	S	D	RPN	RPN_{ni}		RPN_n	RPN_n
1	Non-adaptation to the Working Environment	7	3	3	63	0.365 [1]	2	2	4	16	0.137 [2]	6	6	4	144	0.514		1.016	5
2	Unwillingness to Work	6	6	4	144	2.191	6	3	2	36	0.626 [2]	7	5	1	35	0.243	223	3.060	3
3	Over Fatique	6	5	2	60	1.095	5	4	3	60	1.826 [2]						215	2.921	4
4	Depression	8	6	2	96	2.191						6	7	3	126	1.027	120	3.218	2
5	Anxiety Disorder	6	5	4	120	2.191	3	6	6	108	6.390	6	6	3	108	0.514 [29]	222	9.095	1

Table 11. Risk assessment for biological conditions

No	Health Problems	Exchange of Potentially Contaminated items					Working at Close Distance					Damage of Protective Equipment, Gloves, Mask etc.					Training and Practice of Health Personnel on the Subject				
		P	S	D	RPN	RPN_{ni}	P	S	D	RPN	RPN_{ni}	P	S	D	RPN	RPN_{ni}	P	S	D	RPN	RPN_{ni}
1	Hepatit B	3	2	3	18	0.306 [30]						2	1	8	16	0.212	1	2	7	14	0.133
2	HIV	1	8	1	8	1.500 [30]						1	7	8	56	3.394	1	8	7	56	1.673
3	HCV	1	8	2	16	2.750 [30]						1	7	8	56	3.394	1	7	7	49	1.673
4	Tbc						1	5	2	10	0.157 [31]										
5	HDV-delta Hepatit	1	8	3	24	2.750						1	7	8	56	3.394	1	7	7	49	1.673
6	Covid-19						3	8	5	120	6.364 [32]	3	8	5	120	1.886 [32]	4	8	9	288	12.048 [33]

Table 12. Ranked evaluation of biological agents based on total risk score under unidentified infection conditions

No	Health Problems	Unidentified Infection					Total RPN	Total Risk Score RPN	Ranking RPNn
		P	S	D	RPN	RPN_n			
1	Hepatit B	2	1	8	16	0.156	64	0.806	6
2	HIV	2	7	8	112	2.049	232	8.616	4
3	HCV	2	7	8	112	2.049	233	9.866	3
4	Tbc	3	7	7	147	1.502	157	1.660	5
5	HDV-delta Hepatit	2	7	9	126	2.185	255	10.003	2
6	Covid-19	5	8	10	400	12.821	928	33.118	1

Hepatitis virus-related diseases, tuberculosis, and Covid-19 which affect the whole world are the main biological risks encountered in operating rooms. Since the hepatitis virus and COVID-19 tests are usually performed before surgery, probability values are usually low. However, since the confidence intervals of the tests are changeable, waiting for the test results in situations that require emergency surgery such as brain haemorrhage can lead to untested situations, as the patient dies. Biological risk increases in the operating room due to "Contamination during the insertion and removal of the injector, etc'' during insertion and removal of a piercing cutting tool like an injector.
There is an evaluation for five groups and two of them are "Contamination during the the insertion and removal of the injector, etc ". Apart from this, the hazard of 'contamination of infected particles from the ventilation system' is also one of the biological risk factors in the operating room. However, this hazard was determined but the evaluation of it could not be done. Generally, negative compressed air is used in the operating rooms, and the ventilation system uses clean air; these are the only risk factors for COVID-19.

Probability, severity, and detectability values for COVID-19 were determined as 3.8.7, respectively with expert opinion. According to this evaluation, the RPN value poses the most significant risk with 168 but it was not considered in the evaluation since no other hazard was identified.

As a result of the evaluation based on biological risks, COVID-19 disease is the riskiest disease due to "unidentified infection". According to the total evaluation, Covid-19 disease is followed by HDV, HCV, and HIV. The ranking obtained with the approach suggested in the study is provided in Table 11 and Table 12.

The results obtained according to the total RPNn for each hazard group are given in Figure 1. The hazard numbers within each hazard group are given on the bars. The most critical health problem in the operating room according to Figure 1 occurs due to biological conditions with the "Covid-19". This health problem is followed by the hazards with numbers 5 and 3 that occur also due to biological conditions. This situation shows that the most critical risk source consists of biological conditions. In Figure 1, it is seen that the most critical hazard group after the hazards and health problems due to biological conditions result from psychological conditions. The fact that teams consisting of many workers from different levels work in the operating room for long working hours also makes psychological conditions important and its importance status is seen in Figure 1.

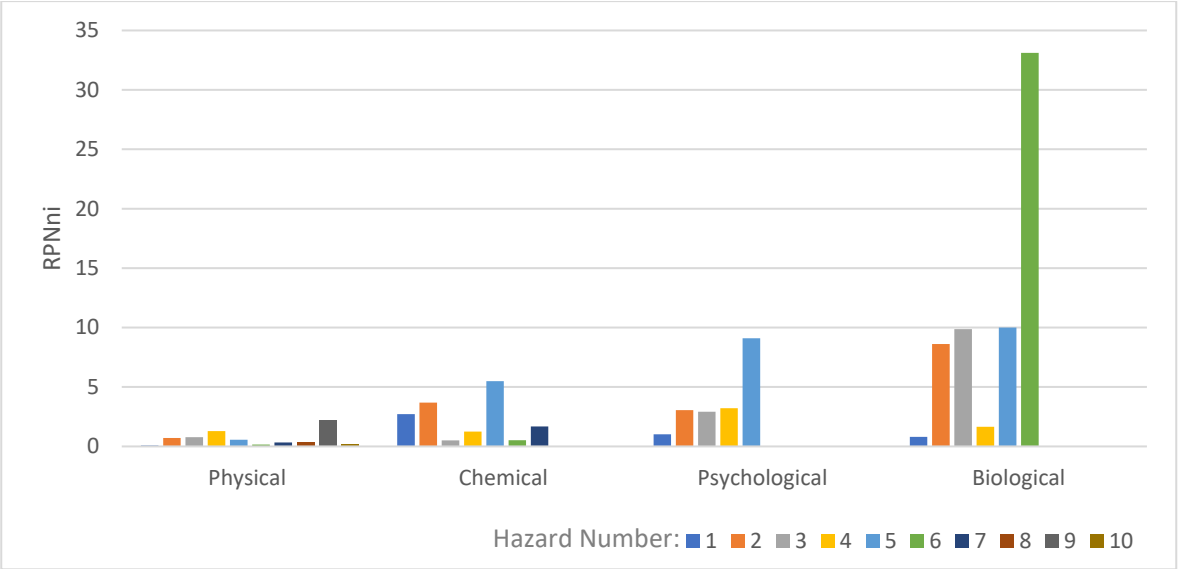

Figure 1. General evaluation

4. Conclusion

Risk analyses find an application area in every sector with legal regulations and with the increase in social conscience. There are many methods used in risk analyses and scaling is done according to the scales determined in these methods. However, when risk analyses are investigated on practices, it is seen that the place and distribution of the hazard in its source is an important factor. Risk analyses that take the distribution of each health problem in the hazard source contribute to determining the importance levels of the health problems more precisely and correctly. The steps that were followed in the method that was developed in this study and the sub-hazard (health care problems) caused by these hazards by the FMEA method, scale definition of the P, S, and D points in this evaluation according to the average and standard deviation values in the related hazard source and obtaining the RPNn values by doing the risk analysis according to this new scale and calculation of the total RPNn value. The risk analysis done depending on the scale according to the distribution of P, S, and D values in the hazard source constitutes the original aspect of the study.

Healthcare services are work areas in which activities related to every section of society are carried out and which contain many risks to work and about the health of workers. With its many departments, factors such as the generally long working hours in the operating rooms where all surgical procedures are performed and the simultaneous work of many people in the operations bring about many probable hazards and may cause health problems.

This situation necessitates risk analyses to be done in the operating rooms. Thus, the approach proposed in this study was carried out by taking the operating room department of a big hospital into consideration. The hazards that could occur in an operating room were analysed in four

classes: Physical, chemical, psychological, and biological hazards.

The descriptions of hazards and potential risk and/or sub-hazards that can occur due to hazards in each group were made, and risk assessment was done with the proposed method. As a result of this evaluation, the most important hazards were determined as "headache", 'Loss of protective feature of the skin', "anxiety disorder" and "Covid-19" in the physical, psychological, and biological conditions respectively. The approach proposed in the study can be used in the production sector or different departments of the hospitals in future studies.

Article Information Form

Acknowledgments
We would like to thank Prof. Dr. Yasemin Güneş from the Department of Anesthesiology at Çukurova University and Dr. Mesut Koca, pediatric surgeon at a private hospital, for their valuable support and contributions to this study

Funding
Authors have not received any financial support for the research, authorship, or publication of this study.

Authors Contribution
Authors contributed equally to the study.

The Declaration of Conflict of Interest/ Common Interest
No conflict of interest or common interest has been declared by authors.

The Declaration of Ethics Committee Approval
This study does not require ethics committee permission or any special permission.

The Declaration of Research and Publication Ethics
Authors of the paper declare that they comply with the scientific, ethical, and quotation rules of SAUJS in all processes of the paper and that they do not make any falsification of the data collected. In addition, they declare that Sakarya University Journal of Science and its editorial board have no responsibility for any ethical violations that may be encountered and that this study has not been evaluated in any academic publication environment other than Sakarya University Journal of Science.

References

[1] A. Sheikhzadeh, C. Gore, J.D. Zuckerman, M. Nordin, "Perioperating nurses and technicians perceptions of ergonomic risk factors in the surgical environment," Applied ergonomics, 40(5), 833-839, 2009.

[2] D. Yu, B. Lowndes, C. Thiels, J. Bingener, A. Abdelrahman, R. Lyons, S. Hallbeck, "Quantifying intraoperative workloads across the surgical team roles: Room for better balance?," World journal of surgery, 40(7), 1565-1574, 2016.

[3] F. Vural, E. Sutsunbuloglu. "Ergonomics: an important factor in the operating room," Journal of perioperative practice, 26(7-8), 174-178, 2016.

[4] N. Rafter, A. Hickey, S. Condell, R. Conroy, P. O'Connor, D. Vaughan, D. Williams, "Adverse events in healthcare: learning from mistakes," *QJM*, 108(4), 273–277. 2014.

[5] L.T. Kohn, J. M. Corrigan, M. S. Donaldson. To Err Is Human: Building a Safer Health System, National Academies Press, 2000.

[6] D. Gupta, "Surgical Suites' Operations Management," Production and Operations Management, 16(6), 689–700, 2009.

[7] U. Matern, S. Koneczny, "Safety, hazards and ergonomics in the operating room," Surgical endoscopy, 21(11), 1965-1969, 2007.

[8] R. Khasha, M. M. Sepehri, T. Khatibi, T, "A fuzzy FMEA approach to prioritizing

surgical cancellation factors," International Journal of Hospital Research, 2(1), 17-24, 2013.

[9] L. Pan, S. Tan, L. Cao, X. Feng, "Risk factor analysis and management strategies of operating room-related infections after coronary artery bypass grafting," Journal of thoracic disease, 10(8), 4949, 2018.

[10] G. Abo El Ata, S. El Desouky, M. Manawil, E. Khalifa, "Assessment of work-related musculoskeletal symptoms in operation room nurses," Curr Sci Int, 5(2), 215-22, 2016.

[11] R. K. Voss, Y. J. Chiang, K. D. Cromwell, D.L. Urbauer, J. E. Lee, J. N. Cormier, C.C. H. Stucky, C. C. H. "Do no harm, except to ourselves? A survey of symptoms and injuries in oncologic surgeons and pilot study of an intraoperative ergonomic intervention," Journal of the American College of Surgeons, 224(1), 16-25, 2017.

[12] S. H. Ho, L. Rosario, M. M. Rahman, "Three-dimensional analysis for hospital operating room thermal comfort and contaminant removal," Applied Thermal Engineering, 29(10), 2080-2092, 2009.

[13] E. G. Dascalaki, A. G. Gaglia, C. A. Balaras, A. Lagoudi, "Indoor environmental quality in Hellenic hospital operating rooms," Energy and Buildings, 41(5), 551-560, 2009.

[14] C. S. Rinder, "Fire safety in the operating room," Current Opinion in Anesthesiology, 21(6), 790-795, 2008.

[15] W. C. Culp, B.A. Kimbrough, S. Luna, "Flammability of surgical drapes and materials in varying concentrations of oxygen," Anesthesiology: The Journal of the American Society of Anesthesiologists, 119(4), 770-776, 2013.

[16] J. W. Senders, "FMEA and RCA: the mantras; of modern risk management," *BMJ* Quality & Safety, 13(4), 249-250, 2004.

[17] B. Mosallanezhad, "Using fuzzy FMEA to increase patient safety in fundamental processes of operating room," Journal of Industrial and Systems Engineering, 11(3), 146-166, 2018.

[18] H. C. Liu, J. X. You, X. Y. You, "Evaluating the risk of healthcare failure modes using interval 2-tuple hybrid weighted distance measure," Computers & Industrial Engineering, 78, 249-258, 2014.

[19] P. Trucco, M. Cavallin, "A quantitative approach to clinical risk assessment: The CREA method," Safety science, 44(6), 491-513, 2006.

[20] L. Guo, "Implementation of a risk management plan in a hospital operating room", International Journal of Nursing Sciences, 2(4), 348-354, 2015.

[21] N. Kasatpibal, J. D. Whitney, S. Katechanok, S. Ngamsakulrat, B. Malairungsakul, P. Sirikulsathean, T. Muangnart, "Prevalence and risk factors of needlestick injuries, sharps injuries, and blood and body fluid exposures among operating room nurses in Thailand," American journal of infection control, 44(1), 85-90, 2016.

[22] M. Amghar, B. Zoulloutı, N. Sbıtı, "Risk analysis of operating room using the fuzzy bayesian network model," International Journal of Engineering, 30(1), 66-74, 2017.

[23] Institute for Healthcare Improvement (Access date: April 1, 2025). Patient safety essentials toolkit: Failure Modes and Effects Analysis (FMEA) tool [Online]. Available: https://www.ihi.org/sites/default/files/SafetyToolkit_FailureModesandEffectsAnalysis.pdf

[24] D. H. Stamatis, "Failure mode and effect analysis: FMEA from theory to execution. Quality Press," 2003.

[25] Alemdağ, M. Ameliyathanede Çalışan Sağlık Personelinin Sağlığı Geliştirici

Yaşam Biçimi Davranışları ve İlişkili Faktörlerin Belirlenmesi (Doctoral dissertation, Ankara Yıldırım Beyazıt Üniversitesi Sağlık Bilimleri Enstitüsü), 2019.

[26] R. Van Gaever, V. A Jacobs, M. Diltoer, L. Peeters, S. Vanlanduit, "Thermal comfort of the surgical staff in the operating room," Building and Environment, 81, 37-41, 2014.

[27] M Lembo, V. Cannatà, A. Militello, M. Ritrovato, S. Zaffina, P. Derrico, M Borra, "Artificial lighting and blue light in the operating room: What risks for the surgeon," La Medicina del lavoro, 106(5), 342-350, 2015.

[28] S. Q. Wilburn, G. Eijkemans, "Preventing needlestick injuries among healthcare workers: A WHO–ICN Collaboration," International Journal of Occupational and Environmental Health, 10: 451–456, 2004.

[29] M. S. Spoorthy, S. K. Pratapa, S. Mahant, "Mental health problems faced by healthcare workers due to the COVID-19 pandemic–A review," Asian Journal of Psychiatry, 51, 102119, 2020.

[30] S. Reddy, R. Manuel, E. Sheridan, G. Sadler, S. Patel, P. Riley, P, "Brucellosis in the UK: A Risk to Laboratory Workers? Recommendations For Prevention and Management of Laboratory Exposure," J. Clin Pathol, 63, 90-92, 2010.

[31] S. Hoşoğlu, A. Ç. Tanrıkulu, C. Dağlı, Ş. Akalın Ş "Bir Üniversite Hastanesinin Çalışanlarında Tüberküloz Riski," Toraks Dergisi, 5(3): 196-200, 2004.

[32] A. S. Karaca, M. M. Özmen, A. D. Uçar, A. Ç. Yastı, S. Demirer, "COVID-19'lu hastalarda genel cerrahi ameliyathane uygulamaları," Turk J Surg, 36(1), 6-10, 2020.

[33] R. Pan, L. Zhang, J. Pan, "The Anxiety Status of Chinese Medical Workers During the Epidemic of COVID19: A Meta-Analysis", Psychiatry investigation, 17(5), 475–480, 2020.